T2R2 東京科学大学 リサーチリポジトリ
Science Tokyo Research Repository

論文 / 著書情報
Article / Book Information

題目(和文)	電気化学ヘテロダイン検出振動和周波発生 分光法の実現および電解質溶液/電極界面構造のその場観察
Title(English)	Realization of Electrochemical Heterodyne-Detected Vibrational Sum Frequency Generation Spectroscopy and In-situ Observation of Interface Structure of Electrolyte/Electrode Interfaces
著者(和文)	佐山篤
Author(English)	Atsushi Sayama
出典(和文)	学位:博士(理学), 学位授与機関:東京工業大学, 報告番号:甲第11375号, 授与年月日:2020年3月26日, 学位の種別:課程博士, 審査員:大島 康裕,田原 太平,腰原 伸也,北島 昌史,沖本 洋一,山﨑 優一
Citation(English)	Degree:Doctor (Science), Conferring organization: Tokyo Institute of Technology, Report number:甲第11375号, Conferred date:2020/3/26, Degree Type:Course doctor, Examiner:,,,,,
学位種別(和文)	博士論文
Type(English)	Doctoral Thesis

Powered by T2R2 (Science Tokyo Research Repository)

学位論文

Realization of Electrochemical Heterodyne-Detected Vibrational Sum Frequency Generation Spectroscopy and In-situ Observation of Interface Structure of Electrolyte/Electrode Interfaces

電気化学ヘテロダイン検出振動和周波発生分光法の実現および電解質溶液/電極界面構造のその場観察

2019 年度　博士論文

指導教員 ： 大島　康裕

田原　太平

東京工業大学 理学院 化学系　化学コース

大島・山﨑研究室

佐山 篤

Index

Index of figures

Index of tables

1. Introduction

1.1. Study of interfaces

"Interface" is defined as a boundary of different media and it plays very important roles in both basic and applied science. For instance, the cell membranes separate inside and outside of cells and play crucial roles in biological functions such as a transportation of chemical species from inside to outside and vice versa [1]. Because cell membranes are regarded as the interface between inside and outside of cells, a lot of cell biological issues are related to interface science. Heterogeneous catalysis is one of the central issues in chemistry. Heterogeneous catalytic reactions occur only at the surface of catalysts, and the catalysts selectively act with the reactants and activate the chemical reaction [2]. Electrolyte/electrode interfaces are the core of the electrochemistry and battery and hence are of particular importance in industry [3]. All these interfaces are very important for our lives. Thus, elucidation of structure and reactions at various interfaces at the molecular level is crucial for understanding not only fundamental sciences but also applied sciences. In this thesis, I will focus on the electrolyte/electrode interfaces.

Elucidating the structures and mechanism of electrochemical reactions at electrochemical interfaces is important for understanding and improving battery operation. For example, solid electrolyte interphase (SEI) enables the stable operation of the lithium ion battery. Although the lithium ion battery has been commercially used in all over the world, the structure and formation mechanism of SEI in the lithium ion battery has not been fully understood. Of course, current understanding of operation mechanisms of next-generation batteries [4] is even much more limited.

As already mentioned, the interfacial function is very important for both fundamental and applied sciences. Many scientists have been attracted to the interface science and made a lot of efforts to understand the interfaces. However, clear molecular-level pictures of interfaces have not been obtained for many cases, because it is difficult to detect the only response from molecules at the interface. In general, the number of interfacial molecules is much less than the number of bulk molecules. The signal from interface is thus often buried in the bulk signal, and it is difficult to extract the contribution from interfacial molecules. Therefore, it is necessary to use an interface-selective method.

For studying solid interfaces, several techniques can be used such as photoelectron spectroscopy [5, 6], scanning tunneling microscopy (STM) [7, 8], atomic force microscopy (AFM) [9, 10] and electron diffraction [11, 12]. Electron spectroscopic techniques are powerful tools in the vacuum environment, because they are element-selective and free from a selection rule which becomes

sometimes a serious problem in spectroscopy using photon. STM and AFM have extremely high space-resolution for solid surfaces. X-ray scattering [13-15] is also a powerful tool to study the structure of metal solid surfaces.

Spectroscopy using photon such as UV-vis, IR and Raman spectroscopy, is also a powerful method to study molecular structure. These methods have been applied to various media such as gas phase [16, 17] and liquid phase [18, 19] for a long time and revealed a number of phenomena. However, these optical methods in the UV-IR wavelength region are generally not interface-selective. Therefore, some tricks are combined with these conventional spectroscopies for probing interfacial molecules. For electrolyte/electrode interfaces, subtractive normalized interfacial Fourier transform infrared (SNIFTIR) spectroscopy [20, 21], surface enhanced infrared absorption spectroscopy (SEIRAS) [22-25] and surface enhanced Raman spectroscopy (SERS) [26-29] have been often used to study the structure and reaction at the interface. However, SNIFTIR provides only a difference spectrum between spectra measured at a certain potential and reference potential, so that interface-selectivity of SNIFTIR is not perfect. SEIRAS and SERS provide good interface selectivity when applied to electrodes of plasmonic metals such as Cu, Ag and Au. However, the choice of electrode material is very limited. From these reasons, a more universal interface-selective spectroscopic technique is desired.

1.2. Vibrational sum frequency generation spectroscopy

One of the best techniques to solve the problems of conventional spectroscopy is even-order nonlinear spectroscopy, in particular, vibrational sum frequency generation (VSFG) spectroscopy. VSFG is one of the second-order nonlinear optical processes and an intrinsically interface-selective technique [30-32]. In this process, two pulses having visible (ω_{vis}) and infrared (ω_{IR}) frequencies are irradiated onto a sample. Then sum frequency (SF) light $\omega_{SF} = \omega_{vis} + \omega_{IR}$ is generated. The SF signal is generated only in a region where inversion symmetry is broken, such as interfaces. While most bulk phases have inversion symmetry, interfaces do not. Hence, VSFG can selectively detect the only molecules at the interface. When ω_{IR} matches with the vibrational resonance of the interfacial molecules, the SF signal is resonantly enhanced. Thus, VSFG can provide the vibrational spectra of molecules only at the interface. The usefulness of VSFG was shown by Shen and co-workers for the first time [30] and after their report, VSFG has been widely utilized for studying various interfaces [33-37].

VSFG spectroscopy is a unique tool to investigate the molecular structure at the interface. Nevertheless, it has serious problems. Because conventional VSFG detects the intensity of SF signal

(i.e., homodyne detection), only the absolute square of the second-order nonlinear susceptibility ($(|\chi^{(2)}|^2)$) is obtained. In such $|\chi^{(2)}|^2$ spectra, the interference between resonant and non-resonant signals and/or that between different vibrational resonances distort spectral features and the phase information (sign of $\chi^{(2)}$) is lost. In conventional VSFG spectroscopy, the peak fitting or theoretical calculation is needed for deducing the true spectra, i.e., the second-order nonlinear susceptibility itself ($\chi^{(2)}$).

To obtain the $\chi^{(2)}$ itself, some advanced VSFG techniques have been developed. Shen and co-workers have developed phase-sensitive sum frequency generation (PS-VSFG) spectroscopy [38, 39]. In their scheme, the phase of sample SF signal against to the reference signal is obtained by changing the angle of a phase modulator. This method does not need a complex analysis scheme to obtain the phase information, but a lot of data points are needed to be scanned in a point-by-point fashion because the narrow band IR pulse is employed. Recently, Tahara and co-workers have developed heterodyne-detected VSFG (HD-VSFG) spectroscopy which uses a broadband IR pulse [40]. HD-VSFG spectroscopy separately provides an imaginary part (Im) and a real part (Re) of $\chi^{(2)}$ by analyzing the interference pattern between the SF signal and an additional third pulse, i.e., local oscillator (LO). The interference pattern is Fourier transformed from a frequency domain to a time domain, and the interference term is extracted by a filter function. Then filtered interference term is inverse Fourier transformed to the frequency domain again and it gives the information about $\chi^{(2)}$ itself.

Both methods mentioned above provide $\chi^{(2)}$ itself. Therefore, the experimentally obtained spectra are free from spectral distortion and hence can be interpreted straightforwardly in the same way as interpretation of IR absorption and/or Raman spectra. Furthermore, the up/down orientation of interfacial molecules can be experimentally determined from the sign of $\mathrm{Im}\chi^{(2)}$. The latter is a unique advantage of PS-VSFG and HD-VSFG spectroscopy over any other interfacial spectroscopy. In particular, HD-VSFG spectroscopy has been intensively applied to the air/water [40], air/monolayer/water [41] interfaces, and provided important knowledge about the interface structure including the up/down orientation of interfacial molecules. For these simple interfaces, more advanced HD-VSFG techniques such as 2D-HD-VSFG and time-resolved HD-VSFG (TR-HD-VSFG) have been realized. 2D-HD-VSFG [42-44] and TR-HD-VSFG [45] have successfully revealed the heterogeneity of hydrogen-bond network and the femtosecond vibrational dynamics of interfacial water molecules. Furthermore, HD-VSFG spectroscopy has been applied to more complicated interfaces such as a silica/water interface [46, 47] and provided rich information about interface structure of the silica/water interface. As a next step, it was highly desirable to apply

HD-VSFG spectroscopy to more realistic interfaces such as electrolyte/electrode interfaces, which is the core of both fundamental and applied electrochemistry, as mentioned in section 1.1. In fact, this is the research subject of my Ph. D thesis study.

Electrolyte/electrode interfaces have been one of the most important subjects of VSFG spectroscopy for many years [48-58]. However, most of previous VSFG works of electrolyte/electrode interfaces were carried out by the conventional VSFG with homodyne detection because it is difficult to measure a reference spectrum, which is necessary for determining the phase and amplitude of SF signal, under an electrochemical condition. Actually, Zanni and co-workers applied HD-VSG spectroscopy to a CO-adsorbed electrolyte/electrode interface [59] but the sign of $\chi^{(2)}$ was not discussed because of this difficulty. In order to achieve the application of HD-VSFG to electrolyte/electrode interfaces, the phase reference is needed under the electrochemical environment. In other words, it is necessary to measure the reliable reference spectrum under the same condition as a sample spectrum is measured.

To overcome the serious problem, in the present thesis study, I develop a method which enables us to measure the phase reference under an electrochemical condition. Then, I apply HD-VSFG spectroscopy to the electrolyte/electrode interfaces using the phase reference and reveal the interface structure of the electrolyte/electrode interfaces including the up/down orientation of interfacial molecules.

1.3. Aims of this study

The aims of this study are as follows. The first aim is to develop the phase calibration method under the electrochemical environment. As mentioned in the previous section, the phase reference under electrochemical condition is essential to achieve the HD-VSFG measurements of electrolyte/electrode interfaces. Moreover, a spectro-electrochemical cell, which enables us to perform both electrochemical and spectroscopic measurements, is also required. Therefore, developing the phase reference and spectro-electrochemical cell is one of the central aims of this study.

The second is to obtain the molecular picture of electrolyte/electrode interfaces. The molecular-level picture of structure of electrolyte/electrode interfaces has not been elucidated well. HD-VSFG spectroscopy provides distortion-free vibrational spectra and the up/down orientation of interfacial molecules. These advantages are very useful to obtain the molecular-level picture of electrochemical interfaces. To demonstrate the usefulness and uniqueness of HD-VSFG measurements of electrolyte/electrode interfaces, I apply HD-VSFG spectroscopy to prototypical

electrolyte/electrode interfaces and discuss the structure and reactivity at these electrode interfaces.

By achieving these goals, I demonstrate the powerfulness of the HD-VSFG spectroscopy at electrolyte/electrode interfaces, which will open new ways to the spectro-electrochemistry field and bring a lot of new insights into the molecular details of electrolyte/electrode interfaces.

1.4. Outline of this thesis

The outline of this thesis is as follows. In chapter 2, the theoretical background of sum frequency generation is described. In chapter 3, the experimental setup of electrochemical HD-VSFG spectroscopy and the in-situ reference method are summarized, which are followed by the validation of the in-situ reference method. In chapter 4, the HD-VSFG study on the potential-dependent structure of the acetonitrile/platinum interface is described, which is a prototypical non-aqueous electrochemical interface. In chapter 5, the structure of super-concentrated electrolyte/electrode interface and the origin of reduction stability of solvents in such super-concentrated electrolyte are discussed. In chapter 6, the summary of the present study and the future perspectives are given.

2. Background of sum frequency generation [60]

In this chapter, first, the interaction between matter and light is described based on Maxwell equation (section 2.1 – 2.5). Next, the interaction between microscopic matter and light is discussed based on quantum mechanics (section 2.6 – 2.7). Then, to describe the interaction between macroscopic matter and light, the density matrix is introduced and linear and second-order nonlinear optical responses are expressed by using the results of section 2.6 and 2.7 (section 2.8 – 2.13). Finally, the conversion of the representation of second-order nonlinear susceptibility from the molecular frame to the laboratory frame is described (section 2.14).

2.1. Polarization

All matter consists of atoms. And atoms are constituted by nuclei and electrons. When the light, an electromagnetic wave, is incident into matter, the atoms interact with the incident light. The nuclei have positive charge, therefore it moves to the direction of electric field. On the other hand, electrons have negative charge, hence it moves to the opposite direction to the electric field. As a result, spatial electrical bias is generated in the atoms. This is known as polarization and expressed by equation (2.1).

$$\boldsymbol{P} = N\boldsymbol{\mu} \ . \tag{2.1}$$

Where, $\boldsymbol{P}$ is a polarization vector, N is number density of atoms and $\boldsymbol{\mu}$ is the electric dipole moment. When $+e$ and $-e$ charges are put with certain distance $\boldsymbol{d}$, $\boldsymbol{\mu}$ is described in equation (2.2).

$$\boldsymbol{\mu} = e\boldsymbol{d} \ . \tag{2.2}$$

Where, e is the magnitude of charge and $\boldsymbol{d}$ is the distance between the $+e$ and $-e$ charges (the direction is from $-e$ to $+e$). The optical response of matter is coming from polarization.

2.2. Interaction between matter and light

The behavior of electromagnetic wave is described by Maxwell equation. Maxwell equation in a dielectric medium is expressed by equation (2.3) – (2.6).

$$\boldsymbol{\nabla} \times \boldsymbol{E} = -\mu_0 \frac{\partial \boldsymbol{H}}{\partial t} \ . \tag{2.3}$$

$$\boldsymbol{\nabla} \times \boldsymbol{H} = \frac{\partial \boldsymbol{D}}{\partial t} \ . \tag{2.4}$$

$$\boldsymbol{\nabla} \cdot \boldsymbol{D} = 0 \ . \tag{2.5}$$

$$\boldsymbol{\nabla} \cdot \boldsymbol{H} = 0 \ . \tag{2.6}$$

Where, $\boldsymbol{E}$, $\boldsymbol{H}$, $\boldsymbol{D}$, μ_0, and t are the electric field, magnetic field, electric flux density, vacuum permeability, and time, respectively. And $\boldsymbol{D}$ is expressed as

$$\boldsymbol{D} = \varepsilon_0 \boldsymbol{E} + \boldsymbol{P} \ . \tag{2.7}$$

Here, ε_0 is the vacuum dielectric constant. Operate $\boldsymbol{H}\cdot$ from the left of equation (2.3).

$$\begin{aligned} \boldsymbol{H} \cdot (\boldsymbol{\nabla} \times \boldsymbol{E}) &= -\boldsymbol{H} \cdot \left(\mu_0 \frac{\partial \boldsymbol{H}}{\partial t} \right) \\ &= -\mu_0 \left(\boldsymbol{H} \cdot \frac{\partial \boldsymbol{H}}{\partial t} \right) \\ &= -\frac{\mu_0}{2} \frac{\partial}{\partial t} (\boldsymbol{H} \cdot \boldsymbol{H}) \ . \end{aligned} \tag{2.8}$$

Next, operating $\boldsymbol{E}\cdot$ from the left of equation (2.4) and using equation (2.7), the following relation is obtained.

$$\boldsymbol{E}\cdot(\boldsymbol{\nabla}\times\boldsymbol{H})=\boldsymbol{E}\cdot\left(\frac{\partial\boldsymbol{D}}{\partial t}\right)$$

$$=\boldsymbol{E}\cdot\frac{\partial}{\partial t}(\varepsilon_0\boldsymbol{E}+\boldsymbol{P})$$

$$=\varepsilon_0\boldsymbol{E}\cdot\frac{\partial}{\partial t}\boldsymbol{E}+\boldsymbol{E}\cdot\frac{\partial}{\partial t}\boldsymbol{P}$$

$$=\frac{\varepsilon_0}{2}\frac{\partial}{\partial t}(\boldsymbol{E}\cdot\boldsymbol{E})+\boldsymbol{E}\cdot\frac{\partial}{\partial t}\boldsymbol{P}\ .$$

(2.9)

Subtracting equation (2.9) from equation (2.8), we obtain,

$$\boldsymbol{H}\cdot(\boldsymbol{\nabla}\times\boldsymbol{E})-\boldsymbol{E}\cdot(\boldsymbol{\nabla}\times\boldsymbol{H})$$

$$=-\frac{\mu_0}{2}\frac{\partial}{\partial t}(\boldsymbol{H}\cdot\boldsymbol{H})-\frac{\varepsilon_0}{2}\frac{\partial}{\partial t}(\boldsymbol{E}\cdot\boldsymbol{E})-\boldsymbol{E}\cdot\frac{\partial}{\partial t}\boldsymbol{P}\ ,$$

(2.10)

and using the following vector formula;

$$\boldsymbol{H}\cdot(\boldsymbol{\nabla}\times\boldsymbol{E})-\boldsymbol{E}\cdot(\boldsymbol{\nabla}\times\boldsymbol{H})=\boldsymbol{\nabla}\cdot(\boldsymbol{E}\times\boldsymbol{H})\ , \qquad (2.11)$$

the following equation is obtained.

$$\boldsymbol{\nabla}\cdot(\boldsymbol{E}\times\boldsymbol{H})=-\frac{1}{2}\frac{\partial}{\partial t}\{\varepsilon_0(\boldsymbol{E}\cdot\boldsymbol{E})+\mu_0(\boldsymbol{H}\cdot\boldsymbol{H})\}-\boldsymbol{E}\cdot\frac{\partial}{\partial t}\boldsymbol{P}$$

$$=-\frac{1}{2}\frac{\partial}{\partial t}(\varepsilon_0|\boldsymbol{E}|^2+\mu_0|\boldsymbol{H}|^2)-\boldsymbol{E}\cdot\frac{\partial}{\partial t}\boldsymbol{P}\leftrightarrow-\frac{\partial}{\partial t}U=\boldsymbol{\nabla}\cdot\boldsymbol{S}+\boldsymbol{E}\cdot\frac{\partial}{\partial t}\boldsymbol{P}\ .$$

(2.12)

Here,

$$U \equiv \frac{1}{2}(\varepsilon_0|\boldsymbol{E}|^2 + \mu_0|\boldsymbol{H}|^2) \ . \tag{2.13}$$

$$\boldsymbol{S} \equiv \boldsymbol{E} \times \boldsymbol{H} \ . \tag{2.14}$$

$\boldsymbol{S}$ is the Poynting vector, which express energy flow density. The left side of equation (2.12) shows the energy decrease per unit time in a dielectric medium. The first term of right side of equation (2.12) is the energy flow from the dielectric medium. In the case of vacuum condition, the left side and the first term of right side of equation (2.12) are equal because of the energy conservation. However, in the dielectric medium, the energy is further decreased by the polarization, which is shown by the second term of right side of equation (2.12). Therefore, it is considered that the second term,

$$W = \boldsymbol{E} \cdot \frac{\partial}{\partial t}\boldsymbol{P} \ , \tag{2.15}$$

expresses an energy exchange, i.e., the work which the electric field does on the matter through the interaction between the electromagnetic wave and matter. In the case of $W > 0$, the energy is transferred from light to matter. This means light absorption. On the other hand, in the case of $W < 0$, the energy is transferred from matter to light. This means light amplification.

In equation (2.15), $\boldsymbol{E}$ and $\boldsymbol{P}$ oscillate as a function of a frequency of light, ω. In general, the period of light oscillation is much faster than the response time of detector. Therefore, only the cycle averaged observable can be obtained by experiments.

$$\bar{W} = \frac{1}{\tau}\int_{\mathbf{0}}^{\boldsymbol{\tau}} \boldsymbol{E}(t) \cdot \frac{\partial}{\partial t}\boldsymbol{P}(t)dt \ . \tag{2.16}$$

And in the case that $\boldsymbol{E}(t)$ and $\boldsymbol{P}(t)$ can be written by a Fourier display with a single frequency

component, $\boldsymbol{E}(t)$ and $\boldsymbol{P}(t)$ are given by the following equations:

$$\boldsymbol{E}(t) = \frac{1}{2}\left(\boldsymbol{E}(\omega)e^{-i\omega t} + \boldsymbol{E}(\omega)^* e^{+i\omega t}\right). \tag{2.17}$$

$$\boldsymbol{P}(t) = \frac{1}{2}\left(\boldsymbol{P}(\omega)e^{-i\omega t} + \boldsymbol{P}(\omega)^* e^{+i\omega t}\right) \ . \tag{2.18}$$

Here, * means a complex conjugate. Substituting equation (2.17) and (2.18) in equation (2.16), we obtain,

$$\begin{aligned}\bar{W} = \frac{1}{\tau}\int_{\mathbf{0}}^{\boldsymbol{\tau}} &\left(\frac{1}{2}\boldsymbol{E}(\omega)e^{-i\omega t} + \frac{1}{2}\boldsymbol{E}(\omega)^* e^{+i\omega t}\right) \\ &\times \frac{\partial}{\partial t}\left(\frac{1}{2}\boldsymbol{P}(\omega)e^{-i\omega t} + \frac{1}{2}\boldsymbol{P}(\omega)^* e^{+i\omega t}\right) dt \\ = \frac{1}{4\tau}\int_{\mathbf{0}}^{\boldsymbol{\tau}} &-i\omega\boldsymbol{E}(\omega)\cdot\boldsymbol{P}(\omega)e^{-2i\omega t} + i\omega\boldsymbol{E}(\omega)\cdot\boldsymbol{P}(\omega)^* \\ &-i\omega\boldsymbol{E}(\omega)^*\cdot\boldsymbol{P}(\omega) + i\omega\boldsymbol{E}(\omega)^*\cdot\boldsymbol{P}(\omega)^* e^{+2i\omega t} dt \ .\end{aligned} \tag{2.19}$$

The first term and fourth term are canceled out by the cycle average because of the oscillating component. Therefore, equation (2.19) is described as follows:

$$\begin{aligned}\bar{W} &= \frac{1}{4\tau}(i\omega\boldsymbol{E}(\omega)\cdot\boldsymbol{P}(\omega)^*\tau - i\omega\boldsymbol{E}(\omega)^*\cdot\boldsymbol{P}(\omega)\tau) \\ &= -\frac{i\omega}{4}(\boldsymbol{E}(\omega)^*\cdot\boldsymbol{P}(\omega) - \boldsymbol{E}(\omega)\cdot\boldsymbol{P}(\omega)^*) \\ &= -\frac{i\omega}{4}\cdot 2i\cdot \mathrm{Im}[\boldsymbol{E}(\omega)^*\cdot\boldsymbol{P}(\omega)] = \frac{\omega}{2}\mathrm{Im}[\boldsymbol{E}(\omega)^*\cdot\boldsymbol{P}(\omega)] \ .\end{aligned} \tag{2.20}$$

Where, Im[] is an imaginary part of a complex number. Equation (2.20) expresses the energy exchange between polarization and the electric field.

2.3. Linear and nonlinear optical processes

In the case that the electric-field amplitude of incident light is weak, induced polarization is proportional to the electric-field amplitude. This relation is written by equation (2.21).

$$\boldsymbol{P}(\omega) = \varepsilon_0 \chi^{(1)} \boldsymbol{E}(\omega) \ . \tag{2.21}$$

Where, $\chi^{(1)}$ is a linear susceptibility. The susceptibility expresses an optical response of matter. The linear optical processes such as absorption, reflection, scattering are caused by the linear polarization given by equation (2.21).

However, in the case that the electric-field amplitude of incident light is strong, polarization is not proportional to the electric-field amplitude, because the induced dipole moment of molecules is not proportional to the electric-field amplitude. This phenomenon is expressed by the power series expansion as follows:

$$\boldsymbol{P}(\omega) = \varepsilon_0 (\chi^{(1)} \boldsymbol{E}(\omega) + \chi^{(2)} \boldsymbol{E}(\omega)\boldsymbol{E}(\omega) + \chi^{(3)} \boldsymbol{E}(\omega)\boldsymbol{E}(\omega)\boldsymbol{E}(\omega) + \cdots) \ . \tag{2.22}$$

Where, $\chi^{(n)}$ (n = 1, 2, 3,…) is the n-th order susceptibility. Especially, n $\geqq$ 2 processes are called nonlinear optical processes.

As an example, I focus on the second-order nonlinear process. Second-order polarization $\boldsymbol{P}^{(2)}(\omega)$ is defined by equation (2.23).

$$\boldsymbol{P}^{(2)}(\omega) \equiv \varepsilon_0 \chi^{(2)} \boldsymbol{E}(\omega)\boldsymbol{E}(\omega) \ . \tag{2.23}$$

Assuming the incident electric field as follows:

$$\boldsymbol{E}(\omega) = \boldsymbol{E}_1 \cos \omega_1 t + \boldsymbol{E}_2 \cos \omega_2 t \ . \tag{2.24}$$

Substituting equation (2.24) to equation (2.23), the following equation is obtained.

$$\boldsymbol{P}^{(2)}(\omega) = \varepsilon_0 \chi^{(2)} \times (\boldsymbol{E}_1 \cos\omega_1 t + \boldsymbol{E}_2 \cos\omega_2 t)(\boldsymbol{E}_1 \cos\omega_1 t + \boldsymbol{E}_2 \cos\omega_2 t)$$

$$= \varepsilon_0 \chi^{(2)} (E_1^2 \cos^2\omega_1 t + 2\boldsymbol{E}_1 \cdot \boldsymbol{E}_2 \cos\omega_1 t \cos\omega_2 t + E_2^2 \cos^2\omega_2 t) \,. \quad (2.25)$$

By using the formulas of trigonometric function, the first term, second term and third term of the right side of equation (2.25) are rewritten as equation (2.26) to (2.28), respectively.

$$E_1^2 \cos^2\omega_1 t = \frac{E_1^2}{2}(1 + \cos 2\omega_1 t) \,. \quad (2.26)$$

$$2\boldsymbol{E}_1 \cdot \boldsymbol{E}_2 \cos\omega_1 t \cos\omega_2 t = \boldsymbol{E}_1 \cdot \boldsymbol{E}_2 \{\cos(\omega_1 + \omega_2) t + \cos(\omega_1 - \omega_2) t\} \,. \quad (2.27)$$

$$E_2^2 \cos^2\omega_2 t = \frac{E_2^2}{2}(1 + \cos 2\omega_2 t) \,. \quad (2.28)$$

These equations have the new frequency components such as $2\omega_1$, $\omega_1+\omega_2$, and $\omega_1-\omega_2$, which are generated through second-order nonlinear optical processes. Equation (2.26) and (2.28) express second harmonic generation (SHG) and the first term and second term of equation (2.27) express sum frequency generation (SFG) and difference frequency generation (DFG), respectively.

2.4. Symmetry of matter and nonlinear optical process

Nonlinear optical processes are classified by the order. In fact, not all orders of nonlinear optical processes occur all the time. The nonlinear optical process is sensitive to symmetry of matter.

The n-th order nonlinear polarization $P^{(n)}$ is expressed as follows:

$$\boldsymbol{P}^{(n)}(\omega) = \varepsilon_0 \chi^{(n)} \boldsymbol{E}^n(\omega) \,. \quad (2.29)$$

Let us consider the case that matter has inversion symmetry. The $\chi^{(n)}$ expresses a property of matter and does not change after the inversion operation. On the other hand, $\boldsymbol{P}^{(n)}(\omega)$ and $\boldsymbol{E}(\omega)$ are vector and then the sign of them is flipped after the inversion operation. Hence after the inversion operation,

equation (2.29) is written as the following equation.

$$-\boldsymbol{P}^{(\mathrm{n})}(\omega) = \varepsilon_0 \chi^{(\mathrm{n})}\left(-\boldsymbol{E}^{\mathrm{n}}(\omega)\right) = (-1)^n \varepsilon_0 \chi^{(\mathrm{n})} \boldsymbol{E}^{\mathrm{n}}(\omega) \ . \tag{2.30}$$

In the even order nonlinear optical process, (2.29) and (2.30) are equal.

$$\boldsymbol{P}^{(\mathrm{n})}(\omega) = \varepsilon_0 \chi^{(\mathrm{n})} \boldsymbol{E}^{\mathrm{n}}(\omega) = -\boldsymbol{P}^{(\mathrm{n})}(\omega) \ . \tag{2.31}$$

In order to satisfy equation (2.31), the $\chi^{(\mathrm{n})}$ must be zero. Therefore, the even order nonlinear optical process is allowed only in media where inversion symmetry is broken, such as interfaces, chiral molecules, and nonlinear optical crystals. This is why sum frequency generation is intrinsically interface-selective.

2.5. Interaction and susceptibility

The interaction between the matter and electric field is given by equation (2.20). And the first-order polarization is expressed by equation (2.21). Substituting equation (2.21) to (2.20) gives the relation between the light-matter interaction and susceptibility.

$$\bar{W} = \frac{\omega}{2} \mathrm{Im}\left[\boldsymbol{E}(\omega)^* \cdot \varepsilon_0 \chi^{(1)} \boldsymbol{E}(\boldsymbol{\omega})\right] = \frac{\varepsilon_0 \omega}{2} |E(\omega)|^2 \mathrm{Im}\chi^{(1)} \ . \tag{2.32}$$

Equation (2.32) shows the energy transfer from light to matter (i. e., absorption). The absorption intensity is proportional to the imaginary part of the susceptibility. Hence, the $\mathrm{Im}\chi^{(1)}$ gives the linear optical response of matter. In this process, the incident light acts as a probe light. The signals are obtained as an increase or decrease of the probe light intensity.

Second-order nonlinear polarization contains even numbers of electric-field terms. Therefore, the Im[] of equation (2.20) contains odd numbers of electric-field terms and the electric-field term cannot be factor out from Im[]. Because of this reason, the signals are not obtained as an increase of decrease or the probe light intensity in the second-order nonlinear process. In this case, an intensity of new light (SFG, DFG) generated by induced second-order nonlinear polarization can be detected. The intensity of detected light reflects an absolute square of the second-order nonlinear susceptibility.

2.6. Time evolution operator and perturbation expansion

The time-dependent Schrödinger equation is shown by equation (2.33).

$$\frac{\partial}{\partial t}|\Psi(t)\rangle = -\frac{2\pi i}{h}H(t)|\Psi(t)\rangle\,. \tag{2.33}$$

Where, $\Psi(t)$, $H(t)$, h are the quantum state vector at time t, Hamiltonian of system, and plank constant, respectively. In general, it is difficult to solve equation (2.33) analytically. Therefore, an approximation such as perturbation expansion is used to solve equation (2.33). In order to describe the time evolution of $\Psi(t)$, a time evolution operator $u(t,t_0)$ is defined as follows:

$$u(t,t_0)|\Psi(t_0)\rangle = |\Psi(t)\rangle\ . \tag{2.34}$$

The time evolution operator satisfies following relations:

$$u(t_0,t_0) = 1\ . \tag{2.35}$$

$$u(t_2,t_1)u(t_1,t_0) = u(t_2,t_0)\ . \tag{2.36}$$

Substituting equation (2.34) to (2.33), the following equation is obtained.

$$(\frac{\partial u(t,t_0)}{\partial t})|\Psi(t_0)\rangle = -\{\frac{2\pi i}{h}H(t)u(t,t_0)\}|\Psi(t_0)\rangle\ . \tag{2.37}$$

For equation (2.37) to hold with arbitrary t_0, equation (2.38) must be satisfied.

$$\left(\frac{\partial u(t,t_0)}{\partial t}\right) = -\frac{2\pi i}{h}H(t)u(t,t_0)\ . \tag{2.38}$$

Equation (2.38) describes the time evolution of $u(t,t_0)$.

In the case that Hamiltonian is time-independent, a solution of equation (2.38) is shown by equation (2.39).

$$u(t,t_0) = C\mathrm{e}^{-\frac{2\pi i}{h}Ht} \ . \tag{2.39}$$

Where, C is a coefficient and from equation (2.35) and (2.39),

$$C = \mathrm{e}^{\frac{2\pi i}{h}Ht_0} \ . \tag{2.40}$$

In general, Hamiltonian depends on time, therefore a sequential solution is used in order to solve equation (2.38). Integrate equation (2.38) from t_0 to t:

$$\int_{t_0}^{t} \frac{\partial u(\tau_1,t_0)}{\partial \tau_1}\,\mathrm{d}\tau_1 = -\frac{2\pi i}{h}\int_{t_0}^{t} H(\tau_1)u(\tau_1,t_0)\,\mathrm{d}\tau_1 \ . \tag{2.41}$$

The left side of equation (2.41) is calculated as follows:

$$[u(\tau_1,t_0)]_{t_0}^{t} = u(t,t_0) - u(t_0,t_0) = u(t,t_0) - 1 \ . \tag{2.42}$$

From equation (2.41) and (2.42), $u(t,t_0)$ is described as equation (2.43).

$$u(t,t_0) = 1 - \frac{2\pi i}{h}\int_{t_0}^{t} H(\tau_1)u(\tau_1,t_0)\,\mathrm{d}\tau_1 \ . \tag{2.43}$$

The right side of equation (2.43) contains $u(t,t_0)$ itself. Therefore, let us try to substitute $u(t,t_0)$ into the right side of equation (2.43) and solve the equation sequentially. Finally, $u(t,t_0)$ is expressed by equation (2.44).

$$u(t,t_0) = 1 + \sum_{\mathrm{n}=1}^{\infty} (-\frac{2\pi i}{h})^{\mathrm{n}}$$

$$\times \int_{t_0}^{t} \int_{t_0}^{\tau_{\mathrm{n}}} \cdots \int_{t_0}^{\tau_2} H(\tau_{\mathrm{n}}) H(\tau_{\mathrm{n}-1}) \cdots H(\tau_1)\, \mathrm{d}\tau_{\mathrm{n}} \mathrm{d}\tau_{\mathrm{n}-1} \cdots \mathrm{d}\tau_1 \ .$$

(2.44)

Here, integral variables were rewritten, and $\tau_{\mathrm{n}} > \tau_{\mathrm{n-1}} > \cdots > \tau_1$. If the Hamiltonian is time-independent, equation (2.44) is written as the following equation.

$$u(t,t_0) = 1 + \sum_{\mathrm{n}=1}^{\infty} (-\frac{2\pi i}{h})^{\mathrm{n}} H^{\mathrm{n}} \int_{t_0}^{t} \int_{t_0}^{\tau_{\mathrm{n}}} \cdots \int_{t_0}^{\tau_2} \mathrm{d}\tau_{\mathrm{n}} \mathrm{d}\tau_{\mathrm{n}-1} \cdots \mathrm{d}\tau_1 \ .$$

(2.45)

The integral part of equation (2.45) is corresponding to a partial volume of n-dimension space and equal to $(t\text{-}t_0)^{\mathrm{n}}/\mathrm{n}!$. Therefore, $u(t,t_0)$ can be described as equation (2.46).

$$u(t,t_0) = \sum_{\mathrm{n}=0}^{\infty} \frac{1}{\mathrm{n}!} \left\{ -\frac{2\pi i}{h} H(t-t_0) \right\}^{\mathrm{n}} = \mathrm{e}^{-\frac{2\pi i}{h} H \cdot (t-t_0)} \ .$$

(2.46)

The Hermite conjugate of equation (2.46) is expressed by the following equation.

$$u^*(t,t_0) = \mathrm{e}^{\frac{2\pi i}{h} H \cdot (t-t_0)} \ . \qquad (2.47)$$

Equation (2.47) shows a reverse time evolution operator, because the following equation is satisfied.

$$u^*(t,t_0) u(t,t_0) = \mathrm{e}^{\frac{2\pi i}{h} H \cdot (t-t_0)} \mathrm{e}^{-\frac{2\pi i}{h} H \cdot (t-t_0)} = 1 \ . \qquad (2.48)$$

2.7. Interaction representation

The interaction between a molecule and light is probabilistically occurred within limited time. For this reason, it is better to split Hamiltonian into time-independent part (H_0) and time-dependent part ($H'(t)$). This is called interaction representation. The state vector should be identified in interaction representation. That state vector, $\Psi_I(t)$ is defined as follows:

$$|\Psi_{\mathrm{I}}(t)\rangle \equiv \mathrm{e}^{\frac{2\pi i}{h}H_0\cdot(t-t_0)}|\Psi(t)\rangle \ . \tag{2.49}$$

The equation of time dependence of $\Psi_I(t)$ is obtained by the following description. First, multiply $u_0(t,t_0)$ to equation (2.49) from left side.

$$u_0(t,t_0)|\Psi_{\mathrm{I}}(t)\rangle = \mathrm{e}^{-\frac{2\pi i}{h}H_0\cdot(t-t_0)}\mathrm{e}^{\frac{2\pi i}{h}H_0\cdot(t-t_0)}|\Psi(t)\rangle = |\Psi(t)\rangle \ . \tag{2.50}$$

Here, $u_0(t,t_0)$ is the time evolution operator of time-independent Hamiltonian, H_0. Substituting equation (2.50) to equation (2.33), the following equation is obtained.

$$\begin{aligned} &\frac{\partial}{\partial t}\{u_0(t,t_0)|\Psi_{\mathrm{I}}(t)\rangle\} \\ &= -\frac{2\pi i}{h}\{H_0 + H'(t)\}u_0(t,t_0)|\Psi_{\mathrm{I}}(t)\rangle \ . \end{aligned} \tag{2.51}$$

The left side of equation (2.51) is equal to

$$\frac{\partial}{\partial t}\{u_0(t,t_0)|\Psi_{\mathrm{I}}(t)\rangle\} = -\frac{2\pi i}{h}H_0\mathrm{e}^{-\frac{2\pi i}{h}H_0\cdot(t-t_0)}|\Psi_{\mathrm{I}}(t)\rangle + \mathrm{e}^{-\frac{2\pi i}{h}H_0\cdot(t-t_0)}\frac{\partial}{\partial t}|\Psi_{\mathrm{I}}(t)\rangle \ . \tag{2.52}$$

And the right side of equation (2.51) is equal to

$$-\frac{2\pi i}{h}\{H_0 + H'(t)\}u_0(t,t_0)|\Psi_{\mathrm{I}}(t)\rangle$$

$$= -\frac{2\pi i}{h}H_0 u_0(t,t_0)|\Psi_{\mathrm{I}}(t)\rangle - \frac{2\pi i}{h}H'(t)u_0(t,t_0)|\Psi_{\mathrm{I}}(t)\rangle \ . \tag{2.53}$$

From equation (2.51) to (2.53), the following equation is obtained.

$$\mathrm{e}^{-\frac{2\pi i}{h}H_0\cdot(t-t_0)}\frac{\partial}{\partial t}|\Psi_{\mathrm{I}}(t)\rangle = -\frac{2\pi i}{h}H'(t)u_0(t,t_0)|\Psi_{\mathrm{I}}(t)\rangle \ . \tag{2.54}$$

Multiply $u_0^*(t,t_0)$ to equation (2.54) from left side.

$$\frac{\partial}{\partial t}|\Psi_{\mathrm{I}}(t)\rangle = -\frac{2\pi i}{h}u_0^*(t,t_0)H'(t)u_0(t,t_0)|\Psi_{\mathrm{I}}(t)\rangle \ . \tag{2.55}$$

The interaction Hamiltonian $H_{\mathrm{I}}'(t)$ is identified as

$$H_{\mathrm{I}}'(t) \equiv u_0^*(t,t_0)H'(t)u_0(t,t_0) \ . \tag{2.56}$$

The time evolution operator in interaction representation is also defined as following.

$$|\Psi_{\mathrm{I}}(t)\rangle = u_{\mathrm{I}}(t,t_0)|\Psi_{\mathrm{I}}(t_0)\rangle \ . \tag{2.57}$$

$$u_{\mathrm{I}}(t,t_0)$$

$$= 1 + \sum_{\mathrm{n}=1}^{\infty}(-\frac{2\pi i}{h})^{\mathrm{n}} \times \int_{t_0}^{t}\int_{t_0}^{\tau_{\mathrm{n}}}\cdots\int_{t_0}^{\tau_2} H_{\mathrm{I}}'(\tau_{\mathrm{n}})H_{\mathrm{I}}'(\tau_{\mathrm{n}-1})\cdots H_{\mathrm{I}}'(\tau_1)\,\mathrm{d}\tau_{\mathrm{n}}\mathrm{d}\tau_{\mathrm{n}-1}\cdots\mathrm{d}\tau_1 \ . \tag{2.58}$$

Next, multiply $u_0(t,t_0)$ to equation (2.57) from left side.

$$u_0(t,t_0)|\Psi_{\mathrm{I}}(t)\rangle = u_0(t,t_0)u_{\mathrm{I}}(t,t_0)|\Psi_{\mathrm{I}}(t_0)\rangle \ . \tag{2.59}$$

From equation (2.50) and (2.59),

$$|\Psi(t)\rangle = u_0(t,t_0)u_{\mathrm{I}}(t,t_0)|\Psi_{\mathrm{I}}(t_0)\rangle \ . \tag{2.60}$$

Moreover, using a relation $|\Psi_{\mathrm{I}}(t_0)\rangle = |\Psi(t_0)\rangle$, the following equation is obtained.

$$|\Psi(t)\rangle = u_0(t,t_0)u_{\mathrm{I}}(t,t_0)|\Psi(t_0)\rangle \ . \tag{2.61}$$

From the comparison between equation (2.34) and (2.61), we can obtain the following relation.

$$u(t,t_0) = u_0(t,t_0)u_{\mathrm{I}}(t,t_0) \ . \tag{2.62}$$

Equation (2.62) means that the time evolution operator $u(t,t_0)$ is divided into time evolution operator under non-perturbation Hamiltonian $u_0(t,t_0)$ and time evolution operator in interaction representation $u_{\mathrm{I}}(t,t_0)$. From equation (2.58) and (2.61),

$$|\Psi(t)\rangle = u_0(t,t_0)$$

$$\times\left\{1+\sum_{\mathrm{n}=1}^{\infty}\left(-\frac{2\pi i}{h}\right)^{\mathrm{n}}\times\int_{t_0}^{t}\int_{t_0}^{\tau_{\mathrm{n}}}\cdots\int_{t_0}^{\tau_2}H_{\mathrm{I}}'(\tau_{\mathrm{n}})H_{\mathrm{I}}'(\tau_{\mathrm{n}-1})\cdots H_{\mathrm{I}}'(\tau_1)\,\mathrm{d}\tau_{\mathrm{n}}\mathrm{d}\tau_{\mathrm{n}-1}\cdots\mathrm{d}\tau_1\right\}$$

$$\times|\Psi(t_0)\rangle \ , \tag{2.63}$$

is acquired.

The order is the number of interaction Hamiltonian $H_{\mathrm{I}}'(t)$ and each order term is expressed as follows:

・0-th order

$$|\Psi^{(0)}(t)\rangle = u_0(t,t_0)|\Psi(t_0)\rangle \ . \tag{2.64}$$

・First order

$$|\Psi^{(1)}(t)\rangle = u_0(t,t_0)\left\{\left(-\frac{2\pi i}{h}\right)\int_{t_0}^{t} H_{\mathrm{I}}'(\tau_1)\mathrm{d}\tau_1\right\}|\Psi(t_0)\rangle$$

$$= u_0(t,t_0)\left\{\left(-\frac{2\pi i}{h}\right)\int_{t_0}^{t} u_0^*(\tau_1,t_0)H'(\tau_1)u_0(\tau_1,t_0)\mathrm{d}\tau_1\right\}|\Psi(t_0)\rangle$$

$$= \left(-\frac{2\pi i}{h}\right)\int_{t_0}^{t} u_0(t,t_0)u_0^*(\tau_1,t_0)H'(\tau_1)u_0(\tau_1,t_0)\mathrm{d}\tau_1\,|\Psi(t_0)\rangle\ .$$

(2.65)

Here,

$$u_0(t,t_0)u_0^*(\tau_1,t_0) = \mathrm{e}^{-\frac{2\pi i}{h}H_0\cdot(t-t_0)}\mathrm{e}^{\frac{2\pi i}{h}H_0\cdot(\tau_1-t_0)} = \mathrm{e}^{-\frac{2\pi i}{h}H_0\cdot(t-\tau_1)} = u_0(t,\tau_1)\ . \quad (2.66)$$

Therefore,

$$|\Psi^{(1)}(t)\rangle = \left(-\frac{2\pi i}{h}\right)\int_{t_0}^{t} u_0(t,\tau_1)H'(\tau_1)u_0(\tau_1,t_0)\mathrm{d}\tau_1 \times |\Psi(t_0)\rangle\ . \quad (2.67)$$

・Second order

$$|\Psi^{(2)}(t)\rangle = u_0(t,t_0)\left\{\left(-\frac{2\pi i}{h}\right)^{\mathbf{2}}\int_{t_0}^{t}\int_{t_0}^{\tau_2} H_{\mathrm{I}}'(\tau_2)\,H_{\mathrm{I}}'(\tau_1)\mathrm{d}\tau_2\mathrm{d}\tau_1\right\}|\Psi(t_0)\rangle\ .$$

(2.68)

$$u_0(t,t_0)H_{\mathrm{I}}'(\tau_2)H_{\mathrm{I}}'(\tau_1)$$

$$= u_0(t,t_0)u_0^*(\tau_2,t_0)H'(\tau_2)u_0(\tau_2,t_0) \times u_0^*(\tau_1,t_0)H'(\tau_1)u_0(\tau_1,t_0)$$

$$= u_0(t,t_0)u_0^*(\tau_2,t_0)H'(\tau_2)u_0(\tau_2,t_0) \times u_0^*(\tau_1,t_0)H'(\tau_1)u_0(\tau_1,t_0)$$

$$= u_0(t,\tau_2)H'(\tau_2)u_0(\tau_2,\tau_1)H'(\tau_1)u_0(\tau_1,t_0) \ . \tag{2.69}$$

From equation (2.68) and (2.69), the second-order state vector is

$$|\Psi^{(2)}(t)\rangle = \left(-\frac{2\pi i}{h}\right)^2 \int_{t_0}^{t}\int_{t_0}^{\tau_2} u_0(t,\tau_2)H'(\tau_2)u_0(\tau_2,\tau_1) \times H'(\tau_1)u_0(\tau_1,t_0)\mathrm{d}\tau_2\mathrm{d}\tau_1|\Psi(t_0)\rangle \ . \tag{2.70}$$

・n-th order

$$|\Psi^{(\mathrm{n})}(t)\rangle$$

$$= \left(-\frac{2\pi i}{h}\right)^{\mathrm{n}} \int_{t_0}^{t}\int_{t_0}^{\tau_{\mathrm{n}}}\cdots\int_{t_0}^{\tau_2} u_0(t,\tau_{\mathrm{n}})H'(\tau_{\mathrm{n}})u_0(\tau_{\mathrm{n}},\tau_{\mathrm{n}-1}) \times H'(\tau_{\mathrm{n}-1})\cdots H'(\tau_1)u_0(\tau_1,t_0)\mathrm{d}\tau_{\mathrm{n}}\mathrm{d}\tau_{\mathrm{n}-1}\cdots\mathrm{d}\tau_1|\Psi(t_0)\rangle \ . \tag{2.71}$$

We can understand the meaning of equation (2.71) as follows. The state vector evolves under non-perturbation Hamiltonian up to τ_1. At τ_1, the system interacts with light. After that, the state vector evolves again up to τ_2. And the state vector repeats this process many times.

2.8. Density matrix

In general, it is difficult to accurately describe the state vector of molecules in realistic systems because the molecules collide with each other and the state vector is modulated by the collision. This out of phase state is called “mixed state”. In order to appropriately describe the mixed state, we have to use a density matrix, which takes account for the quantum mechanical time evolution and statistics.

The density matrix ρ is identified as the following equation:

$$\rho \equiv \sum_{s} p(s)|\Psi^s\rangle\langle\Psi^s| \, .$$

(2.72)

Where, s represents a state which has a certain phase relation and Ψ^s is the state vector in the s state, p(s) is the probability that system is in the s state. Next, expand the state vector by the eigenfunction, |k>.

$$|\Psi^s\rangle = \sum_{k} c_k^s |k\rangle \, .$$

(2.73)

The bra vector of equation (2.73) is

$$\langle\Psi^s| = \sum_{l} c_l^{s*} \langle l| \, .$$

(2.74)

From equation (2.72) to (2.74), the density matrix is expressed by equation (2.75).

$$\rho = \sum_{s} p(s)\left(\sum_{k} c_k^s |k\rangle\right)\left(\sum_{l} c_l^{s*} \langle l|\right)$$

$$= \sum_{kl}\sum_{s} p(s) c_k^s c_l^{s*} |k\rangle\langle l| \, .$$

(2.75)

The matrix element of the density matrix ρ_{nm} is given by the following equation:

$$\rho_{nm} = \langle n|\rho|m\rangle$$

$$= \sum_{kl} \sum_{s} p(s) c_k^s c_l^{s*} \langle n|k\rangle\langle l|m\rangle$$

$$= \sum_{kl} \sum_{s} p(s) c_k^s c_l^{s*} \delta_{nk} \delta_{lm}$$

$$= \sum_{s} p(s) c_n^s c_m^{s*} .$$

(2.76)

And a diagonal component of the matrix element is

$$\rho_{nn} = \sum_{s} p(s) |c_n^s|^2 .$$

(2.77)

The diagonal component of density matrix element ρ_{nn} expresses the probability that system occupies the state |n>. In other words, ρ_{nn} corresponds to the population of state |n>. On the other hand, the non-diagonal component ρ_{nm} is not zero in the case that both c^s_n and c^s_m are not zero. This is related to coherence between different energy levels.

The expectation value of observable *A* is written as the following relation:

$$\overline{\langle A \rangle} = \sum_{s} p(s) \langle A \rangle_s .$$

(2.78)

The quantum expectation value of *A* in the s state is

$$\langle A \rangle_s = \langle \Psi^s | A | \Psi^s \rangle$$

$$= \left(\sum_{m} c_m^{s*} \langle m| \right) A \left(\sum_{n} c_n^s |n\rangle \right)$$

$$= \left(\sum_{\mathrm{m}} c_{\mathrm{m}}^{\mathrm{s}*}\langle \mathrm{m}|\right) A \left(\sum_{\mathrm{n}} c_{\mathrm{n}}^{\mathrm{s}}|\mathrm{n}\rangle\right)$$

$$= \sum_{\mathrm{mn}} c_{\mathrm{m}}^{\mathrm{s}} c_{\mathrm{n}}^{\mathrm{s}*}\langle \mathrm{n}|A|\mathrm{m}\rangle$$

$$= \sum_{\mathrm{mn}} c_{\mathrm{m}}^{\mathrm{s}} c_{\mathrm{n}}^{\mathrm{s}*} A_{\mathrm{mn}} \,.$$

(2.79)

Substituting equation (2.79) to equation (2.78), then we can obtain equation (2.80).

$$\overline{\langle A\rangle} = \sum_{\mathrm{s}} p(\mathrm{s}) \sum_{\mathrm{mn}} c_{\mathrm{m}}^{\mathrm{s}} c_{\mathrm{n}}^{\mathrm{s}*} A_{\mathrm{mn}}$$

$$= \sum_{\mathrm{mn}} \left(\sum_{\mathrm{s}} p(\mathrm{s}) c_{\mathrm{m}}^{\mathrm{s}} c_{\mathrm{n}}^{\mathrm{s}*}\right) A_{\mathrm{mn}}$$

$$= \sum_{\mathrm{mn}} \rho_{\mathrm{nm}}\, A_{\mathrm{mn}}$$

$$= \sum_{\mathrm{n}} \left(\sum_{\mathrm{m}} \rho_{\mathrm{nm}}\, A_{\mathrm{mn}}\right)$$

$$= \sum_{\mathrm{n}} (\rho A)_{\mathrm{nn}} = \mathrm{Tr}(\rho A) \,.$$

(2.80)

Equation (2.80) shows that the expectation value of observable A is given by trace of ρA. If the density matrix of system is acquired, the expectation value can be calculated by equation (2.80).

2.9. Time evolution of density matrix

As describe above, the density matrix provides the expectation value of observables. Then, in order to understand the time evolution of system, the time evolution of the density matrix is crucial.

First, assuming the case that probability distribution p(s) is time-independent:

$$\frac{\partial p(\mathrm{s})}{\partial t} = 0 \,. \tag{2.81}$$

Next, differentiate equation (2.72) with time.

$$\frac{\partial \rho}{\partial t} = \frac{\partial}{\partial t}\sum_{\mathrm{s}} p(\mathrm{s})|\Psi^{\mathrm{s}}\rangle\langle\Psi^{\mathrm{s}}|$$

$$= \sum_{\mathrm{s}} p(\mathrm{s})\left\{\left(\frac{\partial}{\partial t}|\Psi^{\mathrm{s}}\rangle\right)\langle\Psi^{\mathrm{s}}| + |\Psi^{\mathrm{s}}\rangle\left(\frac{\partial}{\partial t}\langle\Psi^{\mathrm{s}}|\right)\right\} \,. \tag{2.82}$$

Here, from equation (2.33),

$$\frac{\partial}{\partial t}|\Psi^{\mathrm{s}}\rangle = -\frac{2\pi i}{h}H(t)|\Psi^{\mathrm{s}}\rangle$$

$$\frac{\partial}{\partial t}\langle\Psi^{\mathrm{s}}| = \frac{2\pi i}{h}\langle\Psi^{\mathrm{s}}|H(t) \,. \tag{2.83}$$

are hold. Substituting equation (2.83) to equation (2.82), the following relation is obtained.

$$\frac{\partial \rho}{\partial t} = \sum_{\mathrm{s}} p(\mathrm{s})\left\{\left(-\frac{2\pi i}{h}H(t)|\Psi^{\mathrm{s}}\rangle\right)\langle\Psi^{\mathrm{s}}| + |\Psi^{\mathrm{s}}\rangle\left(\frac{2\pi i}{h}\langle\Psi^{\mathrm{s}}|H(t)\right)\right\}$$

$$= -\frac{2\pi i}{h}\left\{H(t)\sum_{s} p(s)|\Psi^s\rangle\langle\Psi^s| - \sum_{s} p(s)|\Psi^s\rangle\langle\Psi^s|H(t)\right\}$$

$$= -\frac{2\pi i}{h}\{H(t)\rho - \rho H(t)\} = -\frac{2\pi i}{h}[H(t),\rho]\,.$$

(2.84)

Where, [] is a commutator. Equation (2.84) is called Liouville equation, which describes the time evolution of density matrix.

2.10. Time evolution of system and optical transition

The time evolution of density matrix is given by equation (2.84). Here, let us define a Liouville operator $L(t)$ as the follows:

$$L(t)A \equiv [H(t),A] = H(t)A - AH(t)\ \ \textbf{.} \tag{2.85}$$

Then Liouville equation can be rewritten as

$$\frac{\partial\rho}{\partial t} = -\frac{2\pi i}{h}L(t)\rho(t)\,.$$

(2.86)

Superficially, equation (2.86) has same structure as equation (2.33). Therefore, the time evolution operator for density matrix $U(t,t_0)$ can be identified as

$$\rho(t) = U(t,t_0)\rho(t_0)\ \ \textbf{.} \tag{2.87}$$

From the same procedure for $u(t,t_0)$, the following equation is obtained.

$$U(t,t_0) = 1 + \sum_{\mathrm{n}=1}^{\infty} (-\frac{2\pi i}{h})^{\mathrm{n}}$$

$$\times \int_{t_0}^{t} \int_{t_0}^{\tau_{\mathrm{n}}} \cdots \int_{t_0}^{\tau_2} L(\tau_{\mathrm{n}}) L(\tau_{\mathrm{n}-1}) \cdots L(\tau_1)\, \mathrm{d}\tau_{\mathrm{n}} \mathrm{d}\tau_{\mathrm{n}-1} \cdots \mathrm{d}\tau_1 \,, \tag{2.88}$$

In the interaction representation, the right side of equation (2.86) can be written as

$$L(t)\rho(t) = [H(t), \rho(t)]$$

$$= [H_0 + H'(t), \rho(t)]$$

$$= \big(H_0 + H'(t)\big)\rho(t) - \rho(t)\big(H_0 + H'(t)\big)$$

$$= H_0\rho(t) - \rho(t)H_0 + H'(t)\rho(t) - \rho(t)H'(t)$$

$$= [H_0, \rho(t)] + [H'(t), \rho(t)] = L_0\rho(t) + L'(t)\rho(t) \ . \tag{2.89}$$

Where, L_0 and L' are the non-perturbation Liouville operator, perturbation Liouville operator, respectively.

As the state vector, the perturbation expansion of density matrix is expressed as follows:

・0-th

$$\rho^{(0)}(t) = U_0(t,t_0)\rho(t_0) \ . \tag{2.90}$$

・First order

$$\rho^{(1)}(t) = \left(-\frac{2\pi i}{h}\right) \int_{t_0}^{t} U_0(t,\tau_1) L'(\tau_1) u_0(\tau_1, t_0)\, \rho(t_0) \mathrm{d}\tau_1 \,. \tag{2.91}$$

・Second order

$$\rho^{(2)}(t) = \left(-\frac{2\pi i}{h}\right)^2 \int_{t_0}^{t}\int_{t_0}^{\tau_2} U_0(t,\tau_2)L'(\tau_2)U_0(\tau_2,\tau_1) \times L'(\tau_1)U_0(\tau_1,t_0)\rho(t_0)\mathrm{d}\tau_2\mathrm{d}\tau_1 \ . \quad (2.92)$$

2.11. Interaction between two-state system and light

From the description above, time evolution of the density matrix of two-state system can be calculated. State |i> and |f> are ground state and excited state of the system, respectively. And their eigen energy is hω_i/2π, hω_f/2π, respectively. Consider the case that all molecules occupy the state |i> at t=t_0. Therefore, the density matrix is

$$\rho(t_0) = \begin{pmatrix} \rho_{ii}(t_0) & \rho_{if}(t_0) \\ \rho_{fi}(t_0) & \rho_{ff}(t_0) \end{pmatrix} = \begin{pmatrix} \rho_{ii}(t_0) & 0 \\ 0 & 0 \end{pmatrix}. \quad (2.93)$$

During $t_0 \rightarrow t_1$, the system evolves under non-perturbation. Then

$$\rho^{(0)}(\tau_1) \equiv U_0(\tau_1,t_0)\rho(t_0)$$

$$= U_0(\tau_1,t_0)\begin{pmatrix} \rho_{ii}(t_0) & 0 \\ 0 & 0 \end{pmatrix}$$

$$= \begin{pmatrix} \rho_{ii}(t_0)\cdot e^{-\gamma_i(\tau_1-t_0)} & 0\cdot e^{-(i\omega_{if}+\gamma_{if})(\tau_1-t_0)} \\ 0\cdot e^{-(i\omega_{fi}+\gamma_{fi})(\tau_1-t_0)} & 0\cdot e^{-\gamma_f(\tau_1-t_0)} \end{pmatrix}$$

$$= \begin{pmatrix} \rho_{ii}(t_0) & 0 \\ 0 & 0 \end{pmatrix}, \quad (2.93)$$

where, γ_i, γ_f, γ_{if}, γ_{fi} are the population decay rate of state |i>, f> and phase relaxation rate between |i> and |f>, respectively. And ω_{if}, ω_{if} are a frequency (energy) difference between |i> and |f>. From third equation to fourth equation, γ_i was regarded as 0 because |i> is the ground state. Then, from equation (2.91) and (2.93),

$$\rho^{(1)}(t) = \left(-\frac{2\pi i}{h}\right)\int_{t_0}^{t} U_0(t,\tau_1)L'(\tau_1)\rho^{(0)}(\tau_1)\mathrm{d}\tau_1 \ ,$$

(2.94)

is obtained. $\rho^{(1)}(\tau_1)$ is given by the following calculation.

$$\rho^{(1)}(\tau_1) = L'(\tau_1)\rho^{(0)}(\tau_1) = \left[H'(\tau_1), \rho^{(0)}(\tau_1)\right] = H'(\tau_1)\rho^{(0)}(\tau_1) - \rho^{(0)}(\tau_1)H'(\tau_1) \ .$$

(2.95)

In order to calculate equation (2.95), let us consider the electric dipole interaction. The Hamiltonian is given by equation (2.96).

$$H'(t) = -\boldsymbol{\mu}\cdot\boldsymbol{E}(t) \ . \tag{2.96}$$

Using equation (2.95) and (2.96), $\rho^{(1)}(\tau_1)$ is calculated as follows:

$$\begin{aligned}\rho_{\mathrm{ii}}^{(1)}(\tau_1) &\equiv \langle \mathrm{i}|\rho^{(1)}(\tau_1)|\mathrm{i}\rangle \\ &= \langle \mathrm{i}\left|H'(\tau_1)\rho^{(0)}(\tau_1)\right|\mathrm{i}\rangle - \langle \mathrm{i}\left|\rho^{(0)}(\tau_1)H'(\tau_1)\right|\mathrm{i}\rangle \\ &= -\langle \mathrm{i}\left|\mu\rho^{(0)}(\tau_1)\right|\mathrm{i}\rangle E(\tau_1) + \langle \mathrm{i}\left|\rho^{(0)}(\tau_1)\mu\right|\mathrm{i}\rangle E(\tau_1) \ .\end{aligned} \tag{2.97}$$

Insert the identity operator I shown by equation (2.98) between μ and $\rho^{(0)}(\tau_1)$ in equation (2.97).

$$I \equiv |\mathrm{i}\rangle\langle \mathrm{i}| + |\mathrm{f}\rangle\langle \mathrm{f}| \ . \tag{2.98}$$

$$\begin{aligned}\rho_{\mathrm{ii}}^{(1)}(\tau_1) &= -\langle \mathrm{i}\left|\mu(|\mathrm{i}\rangle\langle \mathrm{i}| + |\mathrm{f}\rangle\langle \mathrm{f}|\rho^{(0)}(\tau_1)\right|\mathrm{i}\rangle E(\tau_1) \\ &\quad + \langle \mathrm{i}\left|\rho^{(0)}(\tau_1)(|\mathrm{i}\rangle\langle \mathrm{i}| + |\mathrm{f}\rangle\langle \mathrm{f}|\mu\right|\mathrm{i}\rangle E(\tau_1) \\ &= -\{\langle \mathrm{i}|\mu|\mathrm{i}\rangle\langle \mathrm{i}\left|\rho^{(0)}(\tau_1)\right|\mathrm{i}\rangle - \langle \mathrm{i}|\mu|\mathrm{f}\rangle\langle \mathrm{f}|\rho^{(0)}(\tau_1)|\mathrm{i}\rangle\}E(\tau_1)\end{aligned}$$

$$+\{\langle \mathrm{i}\left|\rho^{(0)}(\tau_1)\right|\mathrm{i}\rangle\langle \mathrm{i}|\mu|\mathrm{i}\rangle + \langle \mathrm{i}|\rho^{(0)}(\tau_1)|\mathrm{f}\rangle\langle \mathrm{f}|\mu|\mathrm{i}\rangle\}E(\tau_1)$$

$$= 0 \ . \tag{2.99}$$

Here, to simplify the calculation, μ and $E(t)$ are regarded as scalar quantity. And equation (2.93) was used for the calculation. In the same way, other components are calculated.

$$\rho_{\mathrm{if}}^{(1)}(\tau_1)$$

$$= -\{\langle \mathrm{i}|\mu|\mathrm{i}\rangle\langle \mathrm{i}\left|\rho^{(0)}(\tau_1)\right|\mathrm{f}\rangle + \langle \mathrm{i}|\mu|\mathrm{f}\rangle\langle \mathrm{f}|\rho^{(0)}(\tau_1)|\mathrm{f}\rangle\}E(\tau_1)$$

$$+\{\langle \mathrm{i}\left|\rho^{(0)}(\tau_1)\right|\mathrm{i}\rangle\langle \mathrm{i}|\mu|\mathrm{f}\rangle + \langle \mathrm{i}|\rho^{(0)}(\tau_1)|\mathrm{f}\rangle\langle \mathrm{f}|\mu|\mathrm{f}\rangle\}E(\tau_1)$$

$$= \rho_{\mathrm{ii}}^{(0)}(t_0)\mu_{\mathrm{if}}\, E(\tau_1) \ . \tag{2.100}$$

$$\rho_{\mathrm{fi}}^{(1)}(\tau_1)$$

$$= -\{\langle \mathrm{f}|\mu|\mathrm{i}\rangle\langle \mathrm{i}\left|\rho^{(0)}(\tau_1)\right|\mathrm{i}\rangle + \langle \mathrm{f}|\mu|\mathrm{f}\rangle\langle \mathrm{f}|\rho^{(0)}(\tau_1)|\mathrm{i}\rangle\}E(\tau_1)$$

$$+\{\langle \mathrm{f}\left|\rho^{(0)}(\tau_1)\right|\mathrm{i}\rangle\langle \mathrm{i}|\mu|\mathrm{i}\rangle + \langle \mathrm{f}|\rho^{(0)}(\tau_1)|\mathrm{f}\rangle\langle \mathrm{f}|\mu|\mathrm{i}\rangle\}E(\tau_1)$$

$$= -\rho_{\mathrm{ii}}^{(0)}(t_0)\mu_{\mathrm{fi}}E(\tau_1) \ . \tag{2.101}$$

$$\rho_{\mathrm{ff}}^{(1)}(\tau_1)$$

$$= -\{\langle \mathrm{f}|\mu|\mathrm{i}\rangle\langle \mathrm{i}\left|\rho^{(0)}(\tau_1)\right|\mathrm{f}\rangle + \langle \mathrm{f}|\mu|\mathrm{f}\rangle\langle \mathrm{f}|\rho^{(0)}(\tau_1)|\mathrm{f}\rangle\}E(\tau_1)$$

$$+\{\langle \mathrm{f}\left|\rho^{(0)}(\tau_1)\right|\mathrm{i}\rangle\langle \mathrm{i}|\mu|\mathrm{f}\rangle + \langle \mathrm{f}|\rho^{(0)}(\tau_1)|\mathrm{f}\rangle\langle \mathrm{f}|\mu|\mathrm{f}\rangle\}E(\tau_1)$$

$$= 0 \ . \tag{2.102}$$

Where, $\mu_{\mathrm{if}} \equiv \langle \mathrm{i}|\mu|\mathrm{f}\rangle$, $\mu_{\mathrm{fi}} \equiv \langle \mathrm{f}|\mu|\mathrm{i}\rangle$. From equation (2.99) to (2.102),

$$\rho^{(1)}(\tau_1) = \begin{pmatrix} 0 & \rho_{\mathrm{ii}}^{(0)}(t_0)\mu_{\mathrm{if}}\, E(\tau_1) \\ -\rho_{\mathrm{ii}}^{(0)}(t_0)\mu_{\mathrm{fi}} E(\tau_1) & 0 \end{pmatrix}, \tag{2.103}$$

is obtained. And by operating $U_0(t,\tau_1)$ to equation (2.103) from left side, equation (2.104) is acquired.

$$U_0(t,\tau_1)\rho^{(1)}(\tau_1)$$

$$= \begin{pmatrix} 0 & \rho_{\mathrm{ii}}^{(0)}(t_0)\mu_{\mathrm{if}}\, E(\tau_1) e^{(-i\omega_{\mathrm{if}}-\gamma_{\mathrm{if}})(t-\tau_1)} \\ -\rho_{\mathrm{ii}}^{(0)}(t_0)\mu_{\mathrm{fi}} E(\tau_1) e^{(-i\omega_{\mathrm{fi}}-\gamma_{\mathrm{fi}})(t-\tau_1)} & 0 \end{pmatrix}. \tag{2.104}$$

Finally, integrating equation (2.104) with τ_1, equation (2.105) is obtained.

$$\rho^{(1)}(t) = \begin{pmatrix} 0 & \rho_{\mathrm{if}}^{(1)}(t) \\ \rho_{\mathrm{fi}}^{(1)}(t) & 0 \end{pmatrix}. \tag{2.105}$$

Where,

$$\rho_{\mathrm{if}}^{(1)}(t) = \left(-\frac{2\pi i}{h}\right) \int_{t_0}^{t} \rho_{\mathrm{ii}}^{(0)}(t_0)\mu_{\mathrm{if}}\, E(\tau_1) e^{(-i\omega_{\mathrm{if}}-\gamma_{\mathrm{if}})(t-\tau_1)}\, d\tau_1 . \tag{2.106}$$

$$\rho_{\mathrm{fi}}^{(1)}(t) = -\left(-\frac{2\pi i}{h}\right) \int_{t_0}^{t} \rho_{\mathrm{ii}}^{(0)}(t_0)\mu_{\mathrm{fi}}\, E(\tau_1) e^{(-i\omega_{\mathrm{fi}}-\gamma_{\mathrm{fi}})(t-\tau_1)}\, d\tau_1 . \tag{2.107}$$

In general, the n-th order density matrix is expressed by equation (2.108).

$$\rho_{\mathrm{cb}}^{(\mathrm{n})}(t) = \left(-\frac{2\pi i}{h}\right)\int_{t_0}^{t} e^{(-i\omega_{\mathrm{cb}}-\gamma_{\mathrm{cb}})(t-\tau_{\mathrm{n}})}\left\{[-\mu_{\mathrm{ca}}E(\tau_n)]\rho_{\mathrm{ab}}^{(\mathrm{n}-1)}(\tau_{\mathrm{n}})\right\}d\tau_{\mathrm{n}}.$$

$$\rho_{\mathrm{ac}}^{(\mathrm{n})}(t) = \left(-\frac{2\pi i}{h}\right)\int_{t_0}^{t} e^{(-i\omega_{\mathrm{ac}}-\gamma_{\mathrm{ac}})(t-\tau_{\mathrm{n}})}\left\{\rho_{\mathrm{ab}}^{(\mathrm{n}-1)}(\tau_{\mathrm{n}})[-\mu_{\mathrm{bc}}E(\tau_n)]\right\}d\tau_{\mathrm{n}}.$$

(2.108)

2.12. Light absorption

Light absorption is a fundamental optical process and a good example for calculation of the density matrix.

The initial density matrix is

$$\rho(t_0) = \begin{pmatrix}\rho_{\mathrm{ii}}(t_0) & 0\\ 0 & 0\end{pmatrix}\ . \tag{2.109}$$

And the electric field of incident light is

$$E(t) = \sum_{\mathrm{p}} E(\omega_{\mathrm{p}})\, e^{-i\omega_{\mathrm{p}}t}\ .$$

(2.110)

Then, calculate the first order density matrix by using equation (2.107).

$$\rho_{\mathrm{fi}}^{(1)}(t) = -(-\frac{2\pi i}{h})\int_{t_0}^{t}\rho_{\mathrm{ii}}^{(0)}(\tau_1)\mu_{\mathrm{fi}}\,E(\tau_1)e^{(-i\omega_{\mathrm{fi}}-\gamma_{\mathrm{fi}})(t-\tau_1)}\,d\tau_1$$

$$= -(-\frac{2\pi i}{h})\int_{t_0}^{t}\rho_{\mathrm{ii}}(t_0)\mu_{\mathrm{fi}}\,(\sum_{\mathrm{p}}E(\omega_{\mathrm{p}})\,e^{-i\omega_{\mathrm{p}}\tau_1})\times e^{(-i\omega_{\mathrm{fi}}-\gamma_{\mathrm{fi}})(t-\tau_1)}\,d\tau_1$$

$$= \frac{2\pi i}{h}\rho_{\mathrm{ii}}(t_0)\mu_{\mathrm{fi}}e^{(-i\omega_{\mathrm{fi}}-\gamma_{\mathrm{fi}})t}\sum_{\mathrm{p}}E(\omega_{\mathrm{p}})\times\int_{t_0}^{t}e^{[i(\omega_{\mathrm{fi}}-\omega_{\mathrm{p}})+\gamma_{\mathrm{fi}}]\tau_1}\,d\tau_1\ .$$

(2.111)

Here,

$$\int_{t_0}^{t} e^{[i(\omega_{\mathrm{fi}}-\omega_{\mathrm{p}})+\gamma_{\mathrm{fi}}]\tau_1}\, d\tau_1 = \left[\frac{e^{[i(\omega_{\mathrm{fi}}-\omega_{\mathrm{p}})+\gamma_{\mathrm{fi}}]\tau_1}}{i(\omega_{\mathrm{fi}}-\omega_{\mathrm{p}})+\gamma_{\mathrm{fi}}}\right]_{t_0}^{t}$$

$$= \frac{e^{[i(\omega_{\mathrm{fi}}-\omega_{\mathrm{p}})+\gamma_{\mathrm{fi}}]t}}{i(\omega_{\mathrm{fi}}-\omega_{\mathrm{p}})+\gamma_{\mathrm{fi}}} .$$

(2.112)

In equation (2.112), t_0 was regarded as $t_0 \to -\infty$. From equation (2.111) and (2.112),

$$\rho_{\mathrm{fi}}^{(1)}(t) = \frac{2\pi}{h}\rho_{\mathrm{ii}}(t_0)\sum_{\mathrm{p}}\frac{\mu_{\mathrm{fi}}E(\omega_{\mathrm{p}})}{(\omega_{\mathrm{fi}}-\omega_{\mathrm{p}})-i\gamma_{\mathrm{fi}}}e^{-i\omega_{\mathrm{p}}t} ,$$

(2.113)

is obtained. $\rho_{\mathrm{if}}^{(1)}$ is the complex conjugate of equation (2.113).

$$\rho_{\mathrm{if}}^{(1)}(t) = \frac{2\pi}{h}\rho_{\mathrm{ii}}(t_0)\sum_{\mathrm{p}}\frac{\mu_{\mathrm{if}}E(\omega_{\mathrm{p}})}{(\omega_{\mathrm{fi}}+\omega_{\mathrm{p}})+i\gamma_{\mathrm{fi}}}e^{-i\omega_{\mathrm{p}}t} .$$

(2.114)

Where, following relations were used and $-\omega_{\mathrm{p}}$ was replaced to ω_{p}.

$$\rho_{\mathrm{ii}}(t) = \rho_{\mathrm{ii}}{}^{*}(t_0) .$$

$$\mu_{if} = \mu_{fi}{}^{*} .$$

$$E(-\omega_{\mathrm{P}}) = E(\omega_{\mathrm{P}})^{*} .$$

(2.115)

Only the $\rho_{\mathrm{if}}^{(1)}$ and $\rho_{\mathrm{fi}}^{(1)}$ are produced by the interaction between matter and light.

The macroscopic first order polarization is given by the following equation.

$$P^{(1)}(t) = N\langle\mu\rangle$$

$$= N \cdot \mathrm{Tr}[\rho^{(1)}(t)\mu]$$

$$= N\sum_{\mathrm{nm}} \rho_{\mathrm{nm}}^{(1)}(t)\mu_{\mathrm{mn}}$$

$$= N(\rho_{\mathrm{if}}^{(1)}(t)\mu_{\mathrm{fi}} + \rho_{\mathrm{fi}}^{(1)}(t)\mu_{\mathrm{if}})$$

$$= N\frac{2\pi}{h}\rho_{\mathrm{ii}}(t_0)\sum_{\mathrm{p}}\{\frac{\mu_{\mathrm{fi}}\mu_{\mathrm{if}}E(\omega_{\mathrm{p}})}{(\omega_{\mathrm{fi}}+\omega_{\mathrm{p}})+i\gamma_{\mathrm{fi}}} + \frac{\mu_{\mathrm{if}}\mu_{\mathrm{fi}}E(\omega_{\mathrm{p}})}{(\omega_{\mathrm{fi}}-\omega_{\mathrm{p}})-i\gamma_{\mathrm{fi}}}\}e^{-i\omega_{\mathrm{p}}t}\,.$$

(2.116)

And the polarization is also expressed by the following equation:

$$P^{(1)}(t) = \sum_{\mathrm{p}} P^{(1)}(\omega_{\mathrm{p}})e^{-i\omega_{\mathrm{p}}t}\,.$$

(2.117)

From a comparison between equation (2.116) and (2.117), $P^{(1)}(\omega_{\mathrm{p}})$ is shown by equation (2.118).

$$P^{(1)}(\omega_{\mathrm{p}}) = N\frac{2\pi}{h}\rho_{\mathrm{ii}}(t_0)\left\{\frac{\mu_{\mathrm{fi}}\mu_{\mathrm{if}}}{(\omega_{\mathrm{fi}}+\omega_{\mathrm{p}})+i\gamma_{\mathrm{fi}}} + \frac{\mu_{\mathrm{if}}\mu_{\mathrm{fi}}}{(\omega_{\mathrm{fi}}-\omega_{\mathrm{p}})-i\gamma_{\mathrm{fi}}}\right\}E(\omega_{\mathrm{p}})\,.$$

(2.118)

From equation (2.21) and (2.118),

$$\chi^{(1)}(\omega_{\mathrm{p}}) = N\frac{2\pi}{\varepsilon_0 h}\rho_{\mathrm{ii}}(t_0)\left\{\frac{\mu_{\mathrm{fi}}\mu_{\mathrm{if}}}{(\omega_{\mathrm{fi}}+\omega_{\mathrm{p}})+i\gamma_{\mathrm{fi}}} + \frac{\mu_{\mathrm{if}}\mu_{\mathrm{fi}}}{(\omega_{\mathrm{fi}}-\omega_{\mathrm{p}})-i\gamma_{\mathrm{fi}}}\right\},$$

(2.119)

is obtained and equation (2.119) expresses the linear susceptibility. When ω_p is close to ω_{fi}, the second term of equation (2.119) is much larger than the first term. For this reason, second term is called a resonant term. When ω_p is close to the resonant frequency, by rationalize the resonant term, we can obtain equation (2.120).

$$\chi^{(1)}(\omega_p) \approx N\frac{2\pi}{\varepsilon_0 h}\rho_{ii}(t_0)|\mu_{fi}|^2\frac{(\omega_{fi}-\omega_p)+i\gamma_{fi}}{(\omega_{fi}-\omega_p)^2+{\gamma_{fi}}^2}. \tag{2.120}$$

Real part and imaginary part of equation (2.120) have frequency dependence of dispersive type and Lorentz type, respectively. The imaginary part is related to the absorption of light and therefore the spectral shape of absorption is expressed by Lorentz function.

2.13. Sum frequency generation

In this section, the second-order nonlinear susceptibility about sum frequency generation is discussed. Consider an energy diagram shown in Fig. 2.1.

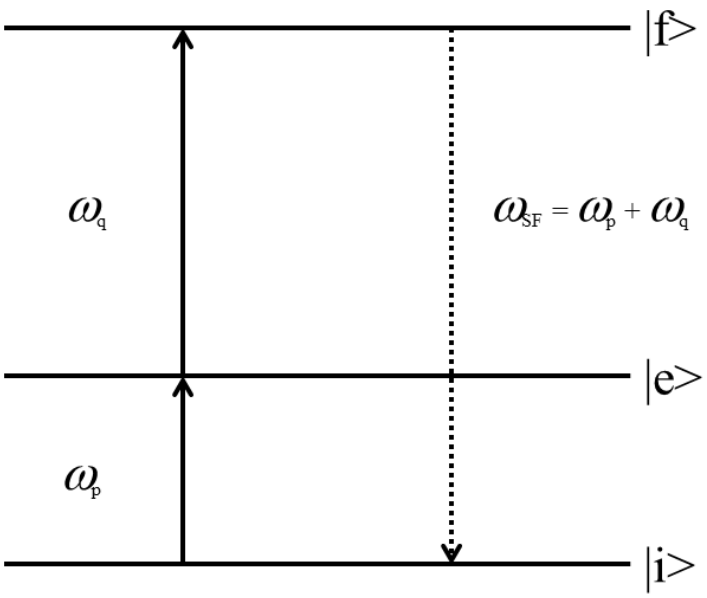

Fig. 2.1. Energy diagram for considering sum frequency generation.

From the calculation in section 2.12, the first order density matrix is given by equation (2.121).

$$\rho_{\mathrm{ei}}^{(1)}(t) = \frac{2\pi}{h}\rho_{\mathrm{ii}}(t_0)\sum_{\mathrm{p}}\frac{\mu_{\mathrm{ei}}E(\omega_{\mathrm{p}})}{(\omega_{\mathrm{ei}}-\omega_{\mathrm{p}})-i\gamma_{\mathrm{ei}}}e^{-i\omega_{\mathrm{p}}t}\,. \tag{2.121}$$

And the second-order density matrix is calculated from equation (2.108).

$$\rho_{\mathrm{fi}}^{(2)}(t) = (-\frac{2\pi i}{h})\int_{t_0}^{t} e^{(-i\omega_{\mathrm{fi}}-\gamma_{\mathrm{fi}})(t-\tau_2)}\left\{\rho_{\mathrm{ei}}^{(1)}(\tau_2)[-\mu_{\mathrm{fe}}E(\tau_2)]\right\}d\tau_2$$

$$= \left(-\frac{2\pi i}{h}\right) \int_{t_0}^{t} e^{(-i\omega_{\mathrm{fi}}-\gamma_{\mathrm{fi}})(t-\tau_2)} \left[-\mu_{\mathrm{fe}} \sum_{\mathrm{q}} E(\omega_{\mathrm{q}}) e^{-i\omega_{\mathrm{q}}\tau_2}\right]$$

$$\times \frac{2\pi}{h} \rho_{\mathrm{ii}}(t_0) \sum_{\mathrm{p}} \frac{\mu_{\mathrm{ei}} E(\omega_{\mathrm{p}})}{(\omega_{\mathrm{ei}} - \omega_{\mathrm{p}}) - i\gamma_{\mathrm{ei}}} e^{-i\omega_{\mathrm{p}}\tau_2}\, d\tau_2$$

$$= i\left(\frac{2\pi}{h}\right)^2 \rho_{\mathrm{ii}}(t_0) e^{(-i\omega_{\mathrm{fi}}-\gamma_{\mathrm{fi}})t} \sum_{\mathrm{pq}} \frac{\mu_{\mathrm{fe}} E(\omega_{\mathrm{q}}) \mu_{\mathrm{ei}} E(\omega_{\mathrm{p}})}{(\omega_{\mathrm{ei}} - \omega_{\mathrm{p}}) - i\gamma_{\mathrm{ei}}}$$

$$\times \int_{t_0}^{t} e^{[i(\omega_{\mathrm{fi}}-\omega_{\mathrm{p}}-\omega_{\mathrm{q}})+\gamma_{\mathrm{fi}})]\tau_2}\, d\tau_2$$

$$= i\left(\frac{2\pi}{h}\right)^2 \rho_{\mathrm{ii}}(t_0) e^{(-i\omega_{\mathrm{fi}}-\gamma_{\mathrm{fi}})t} \sum_{\mathrm{pq}} \frac{\mu_{\mathrm{fe}} E(\omega_{\mathrm{q}}) \mu_{\mathrm{ei}} E(\omega_{\mathrm{p}})}{(\omega_{\mathrm{ei}} - \omega_{\mathrm{p}}) - i\gamma_{\mathrm{ei}}}$$

$$\times \frac{e^{[i(\omega_{\mathrm{fi}}-\omega_{\mathrm{p}}-\omega_{\mathrm{q}})+\gamma_{\mathrm{fi}})]t}}{i(\omega_{\mathrm{fi}} - \omega_{\mathrm{p}} - \omega_{\mathrm{q}}) + \gamma_{\mathrm{fi}}}$$

$$= \left(\frac{2\pi}{h}\right)^2 \rho_{\mathrm{ii}}(t_0) \sum_{\mathrm{pq}} \frac{\mu_{\mathrm{fe}} E(\omega_{\mathrm{q}}) \mu_{\mathrm{ei}} E(\omega_{\mathrm{p}})}{(\omega_{\mathrm{ei}} - \omega_{\mathrm{p}} - i\gamma_{\mathrm{ei}})(\omega_{\mathrm{fi}} - \omega_{\mathrm{p}} - \omega_{\mathrm{q}} - i\gamma_{\mathrm{fi}})}$$

$$\times e^{-i(\omega_{\mathrm{p}}+\omega_{\mathrm{q}})t} \quad . \tag{2.122}$$

$\rho_{\mathrm{if}}^{(2)}$ is the complex conjugate of equation (2.122).

$$\rho_{\mathrm{if}}^{(2)}(t)$$

$$= \left(\frac{2\pi}{h}\right)^2 \rho_{\mathrm{ii}}(t_0) \sum_{\mathrm{pq}} \frac{\mu_{\mathrm{ef}} E(\omega_{\mathrm{q}}) \mu_{\mathrm{ie}} E(\omega_{\mathrm{p}})}{(\omega_{\mathrm{ei}} + \omega_{\mathrm{p}} + i\gamma_{\mathrm{ei}})(\omega_{\mathrm{fi}} + \omega_{\mathrm{p}} + \omega_{\mathrm{q}} + i\gamma_{\mathrm{ei}})} \times e^{-i(\omega_{\mathrm{p}}+\omega_{\mathrm{q}})t} \quad .$$

(2.123)

The second-order nonlinear polarization is

$$P^{(2)}(t) = N \cdot \mathrm{Tr}[\rho^{(2)}(t)\mu] = N(\rho_{\mathrm{fi}}^{(2)}(t)\mu_{\mathrm{if}} + \rho_{\mathrm{if}}^{(2)}(t)\mu_{\mathrm{fi}})$$

$$= N(\frac{2\pi}{h})^2 \rho_{\mathrm{ii}}(t_0) \sum_{\mathrm{pq}} \{ \frac{\mu_{\mathrm{if}} \mu_{\mathrm{fe}} \mu_{\mathrm{ei}} E(\omega_{\mathrm{p}}) E(\omega_{\mathrm{q}})}{(\omega_{\mathrm{ei}} - \omega_{\mathrm{p}} - i\gamma_{\mathrm{ei}})(\omega_{\mathrm{fi}} - \omega_{\mathrm{p}} - \omega_{\mathrm{q}} - i\gamma_{\mathrm{fi}})}$$

$$+ \frac{\mu_{\mathrm{ie}} \mu_{\mathrm{ef}} \mu_{\mathrm{fi}} E(\omega_{\mathrm{p}}) E(\omega_{\mathrm{q}})}{(\omega_{\mathrm{ei}} + \omega_{\mathrm{p}} + i\gamma_{\mathrm{ei}})(\omega_{\mathrm{fi}} + \omega_{\mathrm{p}} + \omega_{\mathrm{q}} + i\gamma_{\mathrm{fi}})} \} e^{-i(\omega_{\mathrm{p}} + \omega_{\mathrm{q}})t} \, .$$

(2.124)

$P^{(2)}(t)$ also can be written as

$$P^{(2)}(t) = \sum_{\mathrm{pq}} P^{(2)}(\omega_{\mathrm{p}} + \omega_{\mathrm{q}}) e^{-i(\omega_{\mathrm{p}} + \omega_{\mathrm{q}})t} \, .$$

(2.125)

From equation (2.124) and (2.125),

$$P^{(2)}(\omega_{\mathrm{p}} + \omega_{\mathrm{q}})$$

$$= N(\frac{2\pi}{h})^2 \rho_{\mathrm{ii}}(t_0) \{ \frac{\mu_{\mathrm{if}} \mu_{\mathrm{fe}} \mu_{\mathrm{ei}}}{(\omega_{\mathrm{ei}} - \omega_{\mathrm{p}} - i\gamma_{\mathrm{ei}})(\omega_{\mathrm{fi}} - \omega_{\mathrm{p}} - \omega_{\mathrm{q}} - i\gamma_{\mathrm{fi}})}$$

$$+ \frac{\mu_{\mathrm{ie}} \mu_{\mathrm{ef}} \mu_{\mathrm{fi}}}{(\omega_{\mathrm{ei}} + \omega_{\mathrm{p}} + i\gamma_{\mathrm{ei}})(\omega_{\mathrm{fi}} + \omega_{\mathrm{p}} + \omega_{\mathrm{q}} + i\gamma_{\mathrm{fi}})} \} E(\omega_{\mathrm{p}}) E(\omega_{\mathrm{q}})$$

$$\equiv \varepsilon_0 \chi^{(2)}(\omega_p + \omega_q;\ \omega_p, \omega_q) E(\omega_{\mathrm{p}}) E(\omega_{\mathrm{q}}) \ .$$

(2.126)

Therefore, the second-order nonlinear susceptibility is

$$\chi^{(2)}(\omega_{\mathrm{p}} + \omega_{\mathrm{q}};\ \omega_{\mathrm{p}}, \omega_{\mathrm{q}})$$

$$= \frac{N}{\varepsilon_0} (\frac{2\pi}{h})^2 \rho_{\mathrm{ii}}(t_0) \{ \frac{\mu_{\mathrm{if}} \mu_{\mathrm{fe}} \mu_{\mathrm{ei}}}{(\omega_{\mathrm{ei}} - \omega_{\mathrm{p}} - i\gamma_{\mathrm{ei}})(\omega_{\mathrm{fi}} - \omega_{\mathrm{p}} - \omega_{\mathrm{q}} - i\gamma_{\mathrm{fi}})}$$

$$+\frac{\mu_{\mathrm{ie}}\mu_{\mathrm{ef}}\mu_{\mathrm{fi}}}{(\omega_{\mathrm{ei}}+\omega_{\mathrm{p}}+i\gamma_{\mathrm{ei}})(\omega_{\mathrm{fi}}+\omega_{\mathrm{p}}+\omega_{\mathrm{q}}+i\gamma_{\mathrm{fi}})}\}.$$

(2.127)

Taking account for an intrinsic permutation symmetry, equation (2.127) can be rewritten as

$$\chi^{(2)}(\omega_p+\omega_q;\ \omega_p,\omega_q)$$

$$=\frac{N}{2\varepsilon_0}(\frac{2\pi}{h})^2\rho_{\mathrm{ii}}(t_0)\{\frac{\mu_{\mathrm{if}}\mu_{\mathrm{fe}}\mu_{\mathrm{ei}}}{(\omega_{\mathrm{ei}}-\omega_{\mathrm{p}}-i\gamma_{\mathrm{ei}})(\omega_{\mathrm{fi}}-\omega_{\mathrm{p}}-\omega_{\mathrm{q}}-i\gamma_{\mathrm{fi}})}$$

$$+\frac{\mu_{\mathrm{if}}\mu_{\mathrm{fe}}\mu_{\mathrm{ei}}}{(\omega_{\mathrm{ei}}-\omega_{\mathrm{q}}-i\gamma_{\mathrm{ei}})(\omega_{\mathrm{fi}}-\omega_{\mathrm{p}}-\omega_{\mathrm{q}}-i\gamma_{\mathrm{fi}})}$$

$$+\frac{\mu_{\mathrm{ie}}\mu_{\mathrm{ef}}\mu_{\mathrm{fi}}}{(\omega_{\mathrm{ei}}+\omega_{\mathrm{p}}+i\gamma_{\mathrm{ei}})(\omega_{\mathrm{fi}}+\omega_{\mathrm{p}}+\omega_{\mathrm{q}}+i\gamma_{\mathrm{fi}})}$$

$$+\frac{\mu_{\mathrm{ie}}\mu_{\mathrm{ef}}\mu_{\mathrm{fi}}}{(\omega_{\mathrm{ei}}+\omega_{\mathrm{q}}+i\gamma_{\mathrm{ei}})(\omega_{\mathrm{fi}}+\omega_{\mathrm{p}}+\omega_{\mathrm{q}}+i\gamma_{\mathrm{fi}})}\}.$$

(2.128)

When the |i> is a ground state, resonant term is dominant in equation (2.128), then equation (2.128) can be approximated to equation (2.129).

$$\chi^{(2)}(\omega_{\mathrm{p}}+\omega_{\mathrm{q}};\ \omega_{\mathrm{p}},\omega_{\mathrm{q}})$$

$$\approx\frac{N}{2\varepsilon_0}\left(\frac{2\pi}{h}\right)^2\rho_{\mathrm{ii}}(t_0)\{\frac{1}{(\omega_{\mathrm{ei}}-\omega_{\mathrm{p}}-i\gamma_{\mathrm{ei}})}$$

$$+\frac{1}{(\omega_{\mathrm{ei}}-\omega_{\mathrm{q}}-i\gamma_{\mathrm{ei}})}\}\cdot\frac{\mu_{\mathrm{if}}\mu_{\mathrm{fe}}\mu_{\mathrm{ei}}}{(\omega_{\mathrm{fi}}-\omega_{\mathrm{p}}-\omega_{\mathrm{q}}-i\gamma_{\mathrm{fi}})}.$$

(2.129)

In the vibrational resonant case, superficially $\chi^{(2)}$ is proportional to the second term of equation (2.129) (when ω_{q} represents infrared light).

$$\chi^{(2)}(\omega_{\mathrm{p}}+\omega_{\mathrm{q}};\ \omega_{\mathrm{p}},\omega_{\mathrm{q}}) \propto \frac{1}{(\omega_{\mathrm{ei}}-\omega_{\mathrm{q}}-i\gamma_{\mathrm{ei}})}$$

$$= \frac{(\omega_{\mathrm{ei}}-\omega_{\mathrm{q}}+i\gamma_{\mathrm{ei}})}{(\omega_{\mathrm{ei}}-\omega_{\mathrm{q}}-i\gamma_{\mathrm{ei}})(\omega_{\mathrm{ei}}-\omega_{\mathrm{q}}+i\gamma_{\mathrm{ei}})}$$

$$= \frac{\omega_{\mathrm{ei}}-\omega_{\mathrm{q}}}{(\omega_{\mathrm{ei}}-\omega_{\mathrm{q}})^2+{\gamma_{\mathrm{ei}}}^2} + \frac{i\gamma_{\mathrm{ei}}}{(\omega_{\mathrm{ei}}-\omega_{\mathrm{q}})^2+{\gamma_{\mathrm{ei}}}^2}\ .$$

(2.130)

Equation (2.130) has the same expression as equation (2.120). Therefore, even in the second-nonlinear optical processes, the real part of $\chi^{(2)}$ (Re$\chi^{(2)}$) has a dispersive spectral shape and the imaginary part of $\chi^{(2)}$ (Im$\chi^{(2)}$) has an absorptive (Lorentz) spectral shape. And as the same manner as the linear optical process, Im$\chi^{(2)}$ provides information about light absorption of matter.

2.14. Sum frequency generation and second-order nonlinear susceptibility

The intensity of SF light is detected in conventional SFG spectroscopy. This means that only the absolute square of the second-order nonlinear susceptibility is obtained through the experiment [43].

$$I_{SF} = \frac{\omega_{\mathrm{SF}}^2}{4c^2 n(\omega_{\mathrm{SF}})^2 \cos^2\theta_{\mathrm{r,SF}}} |\chi_{\mathrm{eff}}^{(2)}|^2 |E(\omega_1)E(\omega_2)|^2\ .$$

(2.131)

Where, c, $n(\omega_{\mathrm{SF}})$, $\theta_{\mathrm{r,SF}}$, are the speed of light in vacuum, refractive index of upper bulk media for SF light, reflection angle of SF light, respectively. And $\chi^{(2)}{}_{\mathrm{eff}}$ is expressed by equation (2.132).

$$\chi_{\mathrm{eff}}^{(2)} \propto F_{\mathrm{I}}(\omega_{\mathrm{SF}})F_{\mathrm{J}}(\omega_1)F_{\mathrm{K}}(\omega_2)\chi_{\mathrm{IJK}}^{(2)}\ .$$ (2.132)

Where, $F(\omega)$ is a Fresnel factor at frequency ω, $\chi^{(2)}{}_{\mathrm{IJK}}$ is the second-order nonlinear susceptibility in a laboratory frame. For rotationally isotropic interface, only the seven component, $\chi^{(2)}{}_{XXZ} = \chi^{(2)}{}_{YYZ}$, $\chi^{(2)}{}_{XZX} = \chi^{(2)}{}_{YZY}$, $\chi^{(2)}{}_{ZXX} = \chi^{(2)}{}_{ZYY}$, $\chi^{(2)}{}_{ZZZ}$ are non-zero [61, 62]. The Fresnel factor for each component

is given by the following formulas [61, 63, 64].

$$F_X(\omega_\mathrm{i}) = \frac{2n_1(\omega_\mathrm{i})\cos\gamma_\mathrm{i}}{n_1(\omega_\mathrm{i})\cos\gamma_\mathrm{i} + n_2(\omega_\mathrm{i})\cos\theta_\mathrm{i}}.$$

$$F_Y(\omega_\mathrm{i}) = \frac{2n_1(\omega_\mathrm{i})\cos\theta_\mathrm{i}}{n_1(\omega_\mathrm{i})\cos\theta_\mathrm{i} + n_2(\omega_\mathrm{i})\cos\gamma_\mathrm{i}}.$$

$$F_Z(\omega_\mathrm{i}) = \frac{2n_2(\omega_\mathrm{i})\cos\theta_\mathrm{i}}{n_1(\omega_\mathrm{i})\cos\gamma_\mathrm{i} + n_2(\omega_\mathrm{i})\cos\theta_\mathrm{i}} \cdot \left(\frac{n_1(\omega_\mathrm{i})}{n'(\omega_\mathrm{i})}\right).$$

(2.133)

Where, $n_1(\omega_\mathrm{i})$, $n_2(\omega_\mathrm{i})$ represent the refractive index of upper bulk media and lower bulk media at frequency ω_i. θ_i, γ_i are incident or reflection at frequency ω_i, refractive angle at frequency ω_i, respectively. $n'(\omega_\mathrm{i})$ is the effective refractive index parameter of interface. $\chi^{(2)}_{\mathrm{eff}}$ depends on the experimental condition, e. g., polarization and geometry in input and signal light. In common, the polarization combination of SF light, ω_1, and ω_2 is used in SFG literature. Namely, SSP, SPS, PSS, and PPP, and $\chi^{(2)}_{\mathrm{eff}}$ at each polarization combination is shown in the following formulas [65].

$$\chi^{(2)}_{\mathrm{eff,SSP}} = F_Y(\omega_\mathrm{SF})F_Y(\omega_1)F_Z(\omega_2)\sin\theta_2\chi^{(2)}_{YYZ}.$$

$$\chi^{(2)}_{\mathrm{eff,SPS}} = F_Y(\omega_\mathrm{SF})F_Z(\omega_1)F_Y(\omega_2)\sin\theta_1\chi^{(2)}_{YZY}.$$

$$\chi^{(2)}_{\mathrm{eff,PSS}} = F_Z(\omega_\mathrm{SF})F_Y(\omega_1)F_Y(\omega_2)\sin\theta_\mathrm{SF}\chi^{(2)}_{ZYY}.$$

$$\chi^{(2)}_{\mathrm{eff,PPP}} = -F_X(\omega_\mathrm{SF})F_X(\omega_1)F_Z(\omega_2)\cos\theta_\mathrm{SF}\cos\theta_1\sin\theta_2\chi^{(2)}_{XXZ}$$

$$-F_X(\omega_{\mathrm{SF}})F_Z(\omega_1)F_X(\omega_2)\cos\theta_{\mathrm{SF}}\sin\theta_1\cos\theta_2\chi^{(2)}_{XZX}$$

$$+F_Z(\omega_{\mathrm{SF}})F_X(\omega_1)F_X(\omega_2)\sin\theta_{\mathrm{SF}}\cos\theta_1\cos\theta_2\chi^{(2)}_{ZXX}$$

$$+F_Z(\omega_{\mathrm{SF}})F_Z(\omega_1)F_Z(\omega_2)\sin\theta_{\mathrm{SF}}\sin\theta_1\sin\theta_2\chi^{(2)}_{ZZZ}\ . \qquad (2.134)$$

Moreover, the second-order nonlinear susceptibility $\chi^{(2)}_{\mathrm{IJK}}$ is related to a hyperpolarizability β_{ijk} of the molecule in a molecular frame. The relation is expressed by the following equation [61].

$$\chi^{(2)}_{\mathrm{IJK}} = N_{\mathrm{s}}\sum_{\mathrm{ijk}}\langle R_{\mathrm{Ii}}R_{\mathrm{Jj}}R_{\mathrm{Kk}}\rangle\beta_{\mathrm{ijk}}\ . \qquad (2.135)$$

Here, < > denotes the ensemble average. N_{s} is number density of interfacial molecules. R is an element of the rotational matrix and given by following formula [65].

$$\begin{pmatrix} R_{Xx} & R_{Xy} & R_{Xz} \\ R_{Yx} & R_{Yy} & R_{Yz} \\ R_{Zx} & R_{Zy} & R_{Zz} \end{pmatrix}$$

$$= \begin{pmatrix} \cos\psi\cos\phi - \cos\theta\sin\phi\sin\psi & -\sin\psi\cos\phi - \cos\theta\sin\phi\cos\psi & \sin\theta\sin\phi \\ \cos\psi\sin\phi + \cos\theta\cos\phi\sin\psi & -\sin\psi\sin\phi + \cos\theta\cos\phi\cos\psi & -\sin\theta\cos\phi \\ \sin\theta\sin\psi & \sin\theta\cos\psi & \cos\theta \end{pmatrix}. \qquad (2.136)$$

Where, ψ, ϕ, θ are angle shown in figure 2.2.

When one focuses on a particular vibration mode of molecules, a hyperpolarizability is given by the following formula [38, 63].

$$\beta_{\mathrm{ijk}} = -\frac{1}{2\varepsilon_0\omega_{\mathrm{q}}}\frac{\partial\alpha_{\mathrm{ij}}}{\partial Q}\frac{\partial\mu_{\mathrm{k}}}{\partial Q}\ . \qquad (2.137)$$

Where, ω_q, α_{ij}, μ_k are the vibrational resonant frequency, Raman polarizability, and transition dipole moment of q-th vibration mode, respectively. And *Q* denotes the normal coordinate of the vibration mode. Equation (2.137) clearly shows that the SFG process is allowed only in both Raman and IR active vibration modes.

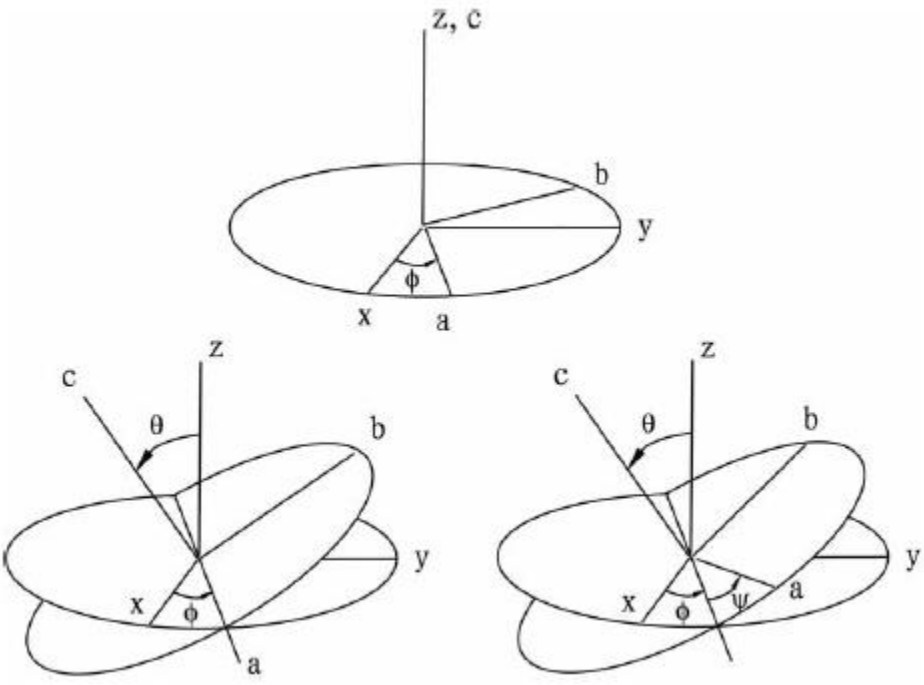

Fig. 2.2. Eular transformation between the laboratory frame and molecular frame [65].

3. Electrochemical heterodyne-detected vibrational sum frequency generation spectroscopy

3.1. HD-VSFG spectroscopy

In this study, a broadband VSFG scheme with multiplex detection is used for HD-VSFG spectroscopy. The spectral resolution in VSFG spectroscopy is governed by the narrower bandwidth of input two pulses. Thus a narrowband visible pulse and a broadband IR pulse are usually used for broadband VSFG spectroscopy. The narrow visible pulse determines the spectral resolution and the broad IR pulse covers the observation spectral region.

3.1.1. Background of HD-VSFG spectroscopy

In this study, I applied heterodyne-detected vibrational sum frequency generation (HD-VSFG) spectroscopy to electrolyte/electrode interfaces. HD-VSFG spectroscopy is a unique spectroscopic technique, which enable us to directly determine the phase and amplitude of electric field of SF light and provides $\chi^{(2)}$ as a complex number [40, 41, 43, 46, 47, 66-68]. In the HD-VSFG measurements, a narrowband visible beam ω_{vis}, a tunable broadband IR beam ω_{IR}, and an additional third light, local oscillator (LO), are input into a sample. LO is generated by inputting a visible beam and a IR beam into an inversion-symmetry broken media such as a y-cut quartz prior to the sample and has the same frequency as a SF beam from the sample ($\omega_{\mathrm{LO}}=\omega_{\mathrm{SFG}}$). The ω_{LO} is delayed by T compared to ω_{vis} and ω_{IR} by passing through a silica plate. The SF beam and delayed LO are introduced into a detector together. Then the total electric-field amplitude of SF light in a time domain is given by the following formula.

$$E_{\mathrm{total}}(t) = E_{\mathrm{SFG}}(t) + E_{\mathrm{LO}}(t+T)\ . \tag{3.1}$$

Where, E is an electric field of light, T is time delay between the SF beam and LO. Experimentally, only the intensity of SF light in a frequency domain is obtained. The interference pattern between the SF beam and LO in a frequency domain is expressed as follows.

$$\tilde{E}_{\mathrm{total}}(\omega) = \tilde{E}_{\mathrm{SFG}}(\omega) + \tilde{E}_{\mathrm{LO}}(\omega)e^{+i\omega T}. \tag{3.2}$$

Where, $\tilde{E}_{\mathrm{total}}(\omega)$ is a Fourier-transformed electric field. The obtained intensity is given by the

absolute square of equation (3.2).

$$\left|\tilde{E}_{\mathrm{total}}(\omega)\right|^2 = \left|\tilde{E}_{\mathrm{SFG}}(\omega)\right|^2 + \left|\tilde{E}_{\mathrm{LO}}(\omega)\right|^2 + \tilde{E}_{\mathrm{SFG}}(\omega)\tilde{E}^*_{\mathrm{LO}}(\omega)e^{-i\omega T} + \tilde{E}^*_{\mathrm{SFG}}(\omega)\tilde{E}_{\mathrm{LO}}(\omega)e^{+i\omega T} \quad . \tag{3.3}$$

The third term of equation (3.3) includes the electric field of SF light from the sample, E_{SFG} and this term can be extracted by a filtering function. This procedure is shown in figure 3.1c and figure 3.1d. The cross term in a frequency domain is obtained with inverse Fourier transformation of the third term of equation (3.3) after filtering. This procedure is shown in figure 3.1e and figure 3.1f.

In order to correct the phase and amplitude of the SF light, the sample spectrum needs to be normalized by a reference spectrum which is obtained with the same manner as the sample measurement. In particular, the optical propagation length of the reference measurement must be exactly the same as that of sample measurement, otherwise optical propagation length difference between $E_{\mathrm{SFG,\ sample}}$ and $E_{\mathrm{SFG,\ ref}}$ causes a phase error. The second-order nonlinear susceptibility $\chi^{(2)}{}_{\mathrm{obs}}$, which is experimentally obtained, is expresses by the following formula [43].

$$\chi^{(2)}_{\mathrm{obs}} = \frac{E_{\mathrm{SFG,sample}}E^*_{\mathrm{LO}}e^{-i\omega_{\mathrm{SF}}T}}{E_{\mathrm{SFG,ref}}E^*_{\mathrm{LO}}e^{-i\omega_{\mathrm{SF}}T}} = \frac{\chi^{(2)}_{\mathrm{sample}}}{\chi^{(2)}_{\mathrm{ref}}} \quad . \tag{3.4}$$

Obtained $\chi^{(2)}$ spectra contains vibrationally non-resonant and resonant contributions. When we focus on the vibrational resonance, equation (2.129) in chapter 2 can be rewritten as follows [43]:

$$\chi^{(2)} = \chi^{(2)}_{\mathrm{NR}} + \sum_{\mathrm{q}} \frac{A_{\mathrm{q}}}{\omega_{\mathrm{q}} - \omega_{\mathrm{IR}} - i\Gamma_{\mathrm{q}}} . \tag{3.5}$$

Where $\chi^{(2)}{}_{\mathrm{NR}}$ is a vibrationally non-resonant background, A_{q}, ω_{q}, Γ_{q} are the amplitude, frequency and damping constant of q-th vibration mode, respectively. Then, $\mathrm{Im}\chi^{(2)}$ is expressed by the following

formula [43].

$$\mathrm{Im}\chi^{(2)} = \mathrm{Im}\chi_{\mathrm{NR}}^{(2)} + \sum_{\mathrm{q}} \frac{A_{\mathrm{q}}\Gamma_{\mathrm{q}}}{(\omega_{\mathrm{q}} - \omega_{\mathrm{IR}})^2 + {\Gamma_{\mathrm{q}}}^2}. \tag{3.6}$$

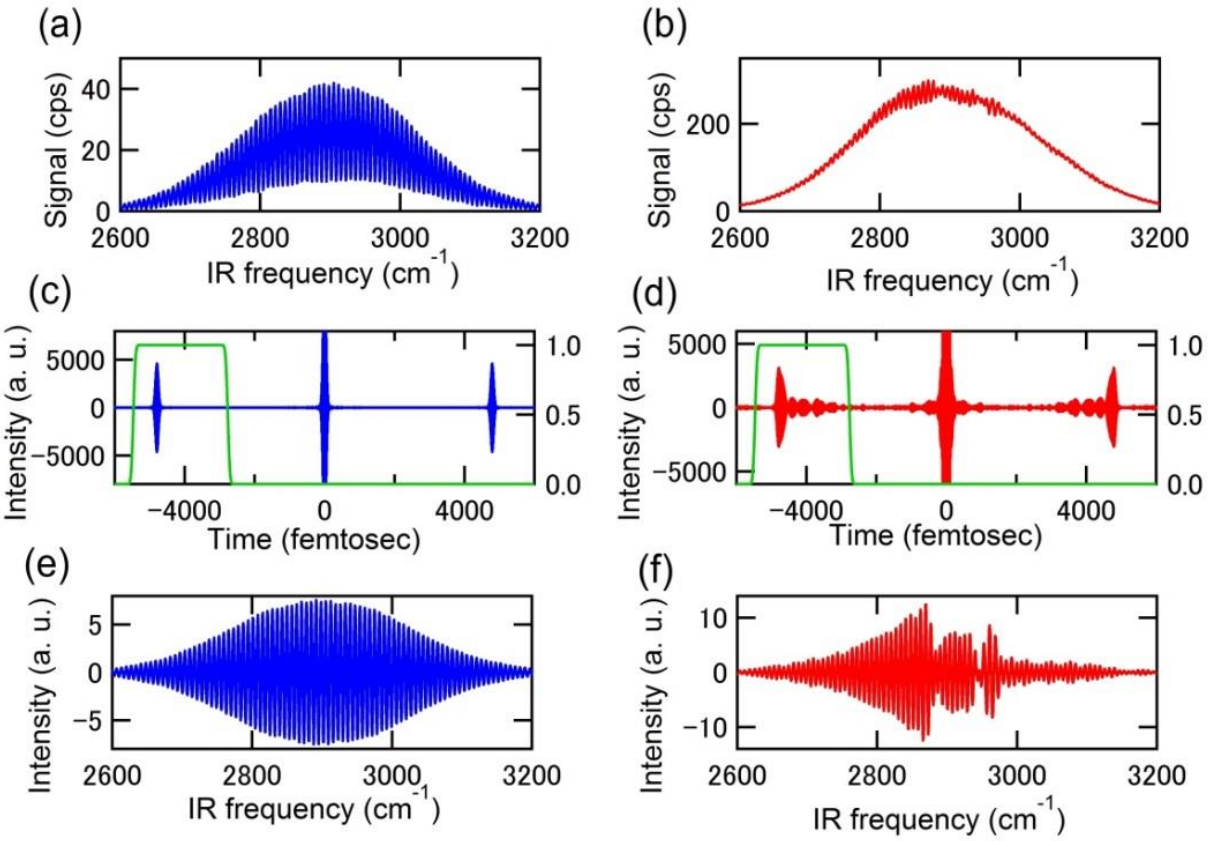

Fig. 3.1. Spectra and interferograms obtained in HD-VSFG measurements. (a, b) Raw spectra detected by CCD. (c, d) Time-domain interferogram obtained by Fourier transformation of (a) and (b). The green lines show the filtering function. (e, f) Filtered complex-fringe spectra. Only the real part is shown for clarity. (a), (b) and (c) are the spectra of the air/quartz whereas (b), (d) and (f) are the spectra of the air/1-octadecanethiol self-assembled monolayer on platinum. Figures are cited from SI of Ref [69].

3.1.2. Experimental setup

The schematic of optical setup of HD-VSFG measurements is shown in figure 3.2. The near-infrared light (center wavelength: 796 nm) is generated by Ti: sapphire regenerative amplifier (Solstice, Spectra Physics, pulse energy: ~3 mJ, repetition rate: 1 kHz, pulse width: <100 fs). The 2/3 of the output 796 nm-pulse was introduced into an optical parametric amplifier equipped with a difference frequency generation unit (TOPAS-prime, Spectra Physics) for generation of tunable broad band IR pulses (1000 - 4000 cm^{-1}, FWHM: ~250 cm^{-1}, shown in figure 3.1a and 3.1b), used as ω_{IR}. The other 1/3 of the output was narrowed (FWHM: ~5 cm^{-1}) by a 4f grating filter consisting of a holographic grating (1800 g/mm), mechanical slit and cylindrical lens (f = 300 mm), used as ω_{vis}. The ω_{vis} and ω_{IR} pulses were focused onto a thin plate of y-cut quartz (10 μm thick) and this generates a local oscillator, ω_{LO}. The ω_{LO} passes through a 3 mm thick silica plate which delays the ω_{LO} by T (~5 ps) compared to ω_{vis}, ω_{IR}. The ω_{vis}, ω_{IR} and ω_{LO} were focused onto a electrolyte/electrode interface with incident angle 29.9°, 26.6°, 29.3°, respectively. The generated SFG from electrode and reflected ω_{LO} were introduced to a polychromator (Andor Tech., SR303i-A) and detected by a CCD (Andor Tech., Newton DU970P). All measurements were performed with PPP combination (P-polarized ω_{SFG}, P-polarized ω_{vis}, P-polarized ω_{IR}). The electrochemistry part is described in the later section.

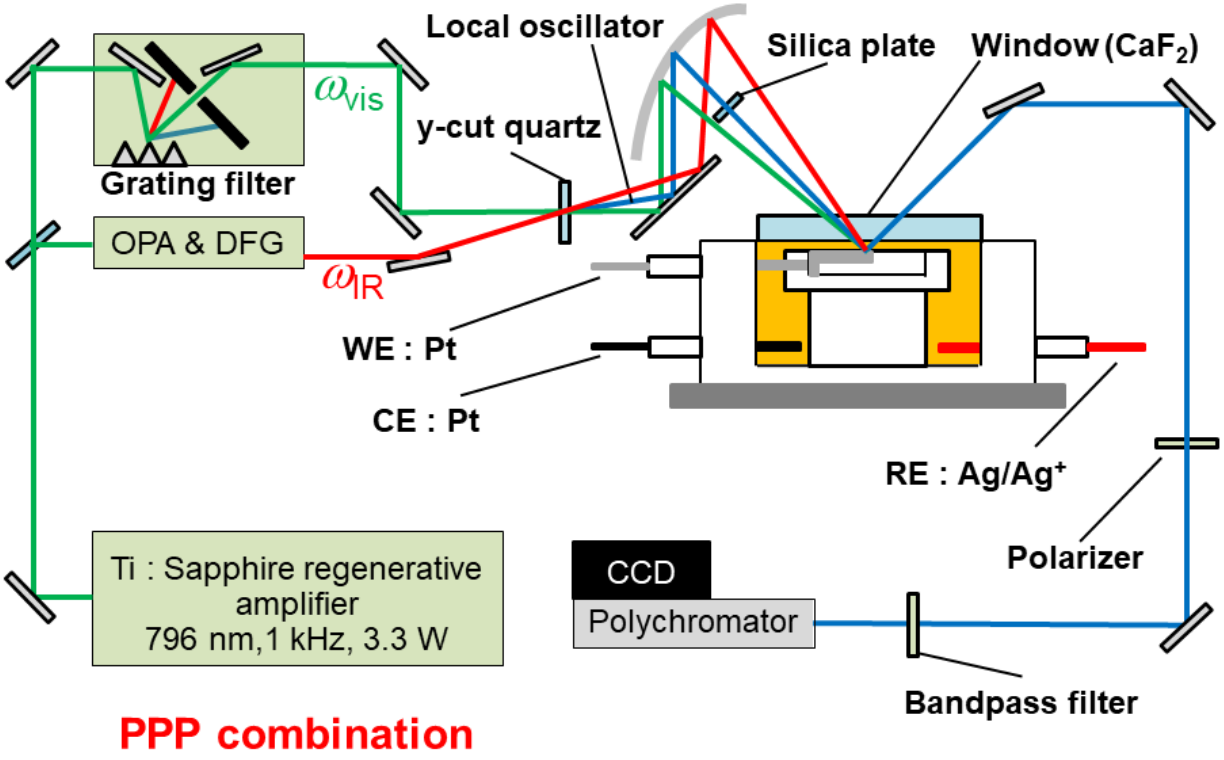

Fig. 3.2. Schematic of the optical setup. BS : Beam Splitter, SPF : Short Pass Filter.

3.2. Development of the spectro-electrochemical cell

3.2.1 Spectro-electrochemical cell

In order to perform a HD-VSFG measurement and an electrochemical measurement simultaneously, I developed a home-made spectro-electrochemical cell. The schematic of the spectro-electrochemical cell is shown in Fig. 3.3. The cell body is made of polypropylene. The visible, IR and LO pulses are incident from a CaF_2 optical-window side. The HD-VSFG measurements were performed with thin-layer electrolyte configuration in which the sample substrate was pushed against the optical window. The thickness of thin-layer electrolyte between the optical window and sample substrate was estimated from the absorbance of solvent and to be around 8 μm. The detail of calculation is described in the next section. The sample substrate was a z-cut quartz and about half of top surface of the z-cut quartz was covered by the polycrystalline platinum electrode deposited by an electron beam evaporator or an Ar sputter machine. This substrate was used as the working electrode. A platinum wire and a silver wire were used as the counter electrode and reference electrode, respectively. The potential of silver wire was calibrated by the redox potential of ferrocene/ferrocene$^+$ ($Fe(C_5H_5)_2/Fe(C_5H_5)_2^+$). According to a previous report, the redox potential of ferrocene/ferrocene$^+$ is +0.380 V vs saturated calomel electrode (SCE) [70]. The redox potential of ferrocene/ferrocene$^+$ is around +0.07 V against a non-aqueous $Ag^+/AgNO_3$ electrode (a silver wire immersed in 0.1 M tetrabutylammonium perchlorate/0.01 M $AgNO_3$ in acetonitrile). Therefore, the potential of $Ag^+/AgNO_3$ reference electrode is +0.37 V vs SCE. The estimated potential difference between the silver wire and $Ag^+/AgNO_3$ reference from O_2 redox potential is ca. 0.11 V (the silver wire is 0.11 V lower than $Ag^+/AgNO_3$ reference electrode). From the calculation above, the potential of the silver wire is around +0.26 V vs SCE. The cyclic voltammograms are shown in Fig. 3.4.

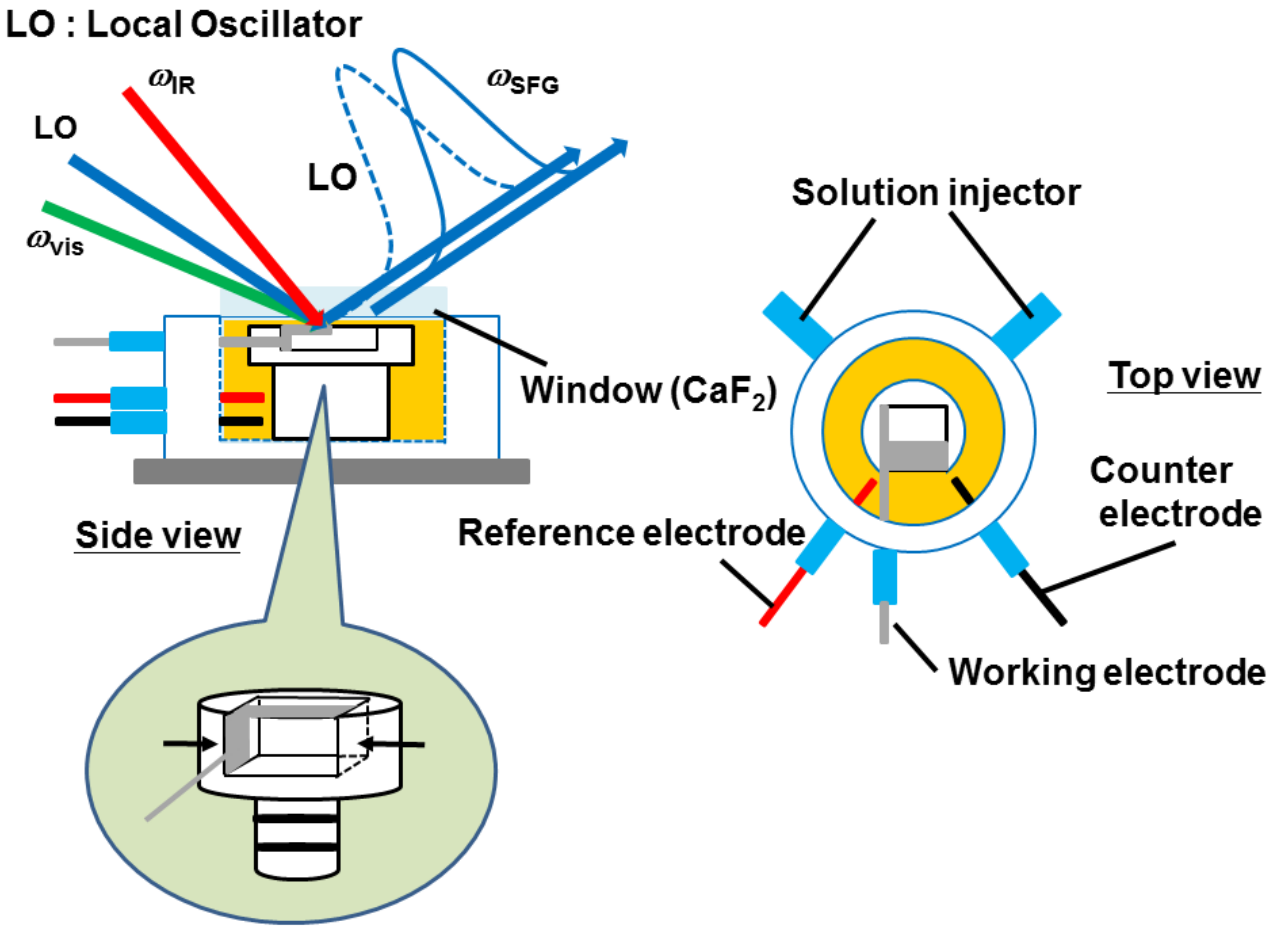

Fig. 3.3. Schematics of our home-made spectro-electrochemical cell.

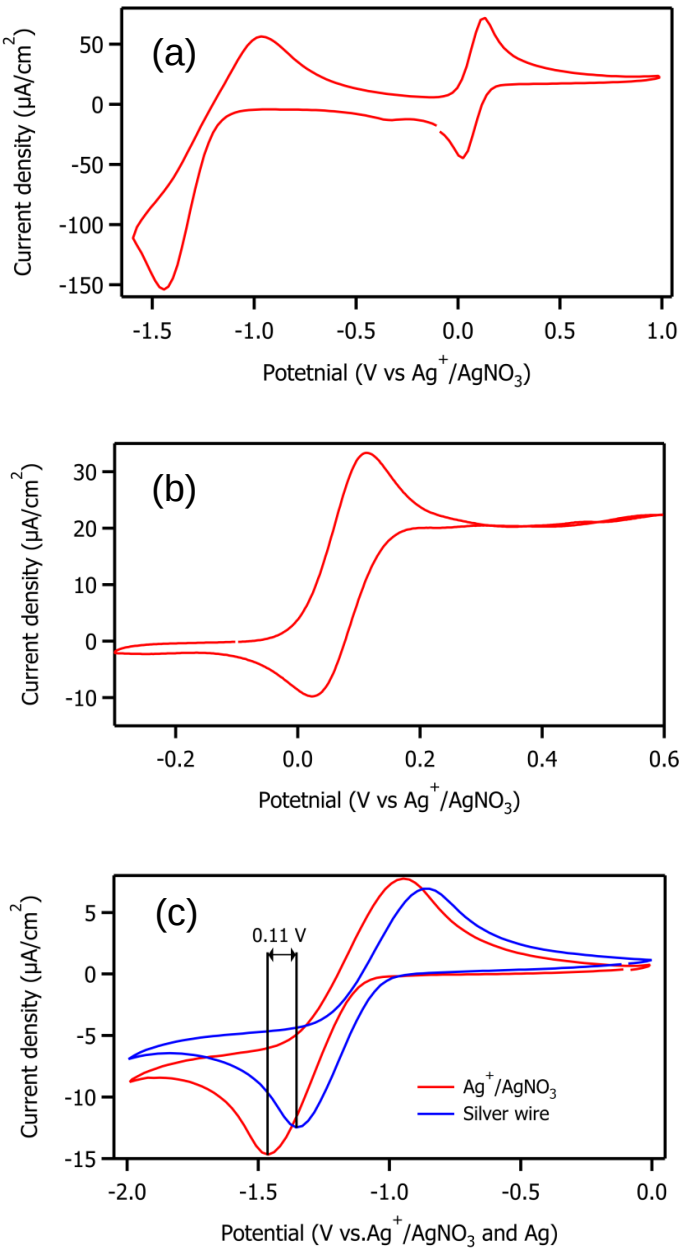

Fig. 3.4. (a) Cyclic voltammogram of 0.1 M tetrabutylammonium perchlorate/8 mM ferrocene in acetonitrile with O_2 bubbling. (b) Cyclic voltammogram in ferrocene redox potential region. (c) Cyclic voltammogram in O_2 redox potential region. The working electrode, counter electrode, reference electrode are carbon, platinum wire, $Ag^+/AgNO_3$ and the silver wire, respectively.

3.2.2. Estimation of the thickness of the solution layer.

The thickness of the solution layer is estimated from the IR absorption of the CN stretch vibration of acetonitrile, which is observed in the un-normalized raw homodyne-detected (conventional) VSFG spectrum of the acetonitrile/quartz interface, with the Lambert-Beer equation,

$$A = \varepsilon C l \ , \tag{3.7}$$

where, A, ε, C, l are the absorbance, molar extinction coefficient, concentration and optical path length, respectively. The actual procedure of our estimation is as follows.

The absorption of acetonitrile was evaluated from the spectrum of the acetonitrile/quartz interface which was used as the reference spectrum. Figure 3.5 shows the un-normalized raw homodyne-detected VSFG spectrum of the acetonitrile/quartz interface (red). The VSFG spectrum was fit to a Gaussian function (black), assuming a Gaussian spectral distribution of the input IR light. As clearly seen in this figure, a dip is recognized at 2250 cm^{-1}, which is due to the absorption of the CN stretch of acetonitrile in the solution layer. The transmittance was calculated to be 0.877 by dividing the observed signal intensity (red) with the fitted value (black) at 2250 cm^{-1}, and this evaluated transmittance was converted to absorbance,

$$A = -\log_{10} 0.877 = 0.0569 \ . \tag{3.8}$$

The molar extinction coefficient (ε) is calculated from the reported absorption cross section (σ~15×10^{-21} cm^2, [71]) of acetonitrile at 2250 cm^{-1} as,

$$\begin{aligned} \varepsilon &= (\log_{10} e)\sigma N_A = 0.434 \times 15 \times 10^{-21} \times 6.022 \times 10^{23} \\ &= 3.922 \times 10^3 \ \left[\frac{\mathrm{cm}^2}{\mathrm{mol}}\right] = 3.922 \times 10^{-1} \ \left[\frac{\mathrm{m}^2}{\mathrm{mol}}\right], \end{aligned} \tag{3.9}$$

where N_A is Avogadro constant. The molar concentration of acetonitrile is calculated as,

$$\begin{aligned} C = \frac{d\ [\mathrm{g\ m^{-3}}]}{M\ [\mathrm{g\ mol^{-1}}]} &= 0.786 \left[\frac{\mathrm{g}}{\mathrm{mL}}\right] \times 10^6 \left[\frac{\mathrm{mL}}{\mathrm{m}^3}\right] \times \frac{1}{41.05} \left[\frac{\mathrm{mol}}{\mathrm{g}}\right] \\ &= 19150 \left[\frac{\mathrm{mol}}{\mathrm{m}^3}\right] . \end{aligned} \tag{3.10}$$

Here, d and M are the density and molecular weight, respectively, and the values were taken from the safety data sheet (SDS) provided by Sigma-Aldrich.

Then, the optical path length was calculated using the obtained A, ε and C as,

$$l = \frac{A}{\varepsilon C} = \frac{0.0569}{3.922 \times 10^{-1} \times 19150} = 7.58 \times 10^{-6}\ [\mathrm{m}] \fallingdotseq 7.6\ [\mu\mathrm{m}]\ . \tag{3.11}$$

Consequently, the thickness of the solution layer was estimated to be ~8 μm.

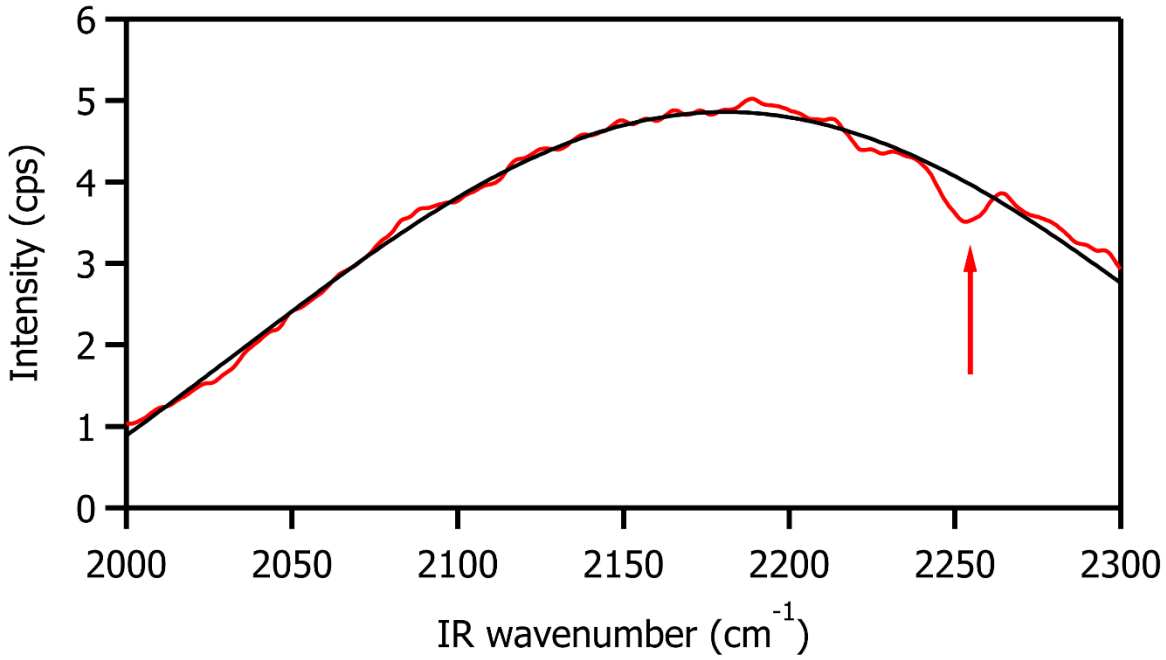

Fig. 3.5. Un-normalized raw homodyne-detected VSFG spectrum of the acetonitrile/quartz interface. The red curve shows the experimental data whereas the black curve is the fitting curve using a Gaussian function. A dip due to the absorption of acetonitrile in the solution layer is clearly recognized at 2250 cm^{-1} (marked by the red arrow).

3.2.3 Estimation of the actual surface area of electrode

A surface area of electrode is required for the evaluation of electric current density in cyclic voltammograms. Because an actual surface area is usually larger than a geometric surface area due to the roughness of electrode surface, it is important to estimate the actual area of working electrodes in cyclic voltammetry. For platinum electrodes, it is possible to calculate the actual surface area from the hydrogen desorption peak in a cyclic voltammogram with sulfuric acid aqueous solution. In this section, calculation of surface area is described for the platinum electrode used in the present study.

The cyclic voltammogram of 0.1 M sulfuric acid aqueous solution with a platinum working electrode is shown in Fig. 3.6a. The hydrogen desorption feature is marked by red arrows. For the estimation of the surface area, the amount of flowed charge (*Q*) through the hydrogen desorption is needed. The flowed charge is given by the following equation.

$$Q = \int_{t_1}^{t_2} I dt = \frac{1}{v}\int_{E_1}^{E_2} I dE \ .$$

(3.12)

Where, *I*, *t*, *v* and *E* are flowed electric current, time, sweep rate of cyclic voltammetry and electrode potential, respectively. To calculate the amount of the flowed charge, first, the area of hydrogen desorption peak in the cyclic voltammogram is calculated by integrating the region shown by diagonal lines in Fig.3.6b. The area was calculated to be 0.01151 [mA V]. In the present study, the sweep rate was 10 mV/s, thus the flowed charge is calculated as follows.

$$Q = \frac{1}{v}\int_{E_1}^{E_2} I dE = \frac{1}{10}\left[\frac{\mathrm{s}}{\mathrm{mV}}\right] \times 0.01151\ [\mathrm{mA\ V}]$$

$$= \frac{1}{10}\left[\frac{\mathrm{s}}{\mathrm{mV}}\right] \times 11.51\ [\mathrm{mA\ mV}]$$

$$= 1.151\ [\mathrm{mA\ s}] = 1.151 \times 10^3\ [\mu\mathrm{C}]$$

(3.13)

And the charge of hydrogen desorption is already known to be 210 [μC/cm^2] [72]. Then, the actual surface area is obtained as follows.

$$\frac{1}{210}\left[\frac{\mathrm{cm}^2}{\mu\mathrm{C}}\right] \times 1.151 \times 10^3\ [\mu\mathrm{C}] = 5.479 \fallingdotseq 5\ [\mathrm{cm}^2]$$

Therefore, the actual surface area of the platinum electrode is around 5 cm^2 in the present study. This value is used for normalizing measured current to obtain current density.

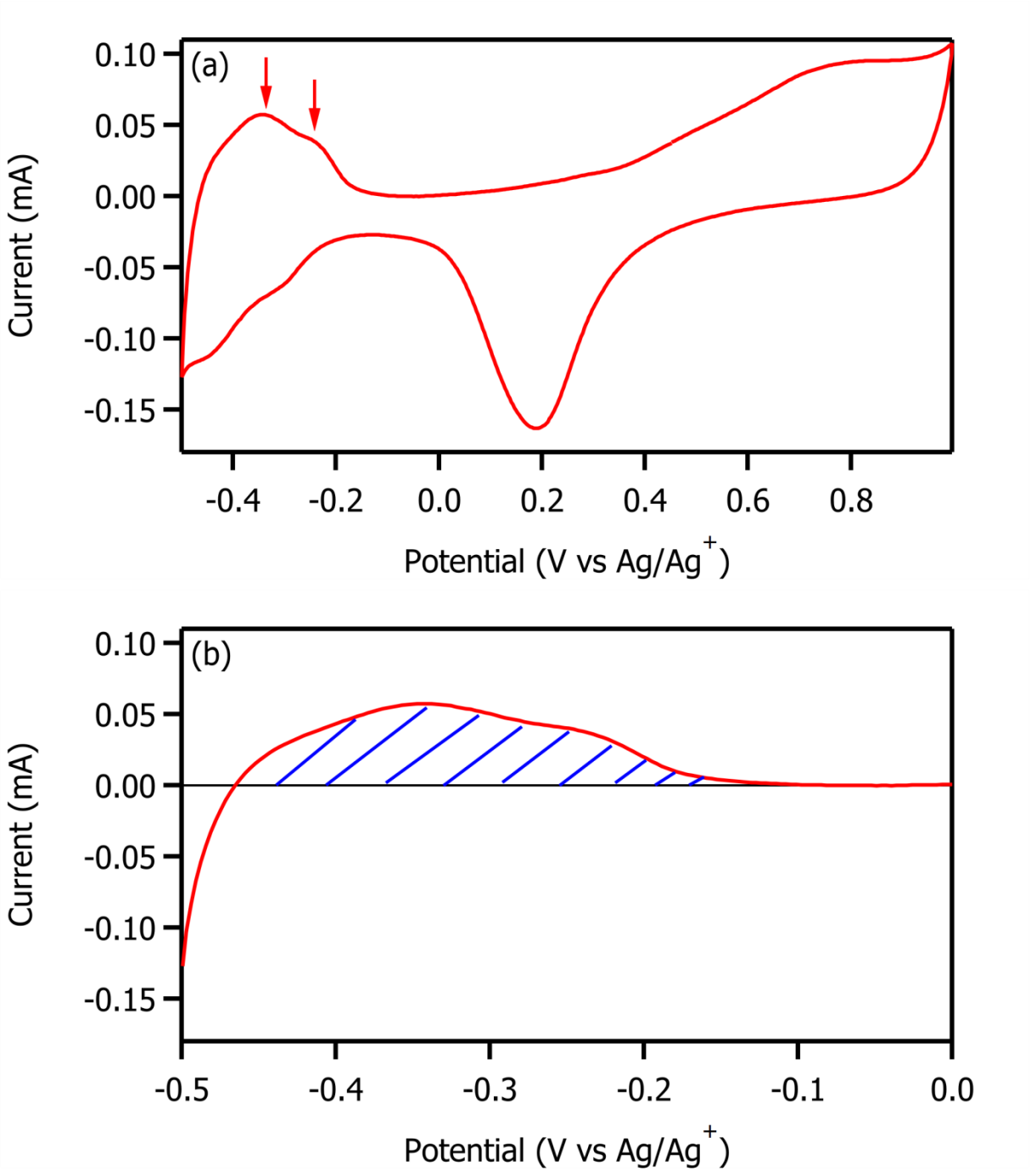

Fig. 3.6. (a) Cyclic voltammograms of 0.1 M sulfuric acid aqueous solution. (b) Cyclic voltammogram in the hydrogen desorption region.

3.3 In-situ reference method

3.3.1 Introduction of in-situ reference method

HD-VSFG spectroscopy is a unique tool for determining the orientation of interfacial molecules. For the calibration of phase and amplitude of SF light, the sample SF signal needs to be normalized by a reference SF signal. In equation (3.2), the completely canceling out of the electric-field term means that the optical propagation length is exactly same both in a sample measurement and a reference measurement. An air/quartz interface has been mainly used as a reference because it has positive real constant $\chi^{(2)}$ in vibrationally non-resonant region. However, in the measurement of electrolyte/electrode interface, the air/quartz interface cannot be used as a reference. In electrochemical condition such as shown in Fig.3.3, the incident and output lights need to pass through the optical window and electrolyte solution layer. Therefore, the optical propagation length in the electrolyte/electrode system is different from the air/quartz reference. Owing to a lack of phase standard which is measurable with exactly same condition in electrochemical system, the sign of $\chi^{(2)}$ was not discussed in the previous HD-VSFG work [59].

To overcome this serious problem, I have developed an in-situ reference method for applying HD-VSFG spectroscopy to electrolyte/electrode interfaces. In this referencing method, the electrode hybridized with reference material, a 100 nm thickness platinum thin film electrode deposited on a half of z-cut quartz substrate (10×10×3 mm), is used [69]. In this case, sample electrode and reference quartz are located under the common optical window and electrolyte solution layer. The sample and reference spectra can be measured simply by moving the cell horizontally using a motored stage. Therefore, the optical propagation lengths of incident lights are almost same for the sample and reference measurements.

3.3.2 Phase difference due to sample height difference

Strictly speaking, the optical propagation length differs only by the thickness of electrode. Hence, the phase of SF signal from sample and reference are different. In the present experimental configuration, the SF pulse and LO pulse have same frequency and are the co-linear propagation geometry. Therefore, there is no phase shift of the SF signal relative to LO after SF and LO pulses reach at sample interface. In this section, the phase difference as a function of sample height difference is discussed. The schematic is shown in Fig. 3.7.

Let us assume that the phase of ω_{vis}, ω_{IR}, and ω_{LO} are ϕ_{vis}, ϕ_{IR} and ϕ_{LO}, respectively. The phase of SF light is given by the following relation [73].

$$\phi_{\mathrm{SF}} = \phi_{\mathrm{vis}} + \phi_{\mathrm{IR}} \ . \tag{3.14}$$

Then, the phase difference $\Delta\phi$ between the SF light and LO is given by the following equation [73].

$$\Delta\phi = \phi_{\mathrm{SF}} - \phi_{\mathrm{LO}} = \phi_{\mathrm{vis}} + \phi_{\mathrm{IR}} - \phi_{\mathrm{LO}} \ . \tag{3.15}$$

When the sample height differs by *h*, the phase difference of ω_{i} caused by height difference is expressed as the follows [73].

$$\Delta\phi_{\mathrm{i}} = \phi_{\mathrm{i}} - 2\pi\frac{h\cos\theta_{\mathrm{i}}}{\lambda_{\mathrm{i}}} \ . \tag{3.16}$$

Where, λ_{i} is a wavelength of each light. Hence, the phase difference, $\Delta\phi'$ between SF and LO when sample height changes is obtained as the following [73].

$$\begin{aligned}\Delta\phi' &= \left(\phi_{\mathrm{vis}} - 2\pi\frac{h\cos\theta_{\mathrm{vis}}}{\lambda_{\mathrm{vis}}}\right) + \left(\phi_{\mathrm{IR}} - 2\pi\frac{h\cos\theta_{\mathrm{IR}}}{\lambda_{\mathrm{IR}}}\right) - \left(\phi_{\mathrm{LO}} - 2\pi\frac{h\cos\theta_{\mathrm{LO}}}{\lambda_{\mathrm{LO}}}\right) \\ &= \Delta\phi - 2\pi\left(\frac{\cos\theta_{\mathrm{vis}}}{\lambda_{\mathrm{vis}}} + \frac{\cos\theta_{\mathrm{IR}}}{\lambda_{\mathrm{IR}}} - \frac{\cos\theta_{\mathrm{LO}}}{\lambda_{\mathrm{LO}}}\right)h \ .\end{aligned} \tag{3.17}$$

The second term of equation (3.17) shows the phase difference due to height difference. In the present case, height difference is 100 nm. The phase difference is calculated using equation (3.17) and the following parameters shown in Table 3.1.

$$\begin{aligned}2\pi\left(\frac{\cos 29.9}{796} + \frac{\cos 26.6}{3333} - \frac{\cos 29.3}{647}\right)\times 100 &= 5.843\times 10^{-3}\ [\mathrm{rad}] \\ = 5.843\times 10^{-3}\ [\mathrm{rad}]\times\frac{180}{\pi}\left[\frac{^\circ}{\mathrm{rad}}\right] &= 0.3348\ [^\circ]\end{aligned} \tag{3.18}$$

The phase difference due to 100 nm height difference is ca. 0.3°. Therefore, the height difference does not cause a significant phase shift.

Table 3.1. Parameters for calculation of equation (3.13).

	SF	vis	IR
λ [nm]	647	796	3333
θ [°]	29.3	29.9	26.6

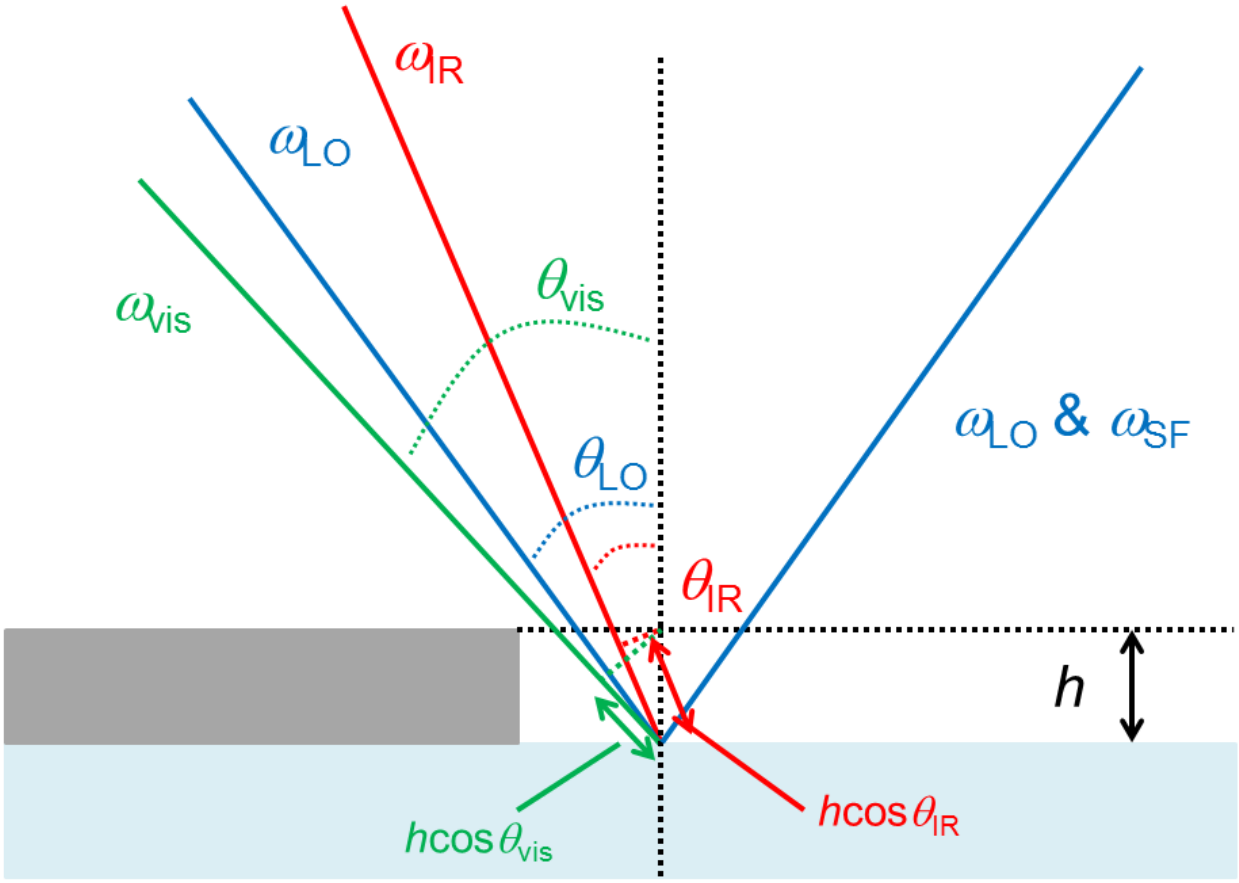

Fig. 3.7. Schematic of phase difference due to sample height difference.

3.3.3 The calculation of Fresnel factors

As shown in equation (2.134), there are four SFG active components in the PPP combination. In the present study, an acetonitrile/platinum interface is the target and a quartz substrate is used as a reference. Hence equation (3.4) can be expressed as the following formula [69].

$$\chi^{(2)}_{\mathrm{obs}} = \frac{r^{*\mathrm{Pt}}_{\mathrm{P,LO}}\chi^{(2)}_{\mathrm{Pt}}E_{\mathrm{vis}}E_{\mathrm{IR}}E^{*}_{\mathrm{LO}}e^{i\omega_{\mathrm{SF}}T}}{ir^{*\mathrm{Q}}_{\mathrm{P,LO}}\chi^{(2)}_{\mathrm{Q}}E_{\mathrm{vis}}E_{\mathrm{IR}}E^{*}_{\mathrm{LO}}e^{i\omega_{\mathrm{SF}}T}} = \frac{r^{*\mathrm{Pt}}_{\mathrm{P,LO}}\left[\sum F^{\mathrm{Pt}}_{\mathrm{IJK}}\chi^{(2)}_{\mathrm{IJK}}\right]}{r^{*\mathrm{Q}}_{\mathrm{P,LO}}(F^{\mathrm{Q}}_{XXX}\chi^{(2)\,\mathrm{Q}}_{XXX})} \ . \tag{3.19}$$

Where, Pt and Q denote platinum electrode and quartz reference, respectively. $r^{*}_{\mathrm{P,LO}}$ is a complex conjugated reflectivity of the LO beam in P-polarization, F_{IJK} (I, J, K=*X*, *Y*, *Z*) is a pre-factor including the Fresnel factors. I, J, K represent laboratory frame axis coordinates. *i* is an imaginary number unit and this factor appears because the reference quartz signal comes from bulk. The F_{IJK} is given by the following relation.

$$F_{\mathrm{IJK}} = F_{\mathrm{I}}(\omega_{\mathrm{SF}})F_{\mathrm{J}}(\omega_{\mathrm{vis}})F_{\mathrm{K}}(\omega_{\mathrm{IR}})L(\theta_{\mathrm{SF}},\theta_{\mathrm{vis}},\theta_{\mathrm{IR}}) \ . \tag{3.20}$$

Where, $L(\theta_{\mathrm{SF}},\theta_{\mathrm{vis}},\theta_{\mathrm{IR}})$ is a factor containing $\sin\theta$ or $\cos\theta$. From equation (2.133), the pre-factor is calculated as follows.

$$F_Z(\omega_{\mathrm{SF}}) = \frac{2n_2(\omega_{\mathrm{SF}})\cos\theta_{\mathrm{SF}}}{n_1(\omega_{\mathrm{SF}})\cos\gamma_{\mathrm{SF}} + n_2(\omega_{\mathrm{SF}})\cos\theta_{\mathrm{SF}}} \cdot \left(\frac{n_1(\omega_{\mathrm{SF}})}{n'(\omega_{\mathrm{SF}})}\right)$$
$$= 1.505 - 0.363i \ .$$
$$F_Z(\omega_{\mathrm{Vis}}) = \frac{2n_2(\omega_{\mathrm{vis}})\cos\theta_{\mathrm{vis}}}{n_1(\omega_{\mathrm{vis}})\cos\gamma_{\mathrm{vis}} + n_2(\omega_{\mathrm{vis}})\cos\theta_{\mathrm{vis}}} \cdot \left(\frac{n_1(\omega_{\mathrm{vis}})}{n'(\omega_{\mathrm{vis}})}\right)$$
$$= 1.552 - 0.324i \ .$$
$$F_Z(\omega_{\mathrm{IR}}) = \frac{2n_2(\omega_{\mathrm{IR}})\cos\theta_{\mathrm{IR}}}{n_1(\omega_{\mathrm{IR}})\cos\gamma_{\mathrm{IR}} + n_2(\omega_{\mathrm{IR}})\cos\theta_{\mathrm{IR}}} \cdot \left(\frac{n_1(\omega_{\mathrm{IR}})}{n'(\omega_{\mathrm{IR}})}\right)$$
$$= 1.752 - 0.218i \ .$$

$$F^{\mathrm{Pt}}_{ZZZ} = F_Z(\omega_{\mathrm{SF}})F_Z(\omega_{\mathrm{vis}})F_Z(\omega_{\mathrm{IR}})\sin\theta_{\mathrm{SF}}\sin\theta_{\mathrm{vis}}\sin\theta_{\mathrm{IR}}$$

$$= 0.399 + 0.254i \ .$$

(3.21)

As the same manner, other pre-factors are calculated and results are summarized in Table 3.2.

Table 3.2. Pre-factors at acetonitrile/platinum interfaces.

	F^{Pt}_{ZZZ}	F^{Pt}_{XXZ}	F^{Pt}_{XZX}	F^{Pt}_{ZXX}
Acetonitrile/platinum	0.399+0.254*i*	-0.003+0.114*i*	0.014+0.065*i*	-0.011-0.054*i*

Since F^{Pt}_{XZX} and F^{Pt}_{ZXX} are negligible small compared to F^{Pt}_{ZZZ} and F^{Pt}_{XXZ}, F^{Pt}_{XZX} and F^{Pt}_{ZXX} are ignored in the present analysis. Therefore, equation (3.19) is rewritten as the following equation [69].

$$\chi^{(2)}_{\mathrm{obs}} \approx \frac{r^{*\mathrm{Pt}}_{\mathrm{P,LO}} \left(F^{\mathrm{Pt}}_{ZZZ} \chi^{(2)}_{\mathrm{Pt},ZZZ} + F^{\mathrm{Pt}}_{XXZ} \chi^{(2)}_{\mathrm{Pt},XXZ} \right)}{r^{*\mathrm{Q}}_{\mathrm{P,LO}} F^{\mathrm{Q}}_{XXX} \chi^{(2)}_{\mathrm{Q},XXX}}$$

$$\propto (A_F \chi^{(2)}_{\mathrm{Pt},ZZZ} + \chi^{(2)}_{\mathrm{Pt},XXZ}) \ . \qquad (3.22)$$

Where, $A_F = F^{Pt}_{ZZZ}/F^{Pt}_{XXZ}$.

The $r^{*}_{\mathrm{P,LO}}$ is calculated by the following equation [69].

$$r^{*}_{\mathrm{P,LO}} = \left(\frac{n_2(\omega_{\mathrm{SF}}) \cos\theta_{\mathrm{SF}} - n_1(\omega_{\mathrm{SF}}) \cos\gamma_{\mathrm{SF}}}{n_2(\omega_{\mathrm{SF}}) \cos\theta_{\mathrm{SF}} + n_1(\omega_{\mathrm{SF}}) \cos\gamma_{\mathrm{SF}}} \right)^{*} \ .$$

(3.23)

The calculated $r^{*\mathrm{Pt}}_{\mathrm{P,LO}}$ and $r^{*}_{\mathrm{P,LO}} F^{\mathrm{Pt}}$ are summarized in Table 3.3.

Table 3.3. Complex conjugate of reflectivity of LO and factors of acetonitrile/platinum interfaces.

$r^{*\mathrm{Pt}}_{\mathrm{P,LO}}$	$r^{*\mathrm{Pt}}_{\mathrm{P,LO}} F^{\mathrm{Pt}}_{ZZZ}$	$r^{*\mathrm{Pt}}_{\mathrm{P,LO}} F^{\mathrm{Pt}}_{XXZ}$
0.633-0.394*i*	0.353+0.003*i*	0.043+0.073*i*

As shown in Table 3.3, the real part of $r^{*\mathrm{Pt}}_{\mathrm{P,LO}} F^{\mathrm{Pt}}_{ZZZ}$ is larger compared to the other part and the imaginary parts are very small. Hence, one can assume the imaginary part of spectra reflects the

Im$\chi^{(2)}$. The parameters used for calculation are listed in Table 3.4.

Table 3.4. Parameters for calculation of pre-factors

	SF	vis	IR
n_1	1.344 [74]	1.344 [74]	1.345 [75]
n_2	2.346+4.216*i* [76]	2.817+4.907*i* [76]	3.118+10.748*i* [76]
n’	1.40 [77]	1.40 [77]	1.40 [77]
θ [°]	29.3	29.9	26.6

The angle γ in equation (3.21) and (3.23) is calculated from Snell’s law, expressed by equation (3.24).

$$n_1(\omega_\mathrm{i})\sin\theta_\mathrm{i} = n_2(\omega_\mathrm{i})\sin\gamma_\mathrm{i} \ . \tag{3.24}$$

Also, the pre-factor $F^{\mathrm{Q}}{}_{XXX}$ and reflectivity $r^{*\mathrm{Q}}{}_{\mathrm{P,LO}}$ for the acetonitrile/quartz interface is calculated in the same manner as for acetonitrile/platinum interfaces. In *z*-cut quartz, the SFG active component is only $\chi^{(2)}{}_{XXX}$. The factor B is multiplied to $F^{\mathrm{Q}}{}_{XXX}$ for quartz interfaces [73]. Then, the relation is expressed by following equations.

$$F^{\mathrm{Q}}_{XXX} = BF_X(\omega_\mathrm{SF})F_X(\omega_\mathrm{vis})F_X(\omega_\mathrm{IR})\sin\theta_\mathrm{SF}\sin\theta_\mathrm{vis}\sin\theta_\mathrm{IR} \ . \tag{3.25}$$

$$B = \frac{c\sin\theta_\mathrm{p}}{\omega_\mathrm{SF}n_2(\omega_\mathrm{SF})(\sin\gamma_\mathrm{SF} + \sin\theta_\mathrm{p})} . \tag{3.26}$$

$$\theta_\mathrm{p} = \sin^{-1}\{n_\mathrm{p}^{-1}\omega_\mathrm{SF}^{-1}(\omega_\mathrm{vis}n_2(\omega_\mathrm{vis})\sin\gamma_\mathrm{vis} + \omega_\mathrm{IR}n_2(\omega_\mathrm{IR})\sin\gamma_\mathrm{IR})\} \ . \tag{3.27}$$

$$n_\mathrm{p} = \omega_\mathrm{SF}^{-1}\{(\omega_\mathrm{vis}n_2(\omega_\mathrm{vis})\sin\gamma_\mathrm{vis} + \omega_\mathrm{IR}n_2(\omega_\mathrm{IR})\sin\gamma_\mathrm{IR})^2 + (\omega_\mathrm{vis}n_2(\omega_\mathrm{vis})\cos\gamma_\mathrm{vis} + \omega_\mathrm{IR}n_2(\omega_\mathrm{IR})\cos\gamma_\mathrm{IR})^2\}^{1/2} .$$

(3.28)

The calculated pre-factor and reflectivity are shown in Table 3.5.

Table 3.5. Reflectivity and factors for quartz interfaces.

$r^{Q*}_{P,LO}$	F^{Q}_{XXX}	$r^{Q*}_{P,LO}F^{Q}_{XXX}$
0.050	3.156×10^{-9}	1.576×10^{-10}

The refractive indices used for calculation are shown in Table 3.6.

Table 3.6. The refractive indices of quartz for calculation.

	SF	vis	IR
n_2	1.54 [78]	1.54 [78]	1.50 [78]

3.3.4 Validation of the in-situ reference method

Before applying the in-situ reference method to a real electrochemical system, first, it was validated that the in-situ reference method works properly even under the liquid phase condition. In the present work, a self-assembled monolayer (SAM) of 1-octadecanethiol (ODT) on a platinum electrode is measured in both air and water and $\chi^{(2)}$ spectra of them are compared. The structure of ODT SAM on noble metal (Au, Ag, Pt) surfaces has been well studied by spectroscopic techniques such as IR spectroscopy [79, 80] and conventional VSFG spectroscopy [81, 82]. The terminal methyl group of the ODT SAM on the metal is expected to point away from the metal surface (i.e., CH_3-up orientation) because sulfur makes a strong chemical bond with noble metal. Using the fact that methyl group of the ODT SAM points away from the metal, I demonstrate that the up/down orientation of interfacial molecules can be determined from the sign of $\mathrm{Im}\chi^{(2)}$ even at liquid/solid interfaces as well as air/liquid interfaces.

The ODT SAM was prepared by immersing a platinum-deposited quartz substrate in 10 mM ODT ethanol solution for overnight. After that, the sample was rinsed with ethanol.

Fig. 3.7a shows the $\chi^{(2)}$ spectra of ODT SAM measured in air. The corresponding $|\chi^{(2)}|^2$ spectrum are obtained from the corresponding complex spectrum and the $|\chi^{(2)}|^2$ spectrum is very similar to the previous report done by conventional VSFG spectroscopy [81]. Im $\chi^{(2)}$ and Re $\chi^{(2)}$ show a positive and negative offset, respectively. This is attributed to the non-resonant background $\chi^{(2)}_{NR}$ due to an intra-band transition of free electrons of a platinum electrode. The detail of

non-resonant background is discussed in chapter 4. In general, $\chi^{(2)}_{NR}$ of a metal is not purely real. But that of a platinum is close to real [83, 84]. The Im $\chi^{(2)}$ spectrum of the ODT SAM in air shows negative peaks in the CH stretch region. These peaks are assignable as follows [85-87]. The peaks at 2874 cm^{-1} and 2935 cm^{-1} are assigned to the CH_3 symmetric stretch ($CH_{3,ss}$) of terminal methyl group of ODT which is split by Fermi resonance with a bending stretch overtone. Another peak at 2962 cm^{-1} is due to the CH_3 antisymmetric stretch ($CH_{3,as}$) of terminal methyl group of ODT. A shoulder peak at 2850 cm^{-1} and broad feature at 2920 cm^{-1} are coming from the CH_2 symmetric ($CH_{2,ss}$) and CH_2 antisymmetric ($CH_{2,as}$) stretch modes, respectively. According to previous reports, the peaks of $CH_{2,ss}$ and $CH_{2,as}$ in monolayer systems show weak intensity because the alkyl chain takes all-trans configuration [85-87]. Therefore, the contribution from CH_2 moieties is canceled out due to local inversion symmetry [85-87]. The observed CH_3 stretch bands and small CH_2 features indicate that the ODT SAM on platinum has all-trans alkyl chain structure with partial gauche defects [81, 82].

Fig. 3.7b shows the $\chi^{(2)}$ and $|\chi^{(2)}|^2$ spectra of ODT SAM measured in water. The vertical scale is different from that in air. This is because the Fresnel factors in water are larger than in air. The calculated Fresnel factors are summarized in Table 3.7 [69]. In the $\chi^{(2)}$ and $|\chi^{(2)}|^2$ spectra, peak features of CH_2 and CH_3 groups are observed although the relative amplitudes between the vibrational bands are slightly different from those observed in air. This result shows that ODT forms a monolayer and hence methyl-up structure is maintained even in water. The most important fact is that the Im $\chi^{(2)}$ spectrum shows a Lorentzian-like negative peak as is observed in air. This demonstrates that phase calibration using the in-situ reference method works properly even at buried interfaces such as liquid/metal interfaces. In addition, the phase of $\chi^{(2)}_{NR}$ in air and in water appear different to each other. This difference is due to the different surface condition of the sample in the different environments. However, a possible experimental phase error is not excluded.

Table 3.7. Calculated Fresnel factors for air/platinum and water/platinum [69].

	F_{ZZZ}	F_{XXZ}	$r^{*Pt}_{P,LO}$	$r^{*Pt}_{P,LO}F^{Pt}_{ZZZ}$	$r^{*Pt}_{P,LO}F^{Pt}_{XXZ}$
Air/Pt	0.179	-0.047	0.751	0.222	0.061
	+0.141i	-0.042i	-0.623i	-0.005i	-0.003i
Water/Pt	0.438	-0.152	0. 687	0.593	0.222
	+0.424i	-0.170i	-0.690i	-0.010i	+0.012i

The significant problem of the ODT SAM measurements is whether the obtained sign of peak in the Im $\chi^{(2)}$ spectrum corresponds to the methyl-up orientation. In order to answer this problem, the relation between the up/down orientation and the sign of peak in the Im $\chi^{(2)}$ spectrum is described below. Expressions for $\chi^{(2)}_{ZZZ}$ and $\chi^{(2)}_{XXZ}$ of the $CH_{3,ss}$ and $CH_{3,as}$ at the resonant frequencies have been reported as a function of orientation angle θ of the methyl group [87]. The formulas are expressed as follows.

$$\chi^{(2)}_{ZZZ,\mathrm{CH_{3,ss}}} = N_s\beta_{zzz,\mathrm{CH_{3,ss}}}\{R(\langle\cos\theta\rangle - \langle\cos^3\theta\rangle) + \langle\cos^3\theta\rangle\} \ . \tag{3.29}$$

$$\chi^{(2)}_{ZZZ,\mathrm{CH_{3,as}}} = 2N_s\beta_{xzx,\mathrm{CH_{3,as}}}(\langle\cos\theta\rangle - \langle\cos^3\theta\rangle) \ . \tag{3.30}$$

$$\chi^{(2)}_{XXZ,\mathrm{CH_{3,ss}}} = \frac{1}{2}N_s\beta_{zzz,\mathrm{CH_{3,ss}}}\{R(\langle\cos\theta\rangle + \langle\cos^3\theta\rangle) + (\langle\cos\theta\rangle - \langle\cos^3\theta\rangle)\} \ . \tag{3.31}$$

$$\chi^{(2)}_{XXZ,\mathrm{CH_{3,as}}} = -N_s\beta_{xzx,\mathrm{CH_{3,as}}}(\langle\cos\theta\rangle - \langle\cos^3\theta\rangle) \ . \tag{3.32}$$

where, *x* and *z* represent the molecular frame axis and *z* axis corresponds to the direction of the transition dipole moment of the $CH_{3,ss}$ vibration mode. In this definition, hyperpolarizability components, β_{xxz}, β_{yyz}, and β_{zzz} are non-zero for $CH_{3,ss}$ and only β_{xzx} is non-zero for $CH_{3,as}$ [87]. These hyperpolarizability components of the CH stretch modes are all negative [40, 88]. *R* is the ratio between β_{xxz}(β_{yyz}) and β_{zzz}; $R = \beta_{xxz}/\beta_{zzz}$ and it is positive. It has been reported that $R = 3.4$ for methyl group of 1-alchol with long alkyl chain [87]. It can be considered that the *R* value of methyl group of ODT is very similar to 3.4 because ODT has the almost same structure as long-alkyl-chain 1-alchol except for the thiol moiety. Therefore, $R = 3.4$ is used in the calculation.

From equation (3.22) and (3.29) - (3.32), the following relations are obtained.

$$\chi^{(2)}_{\mathrm{obs,CH_{3,ss}}} \approx \beta_{zzz,\mathrm{CH_{3,ss}}}\{(A_F R + \frac{1}{2})(\langle\cos\theta\rangle - \langle\cos^3\theta\rangle) + \frac{R}{2}\langle\cos\theta\rangle + (A_F + \frac{R}{2})\langle\cos^3\theta\rangle\} \ .$$

(3.33)

$$\chi^{(2)}_{\mathrm{obs,CH_{3,as}}} \approx \beta_{xzx,\mathrm{CH_{3,as}}}\{(2A_F - 1)(\langle\cos\theta\rangle - \langle\cos^3\theta\rangle)\} \ . \qquad (3.34)$$

Equation (3.33) and (3.34) imply that when <cosθ> is positive, $\chi^{(2)}_{\mathrm{obs,CH3,ss}}$ and $\chi^{(2)}_{\mathrm{obs,CH3,as}}$ are negative because the inside of {} in equation (3.33) and (3.34) are both positive while β_{xxz} and β_{zzz} are negative. As the same logic, when <cosθ> is negative, $\chi^{(2)}_{\mathrm{obs,CH3,ss}}$ and $\chi^{(2)}_{\mathrm{obs,CH3,as}}$ are positive. Therefore, the negative sign of the CH_3 bands shown in Fig.3.7 indicates that <cosθ> is positive, corresponding to the methyl-up orientation of ODT SAM. Moreover, equation (3.33) and (3.34) imply that the $CH_{3,ss}$ vibration band and $CH_{3,as}$ vibration band have the same sign of Im $\chi^{(2)}$. These consistencies between experimental observation and theory justify that the up/down orientation of interfacial molecules can be determined by the in-situ reference method.

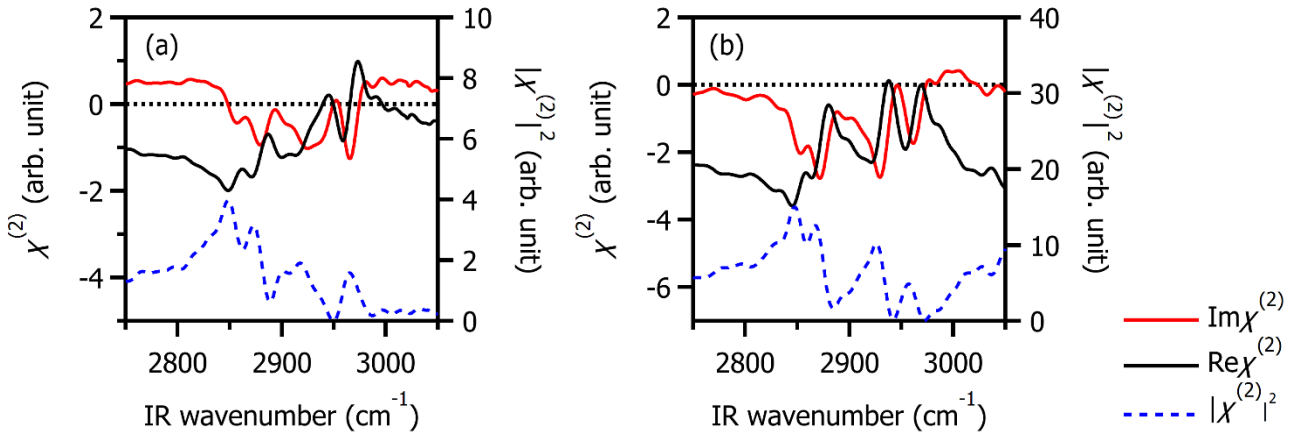

Fig. 3.8. $\chi^{(2)}$ and $|\chi^{(2)}|^2$ spectra of ODT SAM on the platinum electrode measured in (a) air and (b) water. Red and black solid curves represent Im $\chi^{(2)}$ and Re $\chi^{(2)}$, respectively. Blue broken curves are corresponding $|\chi^{(2)}|^2$ spectra calculated from $\chi^{(2)}$ spectra.

3.4 Conclusion of chapter 3

The in-situ reference method has been developed and it enables us to realize electrochemical HD-VSFG measurements with correct phase. Using ODT SAM on platinum as a model sample, it was demonstrated that the up/down orientation of the terminal methyl group of ODT SAM can be determined experimentally with employing the in-situ reference method. The largest advantage of the in-situ reference method is that the absorption by liquid phase is corrected by the normalization. Therefore, in-situ reference method can be used for studying the orientations of solvent molecules at electrolyte/electrode interfaces.

4. HD-VSFG measurement of acetonitrile/platinum interfaces

4.1 Introduction of studying electrolyte/electrode interfaces

Molecular-level information of structure and electrochemical reactions at electrolyte/electrode interfaces is essentially important not only for understanding of the fundamental electrochemical process but also for industrial applications such as development of next-generation rechargeable batteries [89-91]. For achieving this purpose, huge efforts have been made using various methods such IR [22-25], Raman [26-29] spectroscopy and X-ray scattering [13-15]. In spite of its importance and efforts, however, the structure and electrochemical reactions at the electrolyte/electrode interfaces have not been understood well at the molecular level owing to the complexity of the electrochemical interfaces. Hence, further development of advanced in-situ characterization techniques is desired for obtaining molecular-level knowledge about the electrolyte/electrode interfaces.

As mentioned in chapter 1, electrochemical interfaces are the core of electrochemistry, and they have been one of the most important targets of VSFG spectroscopy for many years [48-58]. But most of previous electrochemical VSFG works were carried out by conventional homodyne-detected VSFG spectroscopy because it is difficult to determine the phase and amplitude of the SF signal at the electrolyte/electrode interface. In other words, it is difficult to measure a reference spectrum for calibration of the phase of SF signal under the same condition as the sample measurement due to the presence of the electrolyte solution and the optical window. Previously, Zanni and co-workers applied HD-VSFG spectroscopy to a CO-adsorbed electrode interface [59], however, they did not discuss the sign of $\chi^{(2)}$ at the electrolyte/electrode interface because of the lack of the phase reference. To overcome this serious problem, I developed the in-situ reference method described in the chapter 3. The in-situ reference method has enabled us to determine the phase and amplitude of the $\chi^{(2)}$ spectrum at electrolyte/electrode interfaces [69].

In this study, by using this in-situ reference method, HD-VSFG spectroscopy is applied to a prototypical non-aqueous electrochemical interface, i.e., the interface between a platinum electrode and 0.1 M $LiCF_3SO_3$ acetonitrile (CH_3CN) solution. Surprisingly, the HD-VSFG experiments clearly indicate that the CH_3 group of acetonitrile points toward the platinum electrode at positive electrode potentials, which is counter-intuitive and is opposite to the orientation that has been proposed by a previous VSFG study [49]. Supported by additional data obtained with conventional VSFG experiments, it is concluded that this orientation of acetonitrile is induced by the anion adsorbed on the electrode surface at the positive potentials. This is the first experimental observation of the potential-dependent up/down orientation of molecules at the electrolyte/electrode interface, which is

essential for obtaining the molecular-level picture at the electrochemical interfaces.

4.2 Cyclic voltammetry

Two cycles of cyclic voltammetry were carried out between -0.8 V and 2.0 V at a scan rate of 10 mV/s before the spectroscopic measurements. Fig. 4.1 shows the cyclic voltammogram of 0.1 M $LiCF_3SO_3$ acetonitrile solution. The current density (i.e., the vertical axis) in Fig. 4.1 was determined using the surface area of the platinum electrode shown in section 3.2.3. The very low current density indicates that no electrochemical reaction occurs in this potential region, and only an electric double layer is charged. The slight tilt of the voltammogram suggests that the resistance of the thin-solution layer is high in the present electrochemical cell. To minimize the effect, I waited 6 minutes after changing the electrode potential prior to the spectroscopic measurement to allow the system to reach the equilibrium.

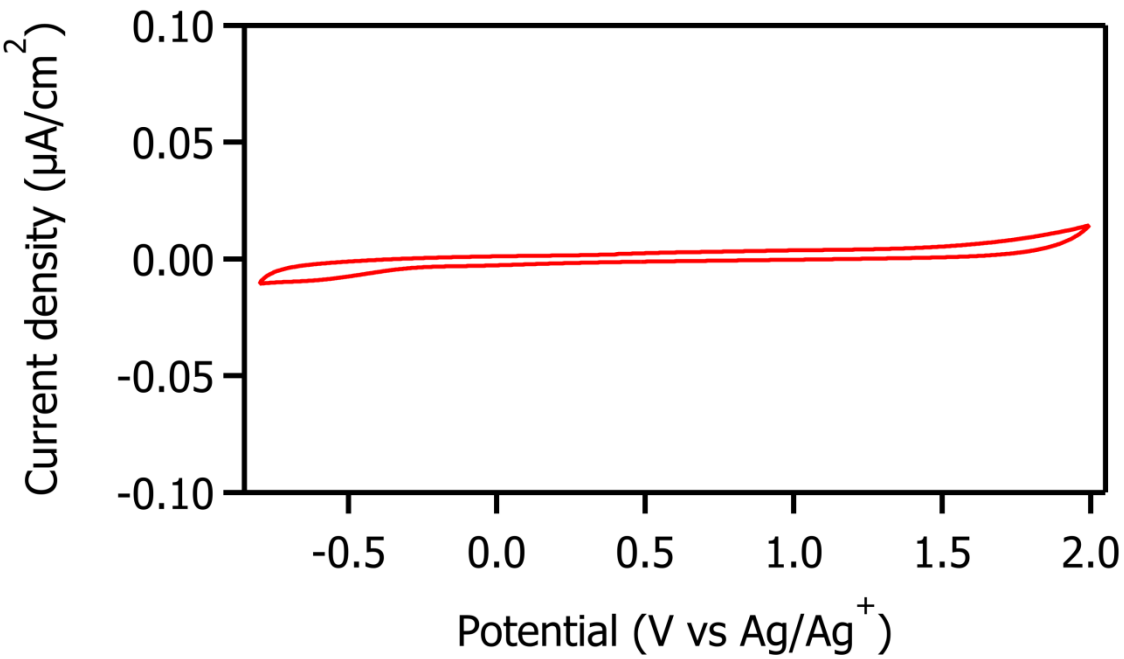

Fig. 4.1. Cyclic voltammogram of 0.1 M $LiCF_3SO_3$ acetonitrile solution. The scan rate was 10 mV/s.

4.3 Estimation of the thickness of electric double layer

At the charged interfaces, molecules not only at the topmost layer but also in the diffuse electric double layer (EDL) can be oriented by the electric field and may contribute to the $\chi^{(2)}$ spectra. This contribution of the oriented molecules in the EDL is often called the $\chi^{(3)}$ effect. In order to show that the $\chi^{(3)}$ effect is negligible in the spectra shown in this study, the thickness of diffuse EDL was estimated as follows.

The potential profile is obtained as a function of distance from the interface (x) by solving Poisson equation and the result is given by the following equation [92]:

$$\phi = \frac{2k_{\mathrm{B}}T}{ze}\ln\{\frac{1+g\exp(-\kappa x)}{1-g\exp(-\kappa x)}\}\ ,$$

$$g = \frac{\exp\left(\frac{ze\phi_0}{2k_{\mathrm{B}}T}\right)-1}{\exp\left(\frac{ze\phi_0}{2k_{\mathrm{B}}T}\right)+1}\ ,$$

$$\kappa = (\frac{2e^2N_{\mathrm{A}}cz^2}{\varepsilon_{\mathrm{r}}\varepsilon_0k_{\mathrm{B}}T})^{1/2}\ ,$$

(4.1)

where, ε_{r}, ε_0, k_{B}, T, e, c, z, and ϕ_0 are the relative dielectric constant, vacuum dielectric constant (= 8.854×10^{-12} C^2 J^{-1} m^{-1}), Boltzmann constant (=1.381×10^{-23} J K^{-1}), temperature (300 K), elementary charge (=1.602×10^{-19} C), concentration of electrolyte (in mol m^{-3}), valence of ion and potential applied to the electrode (potential at x=0), respectively. Using the relative dielectric constant of acetonitrile (38.8 [93]), κ is calculated as follows:

$$\kappa = (\frac{2\times(1.602\times10^{-19})^2\times6.022\times10^{23}\times0.1\times1000\times1^2}{38.8\times8.854\times10^{-12}\times1.381\times10^{-23}\times300})^{1/2}$$
$$= 1.474\times10^{9}\ [\mathrm{m^{-1}}]\ .$$

(4.2)

The potential profile for ϕ_0 = 0.2 V, 0.6 V and 2.0 V are calculated and shown in Fig. 4.2. As seen in Fig. 4.2, the potentials drop precipitously at the very vicinity of the electrode (x<< 1 nm), in

particular when a large potential is applied. This means that the strong electric field exists only at the very vicinity of the electrode and that the electric field in the diffuse EDL (Gouy-Chapman layer) is small in the present electrochemical condition. Thus, it is considered that the contribution of the molecules in the diffuse EDL in the $\chi^{(2)}$ spectra (the $\chi^{(3)}$ effect) is negligible, and the observed vibrational bands are attributable to the molecules at the very vicinity of the electrode interface.

Moreover, in principle, it is possible that the CaF_2 window/electrolyte solution interface in the spectro-electrochemical cell contributes to the SFG signal. However, because the electrode potential is applied only at the electrolyte/electrode interface, any signals that are dependent on the applied potential are safely attributable to the electrode interface. In the present study, as shown in the later sections, all the observed vibrational bands vary depending on the potential and completely disappear at certain potentials. This potential dependence assures that these bands originate from the electrolyte/electrode interface, not from the CaF_2/electrolyte interface.

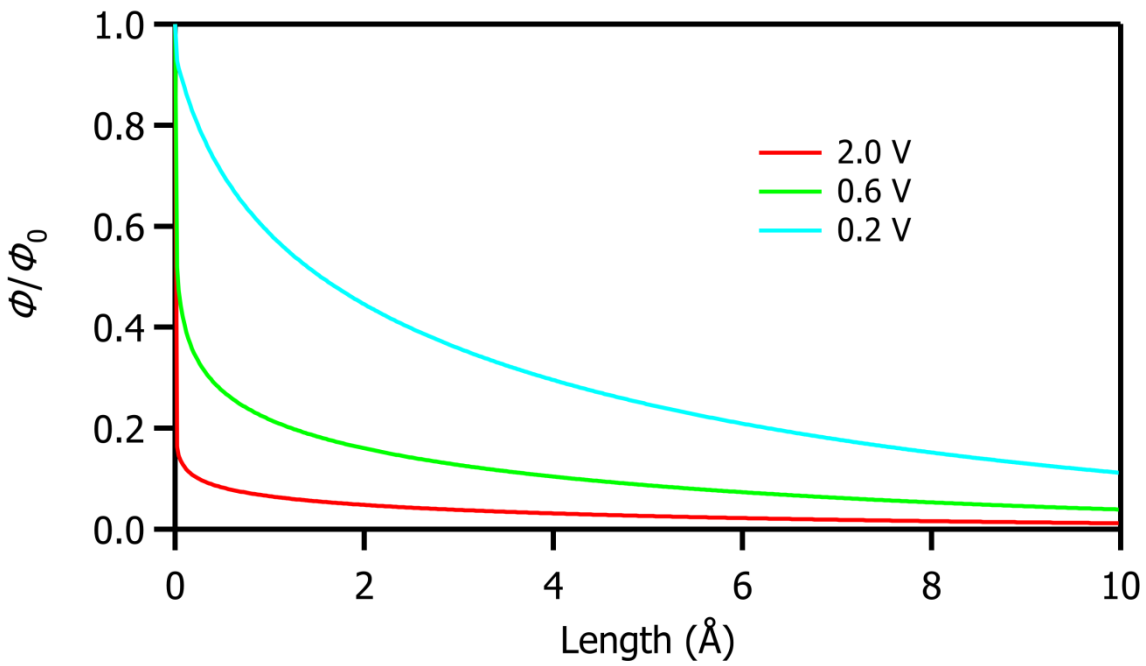

Fig. 4.2. Potential profile for the 0.1 M acetonitrile solution with various applied potentials.

4.4 HD-VSFG spectra in the CH stretch region

Fig. 4.3 shows the $\chi^{(2)}$ spectra of the acetonitrile/platinum interface in the CH stretch region with 0.1 M $LiCF_3SO_3$ electrolyte, which were measured with scanning the electrode potential between -0.8 V and 2.0 V with a 0.4 V potential increment. At 0.4 V which is close to the open circuit potential, the $\mathrm{Im}\chi^{(2)}$ spectrum shows a small positive (upward) peak at 2940 cm^{-1}. The amplitude of this peak increases as the electrode potential becomes more positive. On the other hand, it decreases as the electrode potential becomes more negative and finally disappears almost completely at -0.8 V. The frequency of this peak is close to the absorption maxima of the pure acetonitrile in the bulk (2944 cm^{-1}) [94]. Because it is known that the CH stretch band exhibits a red-shift when it strongly interacts with the electrode [95], the positive peak at 2940 cm^{-1} is assignable to CH_3 symmetric stretch mode of the acetonitrile molecules that are not directly attached to the electrode.

For free acetonitrile, the hyper polarizability of the CH_3 symmetric stretch is known to be negative [96]. Thus, the positive CH_3 symmetric band in the $\mathrm{Im}\chi^{(2)}$ spectra indicates CH_3-down orientation, i.e., the CH_3 group of acetonitrile is pointing toward the platinum electrode. This result differs from the argument of a previous homodyne VSFG study by Baldelli and co-workers [49]. In their work, the orientation of acetonitrile was assumed to be CH_3-up, considering the electrostatic interaction between the lone-pair electron on nitrogen and the positively charged electrode [49]. However, HD-VSFG spectroscopy realized in the present study experimentally determined the sign of the $\mathrm{Im}\chi^{(2)}$ signal and revealed that this is not the case. In order to confirm this conclusion, the $\mathrm{Im}\chi^{(2)}$ spectrum of acetonitrile is measured at the air/pure acetonitrile interface. Fig. 4.4 shows the $\chi^{(2)}$ and $|\chi^{(2)}|^2$ spectra of the air/acetonitrile interface in the CH stretch and CN stretch region. At the air/pure acetonitrile interface, acetonitrile is expected to have CH_3-up orientation because the CH_3 group is more hydrophobic compared to the CN group [96]. The sign of the CH_3 band in the $\mathrm{Im}\chi^{(2)}$ spectrum is indeed negative, which confirms that the negative CH_3 band corresponds to the CH_3-up orientation at the air/pure acetonitrile interface. Therefore, the positive CH_3 band observed at the acetonitrile/platinum interface surely shows that acetonitrile at the interface is in CH_3-down orientation. The reason why acetonitrile prefers the counter-intuitive CH_3 down orientation at the electrode interface is discussed in the later section. If the up/down orientation of acetonitrile changes with the electrode potential, the sign change of the CH_3 symmetric stretch peak is expected. However, no clear negative bands observed in the potential region examined in this study.

Fig. 4.3 also shows the $|\chi^{(2)}|^2$ spectra (blue broken curves) which were calculated from the $\chi^{(2)}$ spectra obtained with HD-VSFG measurements. These $|\chi^{(2)}|^2$ spectra show a peak at around 2950

cm^{-1}, and the peak intensity increases as the potential becomes more positive. On the other hand, at the potentials ranging from 0.8 V to -0.4 V, a small dip appears at around 2930 cm^{-1}. These spectral features of the $|\chi^{(2)}|^2$ spectra are qualitatively consistent with the spectra reported in a previous homodyne VSFG work [49]. In the previous work, the strong peak observed at 2940 cm^{-1} in the positive potential region was assigned to the CH_3 symmetric stretch of acetonitrile which is pointing away from the electrode (CH_3-up) whereas the red-shifted dip feature was assigned to the CH_3 symmetric stretch of acetonitrile that directly interacts with the electrode with CH_3-down orientation [49]. However, the $\mathrm{Im}\chi^{(2)}$ spectra obtained in this study show no negative peak at 2930 cm^{-1}, and hence it is now clear that the dip feature in the $|\chi^{(2)}|^2$ spectra is indeed an artifact that appears when the $\mathrm{Re}\chi^{(2)}$ approaches closely to zero. This demonstrates that HD-VSFG spectroscopy is critically important also for the study of electrochemical interfaces.

It is noteworthy that the vibrationally non-resonant background, $\chi^{(2)}_{NR}$ appears both in the $\mathrm{Im}\chi^{(2)}$ and $\mathrm{Re}\chi^{(2)}$ spectra, and $\chi^{(2)}_{NR}$ in the $\mathrm{Im}\chi^{(2)}$ spectra substantially changes with the change of the electrode potential. In Fig. 4.5a the amplitude of $\chi^{(2)}_{NR}$ is plotted as a function of the electrode potential. It is clear that $\chi^{(2)}_{NR}$ in the $\mathrm{Im}\chi^{(2)}$ spectrum does not show any noticeable change in the negative potential region but it goes to positive in the positive potential region. On the other hand, $\chi^{(2)}_{NR}$ in the $\mathrm{Re}\chi^{(2)}$ spectrum does not significantly vary with the electrode potential. Although the value of $\chi^{(2)}_{NR}$ differs depending on the sample, this trend of the potential dependence of $\chi^{(2)}_{NR}$ was well reproducible.

The origin of $\chi^{(2)}_{NR}$ in the $\mathrm{Im}\chi^{(2)}$ spectra at the electrode interface is not clear at the moment. However, in general, $\chi^{(2)}_{NR}$ in the $\mathrm{Im}\chi^{(2)}$ spectrum is attribute to either electronic resonance [32] or bulk contribution [97, 98]. Although the latter has been considered the origin of $\chi^{(2)}_{NR}$ in the $\mathrm{Im}\chi^{(2)}$ spectrum at dielectric interfaces [97, 98], it is not likely for the metal electrode because the charge of the metal electrode is localized only at the metal surface and thus it is difficult to imagine that the property of bulk metal changes with the potential. As for the former possibility, it is known that platinum has no inter-band transition in the visible frequency region [84]. Therefore, it is considered that the $\chi^{(2)}_{NR}$ in $\mathrm{Im}\chi^{(2)}$ spectra is likely attributable to the intra-band transition induced by the IR photon. The density of states of the neutral platinum is known to be large below Fermi level while it is small above Fermi level [99]. Hence it is possible that when the positive potential is applied, i.e., the Fermi level is lowered, abundant unoccupied states become available to absorb IR photons, which increases $\chi^{(2)}_{NR}$ in $\mathrm{Im}\chi^{(2)}$. On the other hand, if the negative potential is applied, i.e., the Fermi level becomes higher, the density of unoccupied states does not increase the intra-band transition. This expected behavior is consistent with the observed asymmetric potential dependence.

An important fact is that the phase of $\chi^{(2)}_{NR}$ of the platinum electrode varies with the potential. Indeed, the phase of $\chi^{(2)}_{NR}$ changes by as large as 60°, as clearly seen in Fig. 4.5b. As far as I know, this is the first explicit observation of the phase shift of $\chi^{(2)}_{NR}$ at the electrode interface during the potential scan. Such a potential-dependent phase shift of $\chi^{(2)}_{NR}$ makes the fitting analysis of conventional homodyne VSFG spectra even more difficult, and therefore the direct measurement of complex $\chi^{(2)}$ with HD-VSFG is important also in this respect.

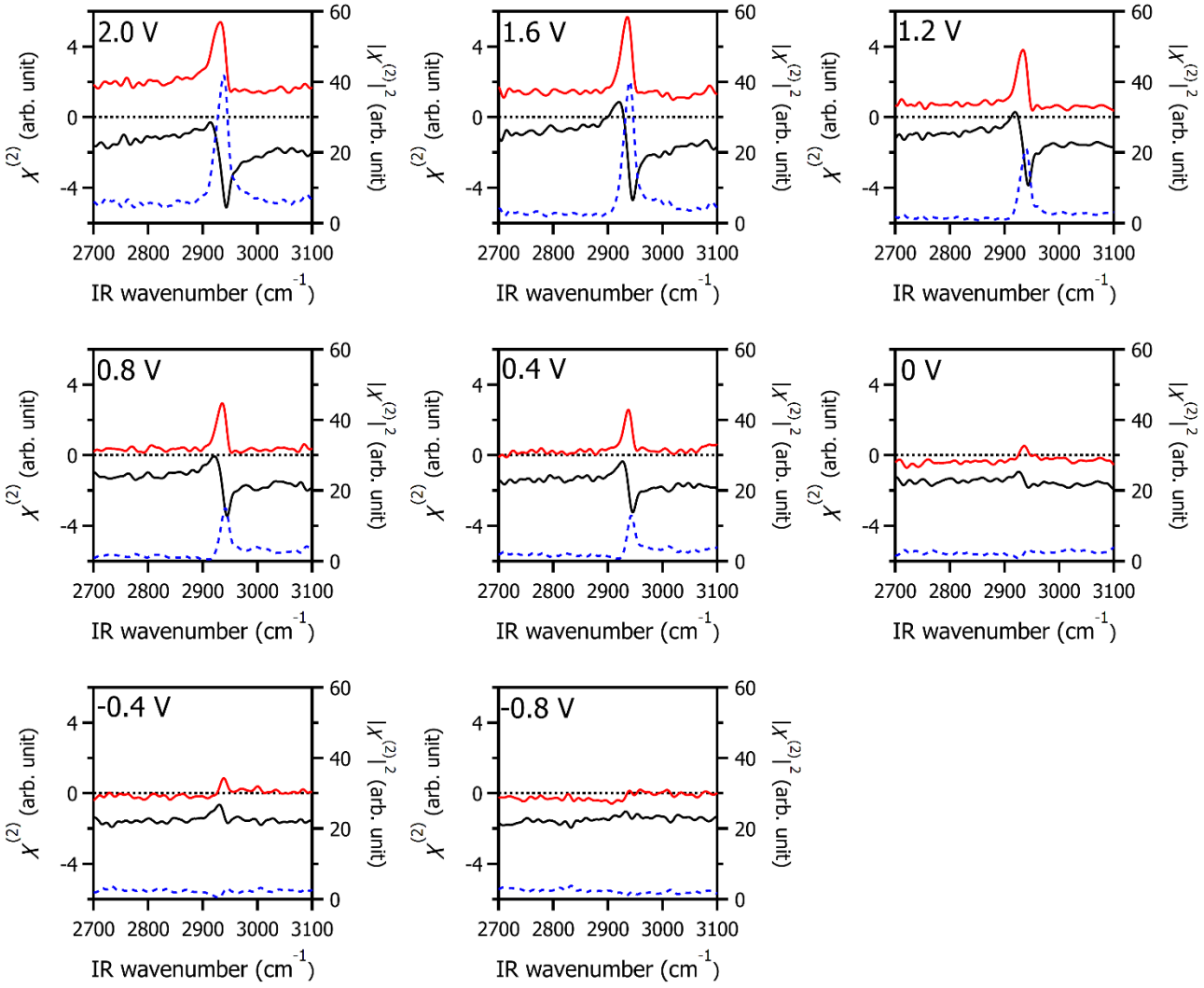

Fig. 4.3. The $\mathrm{Im}\chi^{(2)}$, $\mathrm{Re}\chi^{(2)}$ and $|\chi^{(2)}|$ spectra of the acetonitrile/platinum interface with 0.1 M $LiCF_3SO_3$ electrolyte in the CH stretch region. Red curve, black curve and blue broken curve are $\mathrm{Im}\chi^{(2)}$, $\mathrm{Re}\chi^{(2)}$ and $|\chi^{(2)}|$, respectively. The electrode potential with respect to Ag/Ag^+ is shown on top of each spectrum. The $|\chi^{(2)}|$ spectra were calculated from the and spectra.

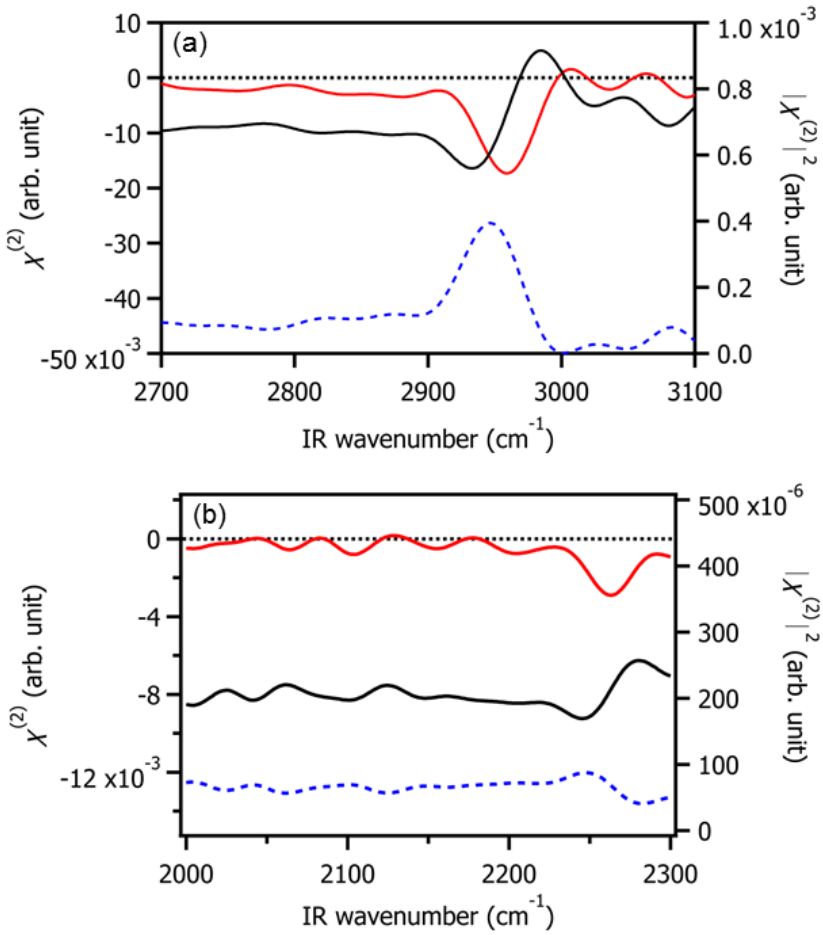

Fig. 4.4. $\chi^{(2)}$ and $|\chi^{(2)}|^2$ spectra of the air/acetonitrile interface in the (a) CH stretch and (b) CN stretch regions. The red and black solid curves represent Im $\chi^{(2)}$ and Re $\chi^{(2)}$ spectra, respectively. The blue broken curves represent $|\chi^{(2)}|^2$ spectra which were calculated from the Im $\chi^{(2)}$ and Re $\chi^{(2)}$ spectra. At this interface, the acetonitrile is expected to be in the CH_3-up (i.e., the CH_3 group points toward the air side [100]) and hence CN-down orientation.

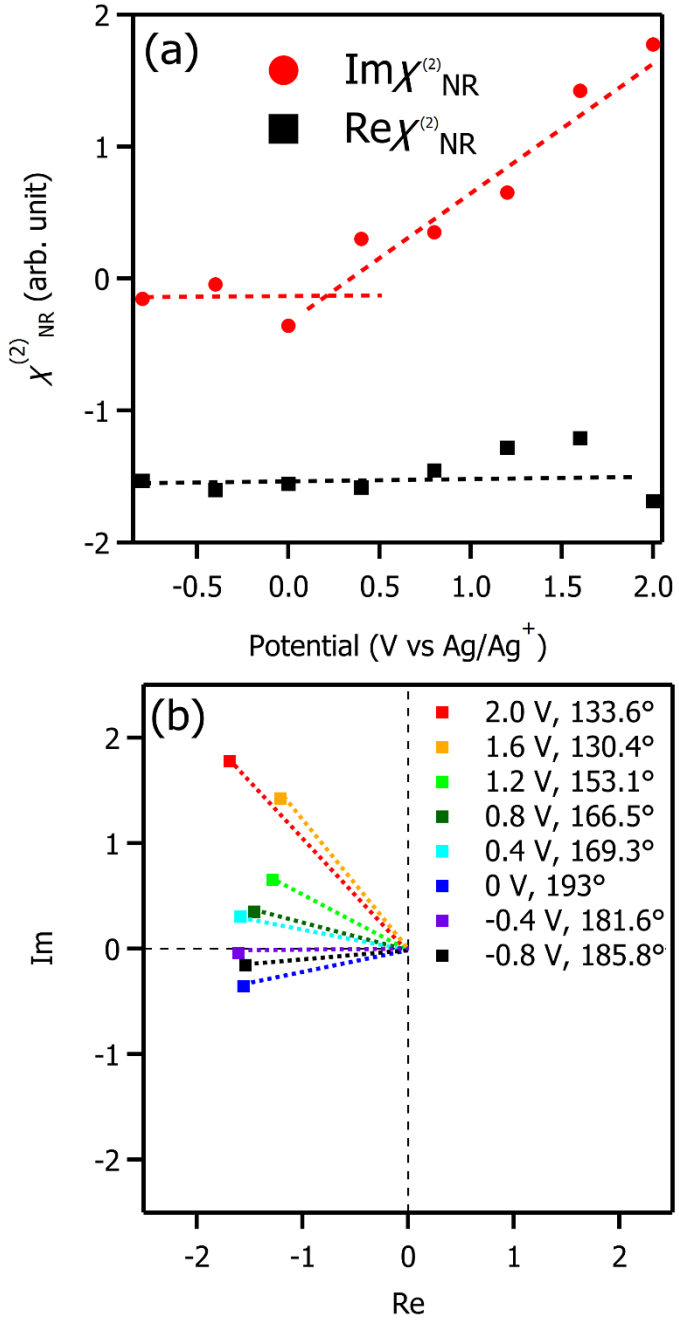

Fig. 4.5. Electrode potential dependence of $\chi^{(2)}_{NR}$. (a) Amplitude of $\chi^{(2)}_{NR}$. The broken lines are eye-guide. (b) Phase of $\chi^{(2)}_{NR}$. The phase angle at each potential is written in the legend.

4.5 HD-VSFG spectra in the CN stretch region

Fig.4.6 shows $\chi^{(2)}$ and $|\chi^{(2)}|^2$ spectra in the CN stretch region of the acetonitrile/platinum interface with 0.1 M $LiCF_3SO_3$ electrolyte. Because strong IR absorption of atmospheric CO_2 disturbs the spectra in the frequency region of 2300 – 2400 cm^{-1}, the spectra in the 2000 – 2300 cm^{-1} region are shown. At the positive potentials, the $Im\chi^{(2)}$ spectra exhibit two positive bands at 2245 and 2290 cm^{-1}, which are assignable to the CN stretch vibration of free acetonitrile and its Fermi resonance with a combination band, respectively [49, 94]. The amplitudes of these positive bands decrease as the electrode potential becomes more negative. The corresponding change can also be seen in the $|\chi^{(2)}|^2$ spectra. In fact, this change of the $|\chi^{(2)}|^2$ spectra has been reported in the previous homodyne VSFG work [49]. At the air/acetonitrile interface, the CN stretch band of acetonitrile appears with the negative sign (Fig. 4.4b). Because the acetonitrile molecule is expected to have the CN-down orientation at the air/acetonitrile interface, the opposite positive sign of the CN stretch band of acetonitrile at the acetonitrile/platinum interface indicates the CN-up orientation of acetonitrile molecules. This conclusion is consistent with the $Im\chi^{(2)}$ spectra in the CH_3 stretch region which indicates the CH_3-down orientation. In addition to the sharp vibrational resonance features due to the CN stretch (split by the Fermi resonance), a positive offset-like signal is observed in the $Im\chi^{(2)}$ spectra at the positive potentials, which is again consistent with the observation in the CH_3 stretch region. Consequently, the $Im\chi^{(2)}$ spectra in the CN region at the positive potentials accord well with those in the CH_3 stretch region (Fig. 4.3) which were discussed in the previous section.

In the potential region more negative than 0.8 V, a very broad negative band appears at around 2150 cm^{-1}. Such a broad band in the low frequency region has been observed in several different spectroscopic measurements, including subtractively normalized interfacial IR spectroscopy [20] and surface enhanced Raman spectroscopy [29]. Initially, this band was assigned to the CN stretch of acetonitrile that is directly adsorbed on the platinum surface [20, 101], however, later many groups re-assigned this band to the stretch vibration of the adsorbed CN^- on the platinum surface, which is produced by the catalytic decomposition at the platinum surface [29, 102, 103]. In homodyne VSFG studies, the broad 2150 cm^{-1} band has also been observed when the system contains CN^- ions in solution [102] or a hot platinum electrode was immersed in an acetonitrile solution [103]. Therefore, we assign this band to the adsorbed CN^-. We note that no CH band is observed in the negative potential region where this 2150 cm^{-1} band is observed (e.g., -0.8 V). This implies that the relevant chemical species has a CN moiety but not a CH group, being consistent with this assignment.

It is noteworthy that the 2150 cm^{-1} band was not observed in the previous VSFG study of acetonitrile/platinum interface by Baldelli et al. [49]. Gu et al. proposed that CN^- is produced at a

roughed platinum electrode at negative potentials but not at a smooth Pt(111) surface [29, 104]. Because Baldelli et al. used a single crystal whereas the evaporated thin platinum film was used in this study, the lack of the 2150 cm^{-1} band in the spectra reported by Baldelli et al. is highly likely attributable to the difference in the roughness of the platinum electrode used in the experiment.

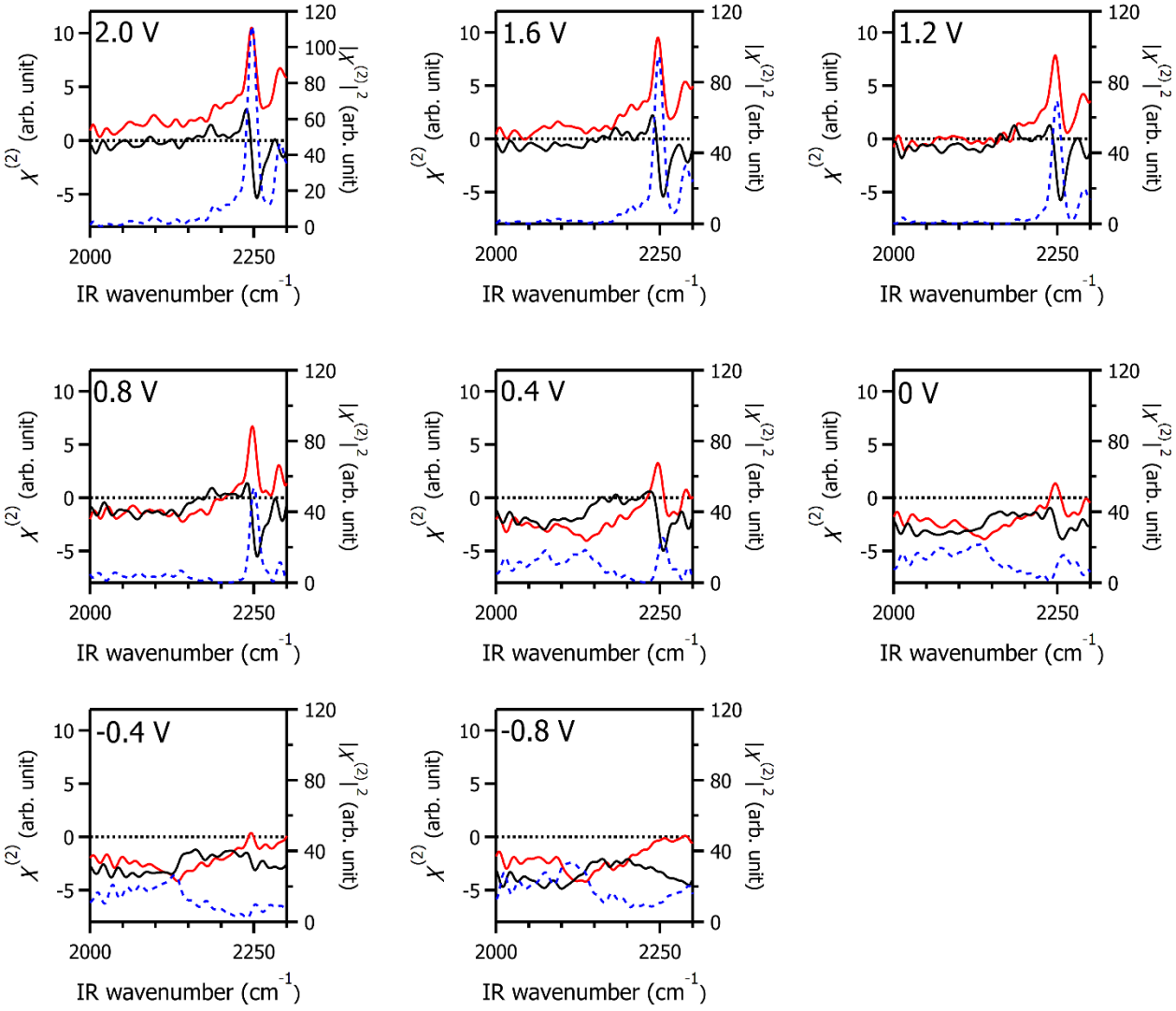

Fig. 4.6. The Im$\chi^{(2)}$, Re$\chi^{(2)}$ and $|\chi^{(2)}|$ spectra of the acetonitrile/platinum interface with 0.1 M $LiCF_3SO_3$ electrolyte in the CN stretch region. Red curve, black curve and blue broken curve are Im$\chi^{(2)}$, Re$\chi^{(2)}$ and $|\chi^{(2)}|$, respectively. The electrode potential with respect to Ag/Ag^+ is shown on top of each spectrum. The $|\chi^{(2)}|$ spectra were calculated from the and spectra.

4.6 HD-VSFG spectra without electrolyte

Intuitively, it is considered that acetonitrile prefers the CH_3-up & CN-down orientation at the acetonitrile/platinum electrode at positive potentials due to attractive electrostatic interaction between the lone-pair electron on nitrogen and the positively charged electrode [49]. However, the present HD-VSFG experiments clearly indicate that acetonitrile has the opposite orientation at the interface at the positive potentials, i.e., the CH_3-down and CN-up. In order to explain this counter-intuitive orientation of acetonitrile at the positive potentials, the possibility is considered that the anion is adsorbed on the platinum electrode and that this anion interacts with acetonitrile at the vicinity of the interface. In other words, I hypothesize that CH_3-down and CN-up orientation of acetonitrile is induced by the repulsive interaction between the lone-pair electron on nitrogen and negative charge of anions.

To verify the hypothesis mentioned above, $\mathrm{Im}\chi^{(2)}$ spectra of a pure acetonitrile/platinum interface was measured without the electrolyte to investigate the influence of anion to the orientation of acetonitrile. Fig. 4.7a shows the $\mathrm{Im}\chi^{(2)}$ spectrum in the CN stretch region at the pure acetonitrile/platinum interface in the open circuit condition. While a broad negative band (because of the adsorbed CN^-) is observed at 2200 cm^{-1}, any positive band assignable to the acetonitrile is hardly observed at 2245 cm^{-1}. This observation is consistent with the $\mathrm{Im}\chi^{(2)}$ spectrum in the CH stretch region shown in Fig. 4.7b, which does not show any clear peak at 2940 cm^{-1} owing to the CH_3 stretch of acetonitrile. These results indicate that free acetonitrile at the pure acetonitrile/platinum interface without ions is not preferentially oriented either CH_3-up or CH_3-down, suggesting an essential role of the anion to induce CH_3-down orientation of acetonitrile observed with electrolyte.

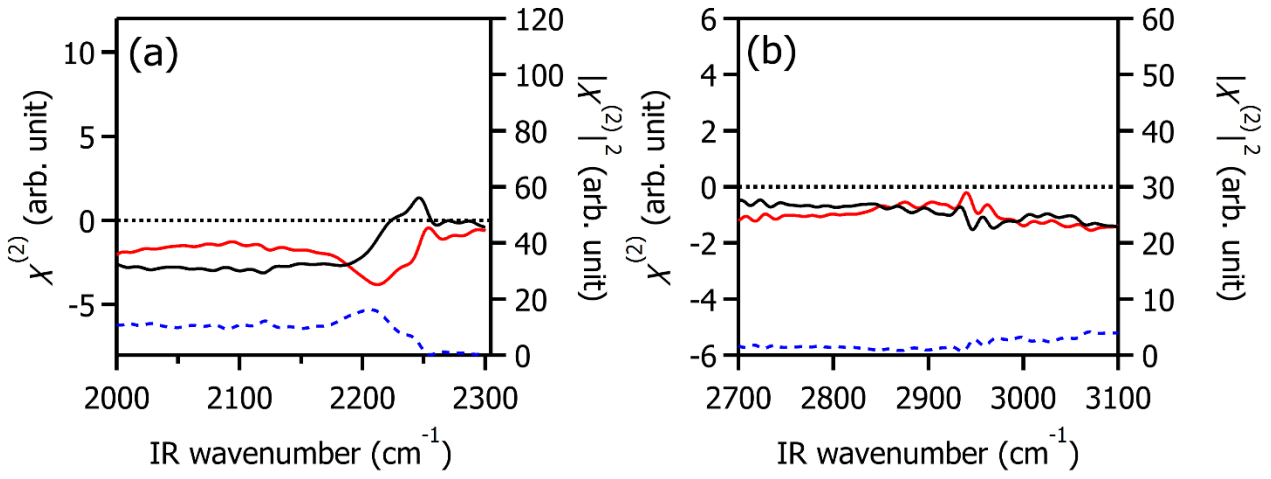

Fig. 4.7. The $\chi^{(2)}$ spectrum of pure acetonitrile/platinum interface in (a) the CN stretch region and (b) the CH stretch region. Red solid, black solid, and blue broken curves correspond to Im$\chi^{(2)}$, Re$\chi^{(2)}$, and $|\chi^{(2)}|^2$, respectively. The $|\chi^{(2)}|^2$ spectra were calculated from the Im$\chi^{(2)}$and Re$\chi^{(2)}$ spectra. The electrode potential is not under control without the electrolyte.

4.7 VSFG spectra of $CF_3SO_3^-$ anion

In order to directly prove the presence of the anion on the electrode and clarify its potential-dependent adsorption, VSFG spectra in 950 – 1200 cm^{-1} region was measured where the CF_3 and SO_3^- vibration of $CF_3SO_3^-$ anion appears. The experiments were done by conventional homodyne VSFG, not by HD-VSFG, because quartz cannot be used as the reference in this low frequency region due to the vibrational resonances of quartz itself. Nevertheless, the VSFG spectra obtained with homodyne detection are normalized by an air/gold spectrum to correct the effect of the intensity distribution of the ω_{IR} spectra. Although this normalization does not take account of the absorption of the $CF_3SO_3^-$ anion, the effect is not large in the present experiment, as shown in Fig. 4.8. These spectra show two strong vibrational resonances at 1070 cm^{-1} and 1170 cm^{-1} coming from the vibrational resonance of quartz itself, which prevents us to use quartz as the reference for the phase and amplitude calibration in this frequency region. The intensity ratio of these spectra is shown in Fig. 4.8b. Although a peak-like feature is recognized at around 1150 cm^{-1}, this feature is an artifact due to an incomplete normalization between the very small signals in the raw spectra in this region. Except for this, the intensity ratio is almost featureless and, in particular, no spectral feature is recognized at 1040 cm^{-1} where the absorption owing to SO_3^- stretch might appear. This indicates that the absorption by the $CF_3SO_3^-$ anion in the solution layer does not affect the VSFG spectra in this frequency region significantly.

Fig. 4.9 shows the obtained $|\chi^{(2)}|^2$ spectra at the acetonitrile/platinum interface with 0.1 M $LiCF_3SO_3$ electrolyte. Black broken curves are the fitted curves obtained with the square of Lorentz function. The detail of the fitting analysis is described in the later section. At the potentials more positive than 0.4 V, a clear band is observed at 1040 cm^{-1}, and its intensity increases as the electrode potential becomes more positive. Based on the frequency, this band is assignable to the SO_3^- symmetric stretch mode of $CF_3SO_3^-$ anion [105-107]. The appearance of this 1040 cm^{-1} band directly proves the adsorption of the $CF_3SO_3^-$ anion on the electrode at positive potentials. The spectra also indicate that the anion desorbs from the electrode at the negative potentials. Qualitatively, the potential dependence of the intensity of the SO_3^- symmetric band appears similar to that of the CH_3 symmetric and CN stretch bands of acetonitrile (Fig. 4.3 and Fig. 4.6). It is noted that $CF_3SO_3^-$ anion is expected to also show the CF_3 anti-symmetric stretch band at around 1160 cm^{-1} [105-107] but it is not recognized in the $|\chi^{(2)}|^2$ spectra. It is probably due to the weak Raman activity of this vibration. Fig. 4.10 shows the IR and Raman spectra of 0.1 M $LiCF_3SO_3$ acetonitrile solution in SO_3^- symmetric stretch region. Hence, the 1040 cm^{-1} band is focused in the following discussion about the structure of acetonitrile/platinum interface with 0.1 M $LiCF_3SO_3$ electrolyte.

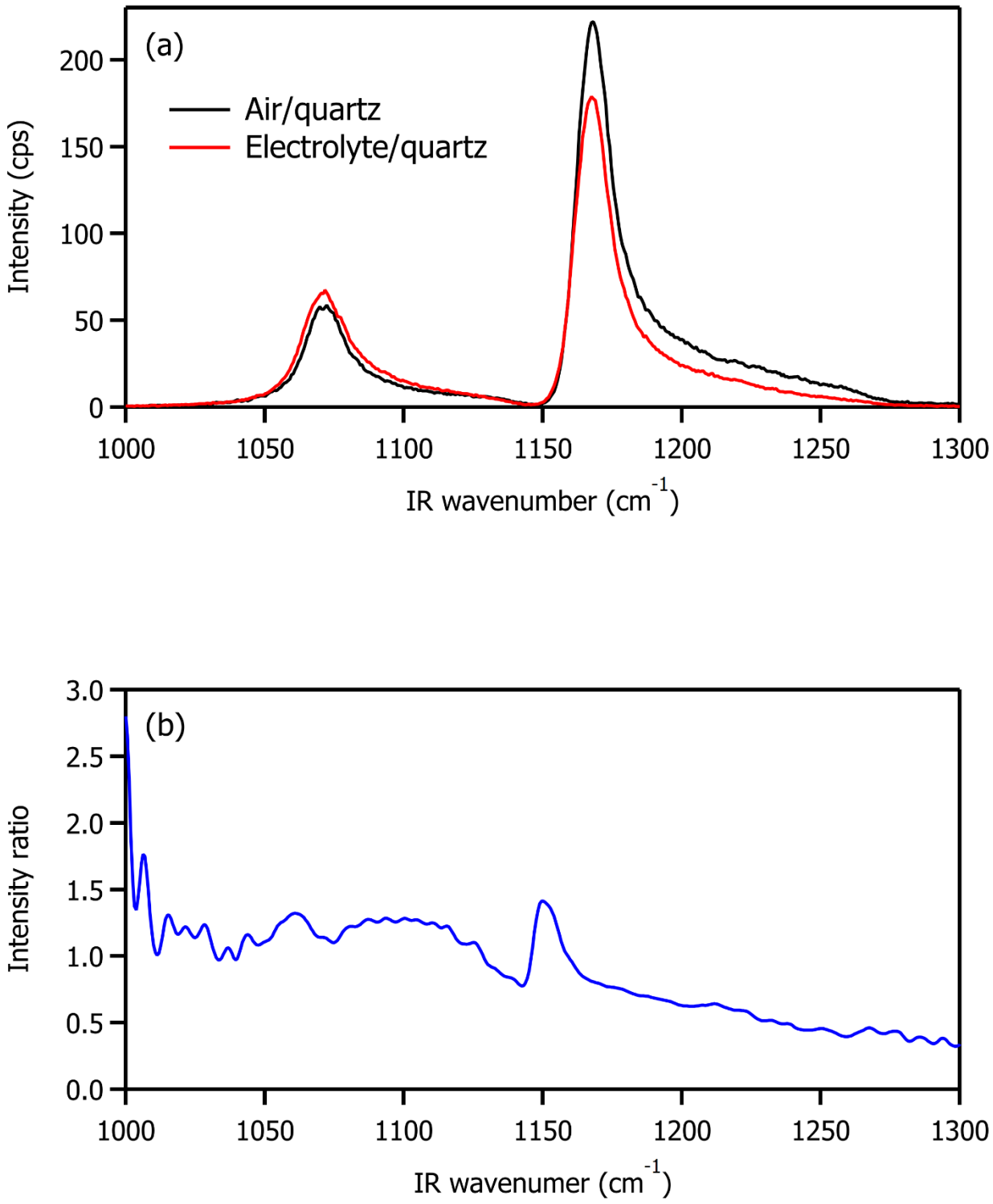

Fig. 4.8. (a) Un-normalized raw homodyne-detected VSFG spectra of the air/quartz and electrolyte/quartz interfaces. (b) Intensity ratio between the VSFG spectra of the electrolyte/quartz interface and the air/quartz interface.

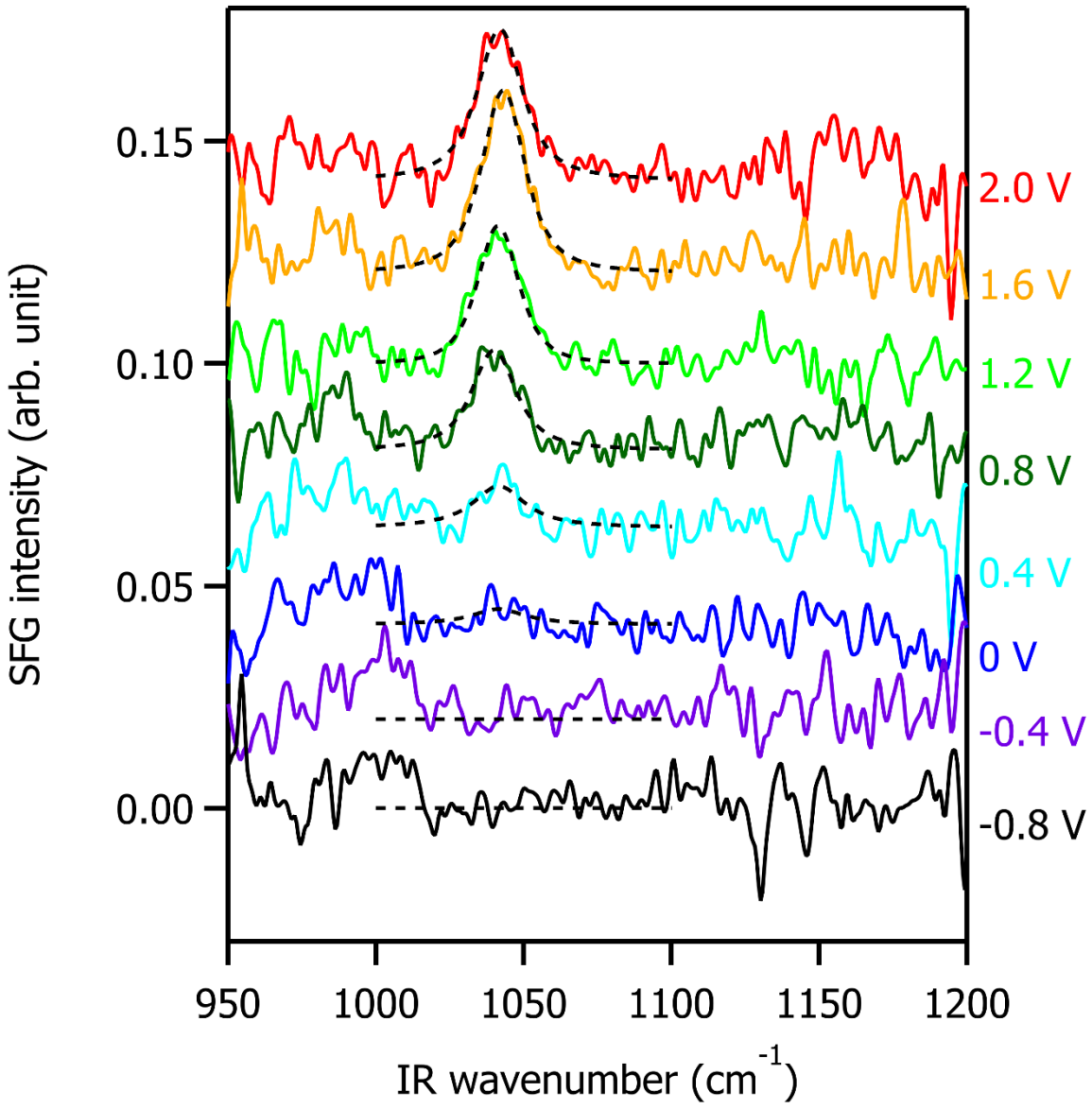

Fig. 4.9. VSFG intensity spectra of acetonitrile/platinum with 0.1 M $LiCF_3SO_3$ in the anion band frequency region. The sample spectra are normalized by an air/gold spectrum. Black broken curves are fitted curve obtained by the square of Lorenz function. 0.02 offsets are added for the comparison of spectra. The potential is quoted against Ag/Ag^+.

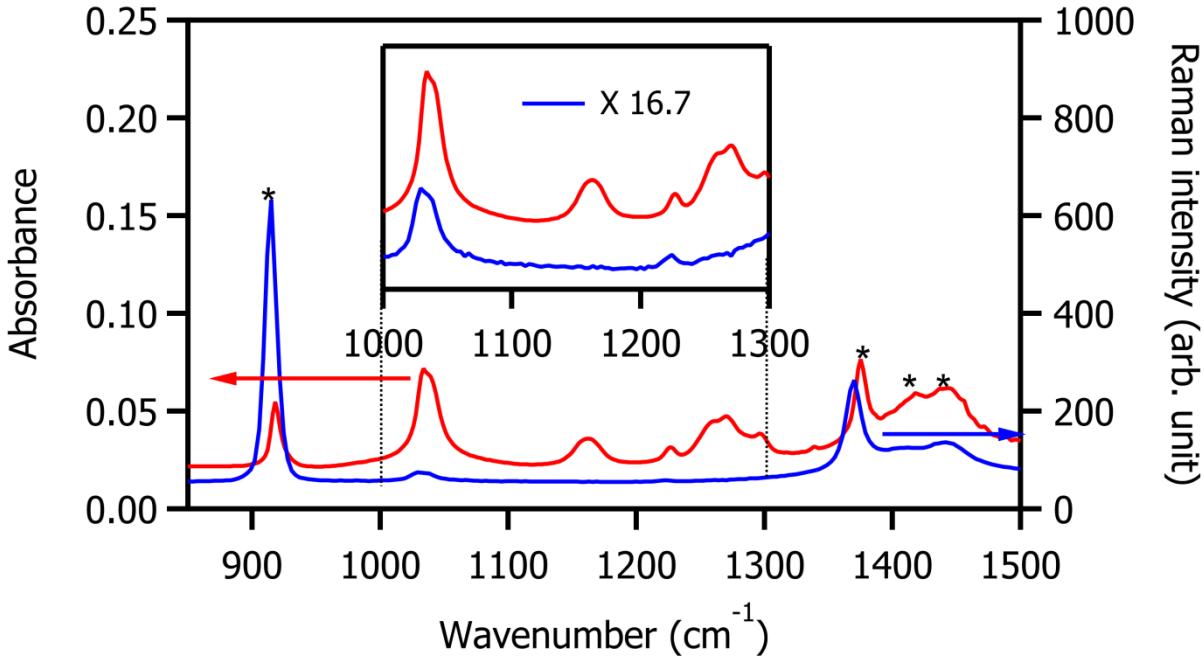

Fig. 4.10. Bulk IR (red) and Raman (blue) spectra of 0.1 M $LiCF_3SO_3$ in acetonitrile. The 1040 cm^{-1} peak is assigned to SO_3^- symmetric stretch [105-107]. The peak at 1160 cm^{-1} in the IR spectrum in (c) is attributed to the CF_3 anti-symmetric stretch. Note that the peaks shown by ⋆ are coming from solvent acetonitrile [108].

4.8 Structure of the acetonitrile/platinum interface

By gathering information obtained in the present study, the structure of the acetonitrile/platinum interface with 0.1 M $LiCF_3SO_3$ electrolyte can be discussed. First, I performed the fitting analysis as follows.

An $\mathrm{Im}\chi^{(2)}$ spectrum contains vibrationally non-resonant and vibrationally resonant contributions and is given by equation (3.4). Equation (3.4) is used for the fitting of $\mathrm{Im}\chi^{(2)}$ spectra in the CH stretch region.

In case that inhomogeneous broadening of a resonant band is significant, a Gaussian distribution of the resonant mode needs to be considered. In the CN stretch region, a very broad negative band owing to CN^- is observed, which is obviously broadened because of the inhomogeneity. For performing fitting of this band, a Lorentz function is replaced with a Gaussian function, and equation (3.4) is represented in the following general form.

$$\mathrm{Im}\chi^{(2)} = \mathrm{Im}\chi_{\mathrm{NR}}^{(2)} + \sum_{\mathrm{q}} \frac{A_{\mathrm{q}}\,\Gamma_{\mathrm{q}}}{(\omega_{\mathrm{q}} - \omega_{\mathrm{IR}})^2 + \Gamma_{\mathrm{q}}^{\,2}} + \sum_{\mathrm{p}} B_{\mathrm{p}} e^{-(\omega_{\mathrm{p}} - \omega_{\mathrm{IR}})^2/2\gamma_{\mathrm{p}}^2} \quad . \tag{4.3}$$

Here, B_{p} and γ_{p} represent the amplitude and width of Gaussian function, respectively, for an inhomogeneously broadened p-th vibrational mode. Equation (4.3) was used for the fitting of $\mathrm{Im}\chi^{(2)}$ spectra in the CN stretch region, using two Lorentz functions (for two CN stretch bands of acetonitrile) and one negative Gaussian function (for the CN^- band).

The homodyne-detected VSFG spectra, which correspond to $|\chi^{(2)}|^2$ spectra, are represented by equation (4.4).

$$\left|\chi^{(2)}\right|^2 = |\chi_{\mathrm{NR}}^{(2)}|^2 + \sum_{\mathrm{q}} \frac{A_{\mathrm{q}}^{\,2}}{(\omega_{\mathrm{q}} - \omega_{\mathrm{IR}})^2 + \Gamma_{\mathrm{q}}^{\,2}}$$

$$+2\sum_{\mathrm{q}} \frac{\mathrm{Re}\chi_{\mathrm{NR}}^{(2)} A_{\mathrm{q}}(\omega_{\mathrm{q}} - \omega_{\mathrm{IR}}) + \mathrm{Im}\chi_{\mathrm{NR}}^{(2)} A_{\mathrm{q}}\,\Gamma_{\mathrm{q}}}{(\omega_{\mathrm{q}} - \omega_{\mathrm{IR}})^2 + \Gamma_{\mathrm{q}}^{\,2}}$$

$$+\sum_{q\neq q'}\frac{A_q A_{q'}}{\left(\omega_q-\omega_{IR}-i\,\Gamma_q\right)\left(\omega_{q'}-\omega_{IR}+i\,\Gamma_{q'}\right)}\ . \tag{4.4}$$

Here, note again that $\chi^{(2)}_{NR}$ is a complex number $\chi^{(2)}_{NR}$ = Re $\chi^{(2)}_{NR}$ + Im $\chi^{(2)}_{NR}$. Equation (4.4) is used for the fitting of the SO_3^- stretch band measured with homodyne-detected VSG spectra.

Fig. 4.11 compares the amplitudes of the CH_3 symmetric stretch, CN stretch (at 2245 cm^{-1}), CN^- stretch and SO_3^- symmetric stretch bands observed at different electrode potentials, which were obtained by the fitting analysis. As clearly seen, the amplitude of the CH_3, SO_3^-, and CN bands increase as the electrode potential becomes more positive, in a manner similar to each other. This indicates that the amplitude of the vibrational bands of acetonitrile and the anion are strongly correlated. In contrast, the potential dependence of the broad negative CN^- band is clearly different from those of other bands, confirming that this band arises from a species different from free acetonitrile. Moreover, the signal due to CN^- decreases in accordance with the increase of the signals coming from the $CF_3SO_3^-$ anion and acetonitrile, implying that the interface structure changes with the change of the potential applied to the platinum electrode.

Based on the above potential dependence of different interfacial species, the structure at the acetonitrile/platinum interface with $LiCF_3SO_3$ electrolyte is proposed as illustrated in Fig. 4.12. At the negative potential, the interface does not have any distinct structure except that a small amount of acetonitrile is decomposed to the CN^- anion on defect sites of the electrode and is adsorbed on the electrode [29]. The acetonitrile molecules in the vicinity of the electrode exhibit no preferential orientation. On the other hand, at the positive potentials, the platinum electrode surface is covered by the $CF_3SO_3^-$ anions, repelling the CN^- anion. The adsorbed $CF_3SO_3^-$ anions interact with acetonitrile molecules and make them oriented with their CH_3 group pointing toward the anions on the electrode. Consequently, acetonitrile has net CH_3-down and CN-up orientation in the vicinity of the platinum electrode. It is not clear that why the acetonitrile does not show any net orientation at the interface at the negative potentials at the moment. One possibility is that because the charge of the electrode surface is well-delocalized and uniformly distributed, the charge density may not be high enough to induce a particular orientation of acetonitrile with a detectable magnitude. It might also be possible that the solvated cation in the vicinity of the electrode disturbs solvent orientation at the negative potentials.

Lastly, I mention the importance of complementary theoretical study to obtain a complete

molecular-level picture of the electrolyte/electrode interface. For the air/water interfaces, in fact, it has been shown that combination of HD-VSFG spectroscopy and MD-simulation is indispensable for elucidating the interface structure at the molecular level [109, 110]. For the acetonitrile/platinum interface investigated in this study, for example, the orientation of CN^- cannot be determined only from the experimental $\mathrm{Im}\chi^{(2)}$ because the hyperpolarizability of cyanide is not known. DFT calculation of the system including the transition metal electrode is required for obtaining reliable hyperpolarizability of CN^- for discussing the orientation of the adsorbed CN^-.

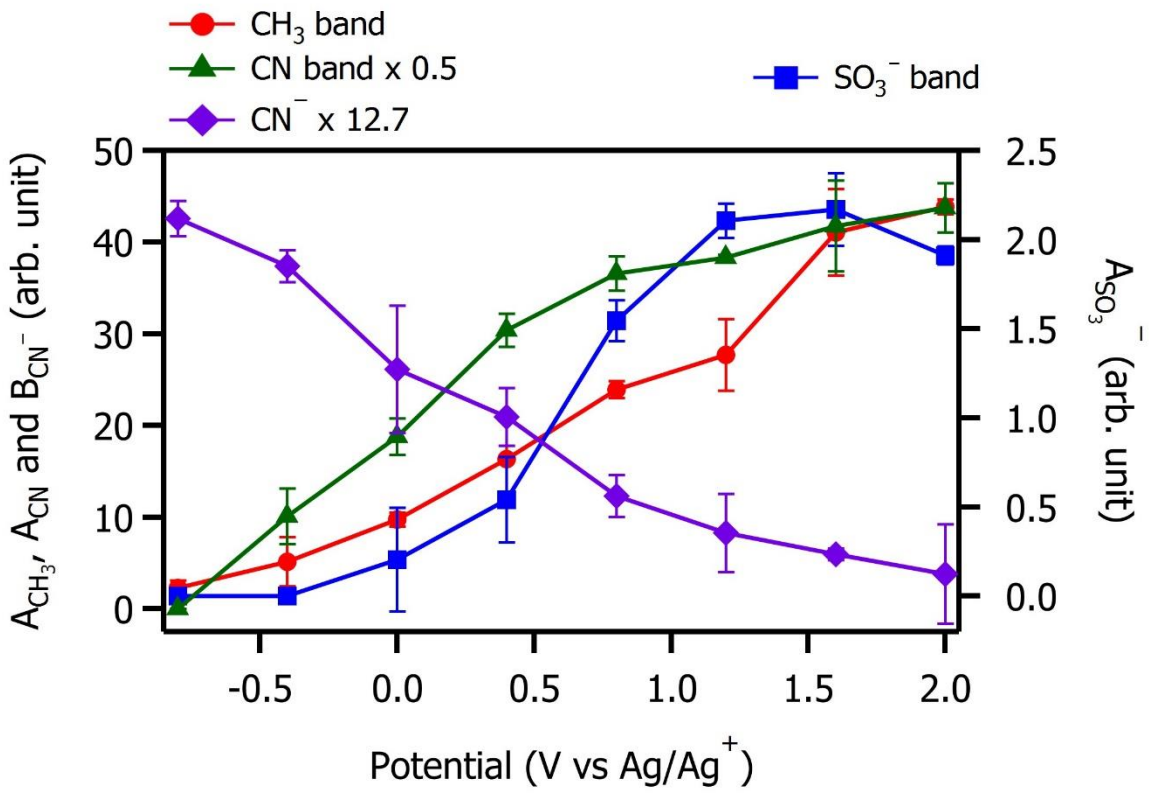

Fig. 4.11. Electrode potential dependence of the amplitudes of the CH_3 stretch (red circle), the CN stretch (green triangle) bands of free acetonitrile, the CN^- (purple diamond) and SO_3^- (blue square) bands in the spectra of acetonitrile/platinum interface with 0.1 M $LiCF_3SO_3$ electrolyte. The data points are averages of two negative-going scans from 2.0 V to -0.8 V. The error bars indicate the variations between the two experiments at each potential.

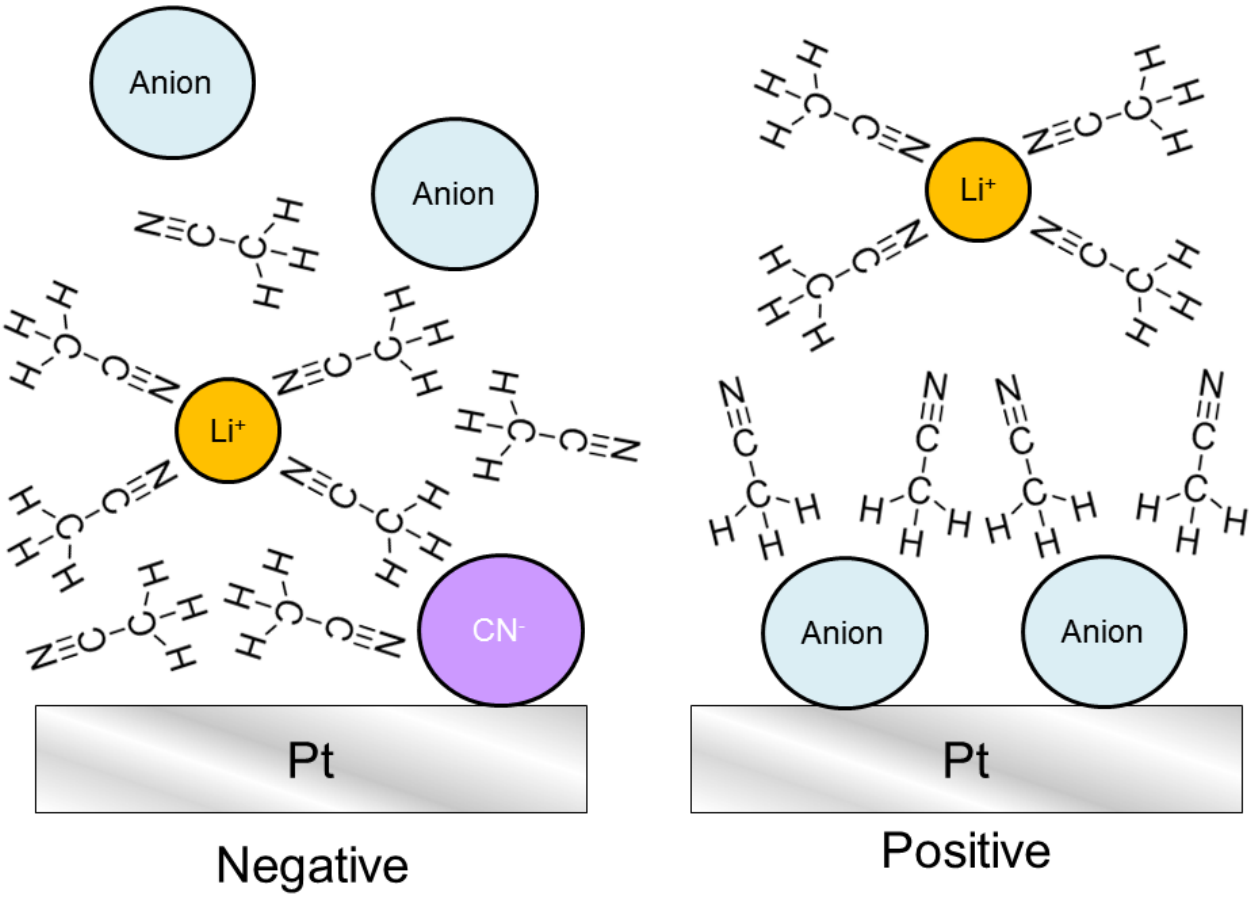

Fig. 4.12. Schematics of the structure of the acetonitrile/platinum interface with $LiCF_3SO_3$ electrolyte.

4.9 Conclusion of chapter 4

HD-VSFG measurements at an electrolyte/electrode interface are realized by employing the in-situ reference method, and succeeded in the observation of the potential-dependent orientation of the interfacial molecule at the electrode for the first time. Electrochemical HD-VSFG measurements at the acetonitrile/platinum interface with 0.1 M $LiCF_3SO_3$ electrolyte revealed that the acetonitrile is pointing their CH_3 group toward the positively charged electrode. Because the signal intensity due to this oriented acetonitrile is well correlated with that of the $CF_3SO_3^-$ anion adsorbed at the interface, it is proposed that this CH_3-down orientation of the interfacial acetonitrile is induced by the anion adsorption on the electrode surface. The present study suggests that the essential role of the anion adsorption for determining the property of solvent molecules at the electrode interface. This work demonstrates that HD-VSFG spectroscopy is a very powerful method also for elucidating the structure at electrolyte/electrode interfaces at the molecular level.

5. HD-VSFG measurement of super-concentrated electrolyte/platinum interfaces

5.1. Introduction of super-concentrated electrolyte

Rechargeable batteries have played more and more important roles in modern lives. Various rechargeable batteries such as lead acid battery, nickel-hydrogen battery, lithium-ion battery (LIB) have been developed and used for versatile purposes, such as vehicles, laptop computers, smart-phones and so on. Especially, LIB has drastically contributed to the society owing to its high voltage. The voltage of LIB is in fact high enough to decompose its own solvent. Nevertheless, stable operation of LIB is realized because of the formation of so-called solid electrolyte interphase (SEI): Ethylene carbonate (EC), which is a solvent of LIB, reductively decomposes at the first charging process and the decomposition product covers the surface of the carbon electrode [3, 111]. Because lithium ions can pass through the SEI while the solvent EC molecules cannot, the continuous decomposition of solvent molecules are inhibited by the presence of the SEI, which enables reversible intercalation of lithium ions at the carbon electrode. Thus, controlling unwanted side reactions other than a battery reaction is essential for the stable operation of high voltage rechargeable batteries.

Because of the increasing demand for high performance batteries, next-generation batteries have been under development in order to achieve higher voltage and energy density than LIB. As in the case of LIB, it is essential to control unwanted solvent decomposition for developing high voltage batteries. A lot of worldwide efforts have been made for developing an electrolyte solution that can be used for novel electrode active materials. Recently, super-concentrated electrolyte solution has attracted much attention as one of the general strategies to design new electrolyte solution for a high voltage battery as described in detail below.

In general, acetonitrile is reductively decomposed easily when in contact with metal lithium. However, it has been reported that acetonitrile becomes stable even in contact with metal lithium when it dissolves saturate amount of $LiN(CF_3SO_2)_2$ (LiTFSA) electrolyte [112]. The mechanism of the high stability of acetonitrile has been discussed based on spectroscopic measurements in bulk phase and DFT-MD calculations as follows: Increasing the salt concentration enhances interactions between cations and anions and/or solvents, leading to the depletion of free solvents, which do not solvate cations. This results in the increase of the number of contact ion pairs (CIPs) and aggregates (AGGs) between the lithium cation and TFSA anion in super-concentrated electrolyte, which induces the down-shift of the lowest unoccupied molecular orbital (LUMO) level of anion, making it lower than the LUMO level of solvents. As a result, the reductive decomposition of the anions takes place prior to the solvent decomposition [112, 113]. Because the decomposition product of anions at the

electrode surface is insoluble in acetonitrile solution and forms a SEI-like layer at the electrode surface, it protects the electrolyte and solvent from the further decomposition.

Several works have followed the above-mentioned pioneering work and found that the stabilization of solvent in super-concentrated electrolytes is not specific to the combination of acetonitrile and LiTFSA but is rather general [114, 115]. Hence the use of super-concentrated electrolytes becomes the new standard strategy to design new electrolyte solutions for next-generation batteries. However, to my best knowledge, there has been no report about in-situ observation of the structure of super-concentrated electrolyte/electrode interfaces and the formation of the anion-decomposition layer.

In this study, HD-VSFG spectroscopy was applied to a 0.1 M and a 4.2 M LiTFSA acetonitrile solution/platinum interface in order to clarify the origin of solvent stability in super-concentrated electrolytes. In previous reports, it has been reported that acetonitrile decomposes by a reductive reaction and CN^- is produced [116, 117]. In addition, our previous study showed that CN^- is formed on a platinum electrode by a catalytic decomposition of acetonitrile. Thus, reactivity of acetonitrile can be clearly probed by monitoring the CN^- band at the electrode. In the present study, the vibrational band assigned to the CN^- as well as free acetonitrile is observed at a platinum electrode in the diluted electrolyte system. On the other hand, in the concentrated electrolyte system, those bands disappear while the band associated with the decomposition product of $TFSA^-$ anions as well as solvating acetonitrile (i.e., acetonitrile solvating a lithium cation) is observed. These in-situ observations clearly indicate that acetonitrile decomposes in the diluted electrolyte solution while $TFSA^-$ anion decomposes in the concentrated electrolyte solution. An additional ex-situ measurement reveals that the TFSA-decomposition product on the electrode is insoluble in acetonitrile, supporting the formation of SEI-like protection layer on the electrode. Our observations support the mechanism previously proposed based on ex-situ analysis and DFT-MD calculation.

5.2. Spectra in diluted condition

5.2.1 Interface structure of 0.1 M LiTFSA electrolyte system before applying negative potentials

Fig. 5.1 shows the $\mathrm{Im}\chi^{(2)}$ spectra and VSFG spectrum of the acetonitrile/platinum interface with 0.1 M LiTFSA electrolyte before applying negative potentials and the corresponding IR spectra. Fig. 5.1a and Fig. 5.1b are in the CH stretch region and CN stretch region, respectively. And Fig. 5.1c shows the VSFG spectrum in SO_2 and CF_3 stretch region. In the CH stretch region, the $\mathrm{Im}\chi^{(2)}$ spectrum shows a positive band at 2940 cm^{-1}, which is assigned to the CH_3 symmetric stretch of free

acetonitrile. In the CN stretch region, the positive band is clearly observed at 2250 cm^{-1}, which is assigned to the CN stretch of free acetonitrile. The positive signs of the CN and CH bands consistently indicate that the acetonitrile is in the CH_3-down and CN-up orientation as mentioned in chapter 4. Following the discussion in chapter 4, it can be considered that CH_3-down, CN-up orientation is induced by $TFSA^-$ anion adsorption. However, the corresponding VSFG spectra in the SO_2 and CF_3 stretch region (Fig 5.1c) shows no clear feature. Therefore, it may be considered that $TFSA^-$ anion is adsorbed at the electrode interface but has no preferential up/down orientation. The CN^- band which might appear around 2100 cm^{-1} as observed in chapter 4 with 0.1 M $LiCF_3SO_3$ is not observed in the present experimental condition. The absence of the CN^- band can be explained by the preferential adsorption of $TFSA^-$ anion on the electrode which prevents the CN^- adsorption.

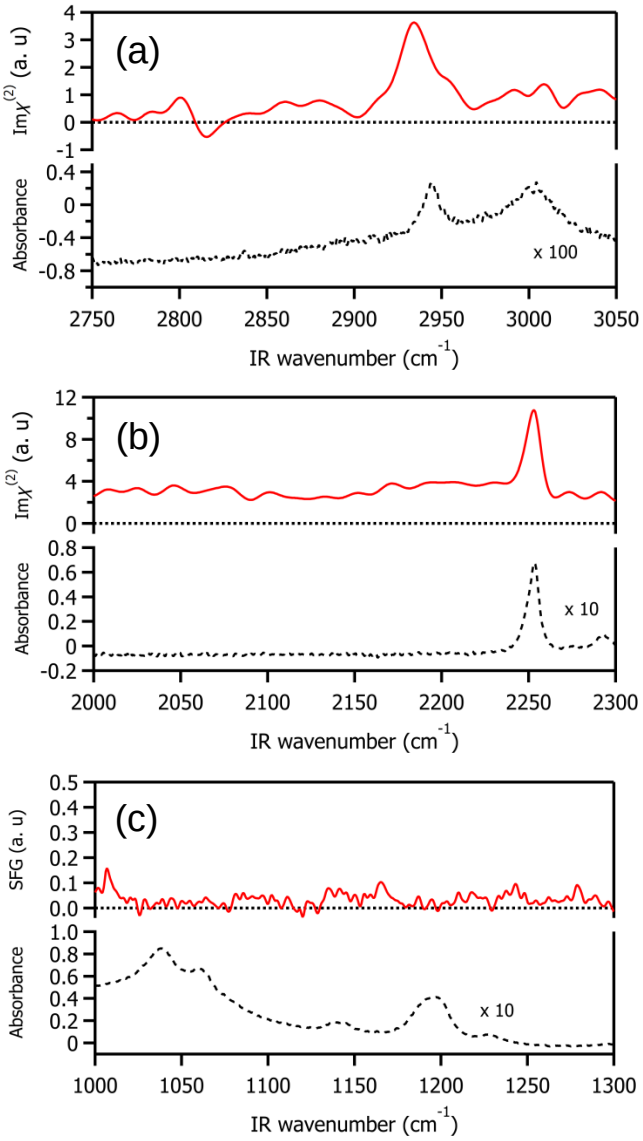

Fig. 5.1. Im$\chi^{(2)}$ spectra and IR spectra of acetonitrile/platinum with 0.1 M LiTFSA electrolyte before applying negative potentials in (a) the CH stretch region and (b) the CN stretch region. (c) VSFG spectrum and IR spectrum in the SO_2 and CF_3 stretch region. The Im$\chi^{(2)}$ spectra and VSG spectrum are shown by red curves, and IR spectra are shown by black broken curves.

5.2.2 Interface structure of 0.1 M LiTFSA electrolyte system with applying negative potentials

After measuring the initial state of the electrode at 0.4 V shown in the previous section, the electrode potential was scanned between 0.4 V and -2.8 V. The $\mathrm{Im}\chi^{(2)}$ spectra change drastically during the first cycle of the potential scan, but the potential at which the changes take place is not reproducible. Because such irreproducible behavior is not seen in the second cycle of the scan, in the following results and discussion, I focus on the second scan data. Fig. 5.2 shows the $\mathrm{Im}\chi^{(2)}$ spectra and VSFG spectrum of the acetonitrile/platinum interface with 0.1 M LiTFSA electrolyte at the potential region between -2.8 V and 0.4 V with a 0.4 V potential increment. The data shown in Fig 5.2 are the spectra measured in the positive going potential scan in the second cycle.

Fig. 5.2a shows the $\mathrm{Im}\chi^{(2)}$ spectra of the acetonitrile/platinum interface in the CH stretch region in the second positive-going scan. The negative band is observed around 2940 cm^{-1} and the band keeps the negative sign during the scan. As discussed previously, the negative band indicates the CH_3-up orientation which is different from that observed initially at 0.4 V before the potential scan. This suggests that some change associated with acetonitrile takes place during the first potential scan.

Fig. 5.2b shows the $\mathrm{Im}\chi^{(2)}$ spectra of the acetonitrile/platinum interface in the CN stretch region. The band which is assigned to the CN stretch of free acetonitrile is still observed. The sign of this band is positive and the amplitude is similar to that observed before the potential scan and almost constant in the whole potential region. This result suggests that the CN-up acetonitrile exists continuously even at the very negative potential (-2.8 V).

A new band is observed in the frequency region between 2000 – 2100 cm^{-1} which is not observed in the corresponding bulk IR spectrum (Fig. 5.1b), and the peak frequency varies depending on the electrode potential. The peak frequency and peak shift are similar to that observed in a prior SERS study [29]. Following the SERS study, this band is assignable to the CN^- adsorbed on the electrode [29] and the frequency shift is attributable to an electrochemical Stark effect [118-120] combined with a charge transfer [29]. The observation of the CN^- band is the manifestation of the acetonitrile decomposition in the 0.1 M LiTFSA solution.

Combining the result in the CH region (negative CH band: CH_3-up orientation) with that in the CN region (positive CN band: CN-up orientation), there must be a species that gives rise to a negative CH band (CH_3-up) but not to a negative CN band. To satisfy this condition, η^2 species is considered, whose CN axis is parallel to the electrode surface while CH_3 group is pointing up [104, 121-123]. Such species does not contribute to the CN band but only to the negative CH band because the CN stretch parallel to the surface is SFG inactive. It has been proposed that η^2 species is the

reaction intermediate of acetonitrile decomposition [122, 123]. The observation of the negative CH band suggests that the product of the number density, orientation distribution function and hyperpolarizability of η^2 species is larger than that of the free acetonitrile. Among these factors, number density of η^2 species cannot exceed that of free acetonitrile, as it is limited by the surface area of the electrode. In contrast, the latter two factors may be larger for η^2 species: The orientation distribution function of η^2 species may be higher than that of free acetonitrile because it is tightly bound on the electrode with a particular tilt angle. The hyperpolarizability of η^2 species may be enhanced by interacting with the electrode. Thus, it is possible that the negative CH band of η^2 species overwhelm the positive CH band of free acetonitrile, although at the moment it is difficult to identify the reason for the appearance of η^2 species in $\mathrm{Im}\chi^{(2)}$ spectra. The negative sign in the whole potential region suggests that once η^2 species is formed, it remains on the electrode in the present potential region.

Fig. 5.2c shows VSFG spectra of the acetonitrile/platinum interface with 0.1 M LiTFSA electrolyte in the SO_2 and CF_3 stretch region at each electrode potential. During the potential scan, no specific feature is observed (the bulk IR absorption is shown in Fig.5.1c). This result indicates that $TFSA^-$ is not in the very vicinity of the electrode or $TFSA^-$ has no preferential up/down orientation even after the potential scan. The former picture is more likely because the η^2 species and CN^- are adsorbed at the electrode surface as observed in the CH and CN stretch regions.

From the above results, the structure of acetonitrile/platinum with 0.1 M LiTFSA electrolyte can be discussed. The schematic drawing of the proposed interface structure is shown in Fig. 5.3. The negative CH band is assignable to the η^2 species, which is an intermediate species of acetonitrile decomposition. The positive CN band is due to free acetonitrile which takes the CN-up orientation. The positive CH band due to the free acetonitrile (CH_3-down orientation) is considered to be overwhelmed by the negative CH signal from η^2 species. The presence of the CN^- band clearly indicates that CN^- is produced by the acetonitrile decomposition and the band shift depending on the electrode potential is clear evidence that CN^- is chemisorbed. No significant feature in anion stretch region indicates the $TFSA^-$ is not in the vicinity of the electrode surface or the $TFSA^-$ shows no preferential orientation. Either way, the $TFSA^-$ does not play an important role in the dilute electrolyte solution.

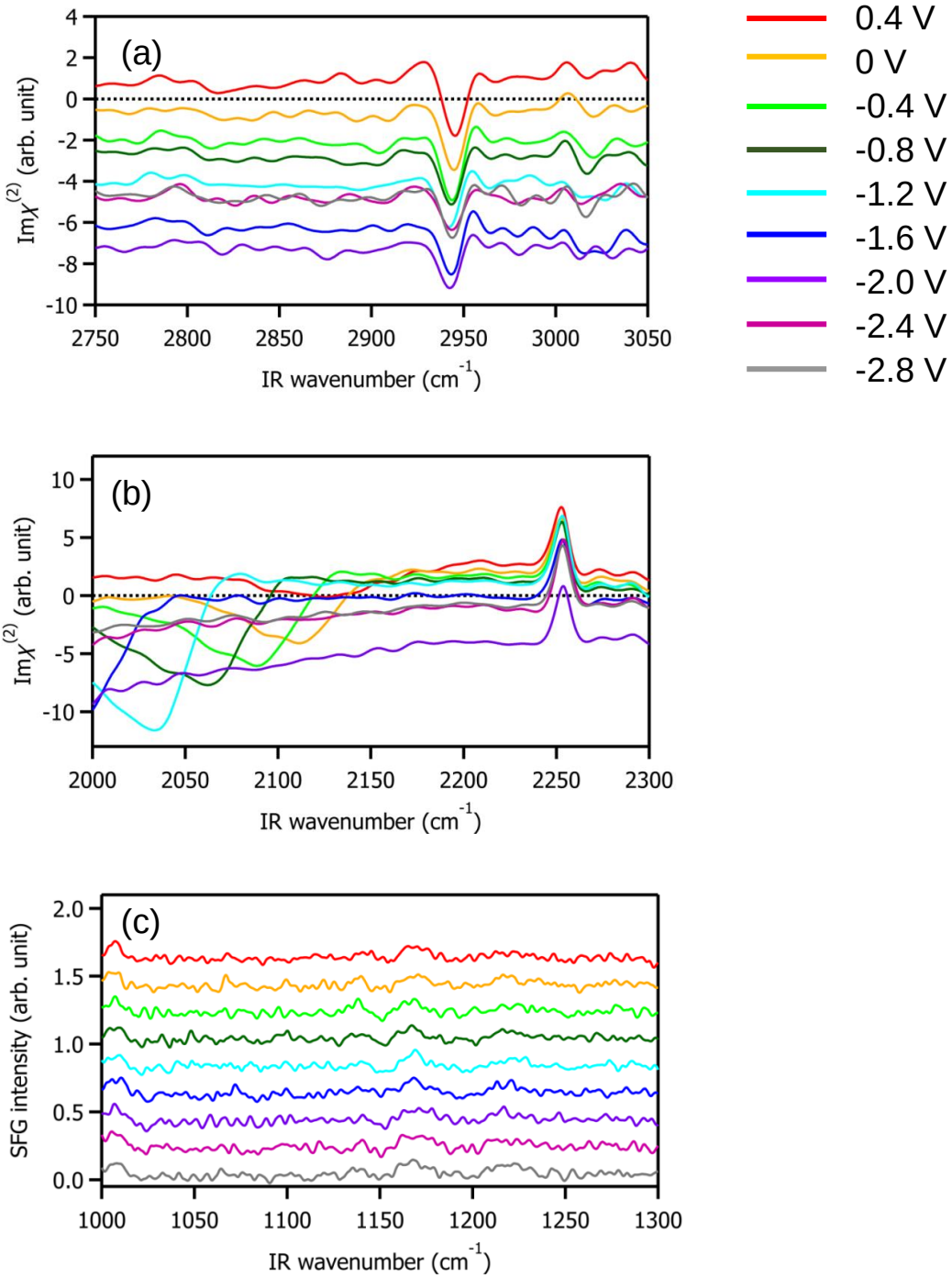

Fig. 5.2. Im$\chi^{(2)}$ spectra of acetonitrile/platinum with 0.1 M LiTFSA electrolyte at each potential in (a) the CH stretch region and (b) the CN stretch region. (c) VSFG spectra of acetonitrile/platinum with 0.1 M LiTFSA electrolyte in the SO_2 and CF_3 stretch region. 0.2 Offsets are added in (c) for comparison.

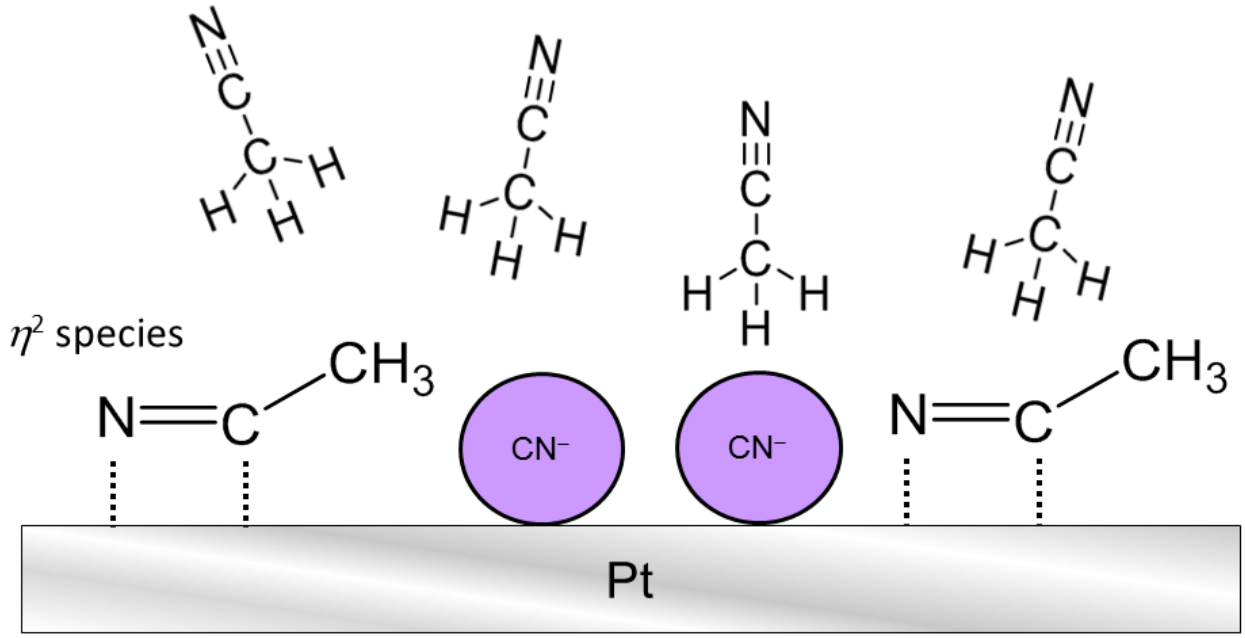

Fig. 5.3. Interface structure of acetonitrile/platinum interfaces with 0.1 M LiTFSA electrolyte.

5.3. Spectra in super-concentrated condition

5.3.1 Interface structure of 4.2 M LiTFSA electrolyte system before applying negative potentials

Fig. 5.4 shows the $\mathrm{Im}\chi^{(2)}$ spectra and VSFG spectrum of the acetonitrile/platinum interface with 4.2 M LiTFSA electrolyte before applying negative potentials, accompanied by the IR spectra of the corresponding bulk solution. Fig. 5.4a and Fig. 5.4b are in the CH stretch and the CN stretch regions, respectively. In the CH stretch region, the initial spectrum shows no clear feature, suggesting a random orientation of acetonitrile. In the CN stretch region, the dispersive feature is observed around 2275 cm^{-1}, which is assigned to the CN stretch of acetonitrile solvating a lithium cation. The observation of the solvating acetonitrile but not the free acetonitrile suggests that solvating acetonitrile is predominant even at the vicinity of the electrode surface when the bulk solution is saturated. The reason why the 2275 cm^{-1} band has dispersive shape is not clear yet. One possibility is that the frequency of the CN stretch of the solvating acetonitrile is slightly perturbed in the vicinity of the electrode and up-oriented CN and down-oriented CN bonds have slightly different frequencies. In the concentrated solution, it is known that a part of solvating acetonitrile is replaced by the $TFSA^-$ and contact ion pairs (CIPs) and/or aggregates (AGGs) are formed [112, 113, 124] in which the anions solvate one or multiple lithium cations, respectively. By the replacement of acetonitrile, the symmetry of the solvation shell becomes lower and the CN stretch mode of solvating acetonitrile may be SFG active. Heterogeneous nature of CIPs and AGGs structure may allow the up-oriented and down-oriented CN bonds to have slightly different frequency, giving rise to the dispersive CN band. In the same configuration, however, the signals in the CH_3 stretch region are considered to be canceled more effectively because the frequency of the CH_3 group is insensitive to the environment, as seen in the bulk IR spectrum (Fig. 5.4a). To identify the reason, contributions of DFT calculation and MD-simulation including ions, solvents, and metal electrodes are essential.

Fig. 5.4c shows VSFG spectra of the acetonitrile/platinum interface with 4.2 M LiTFSA electrolyte in the SO_2 and CF_3 stretch region before applying negative potentials. No clear feature is observed in the initial VSFG spectrum, indicating that $TFSA^-$ anion has no preferential up/down orientation.

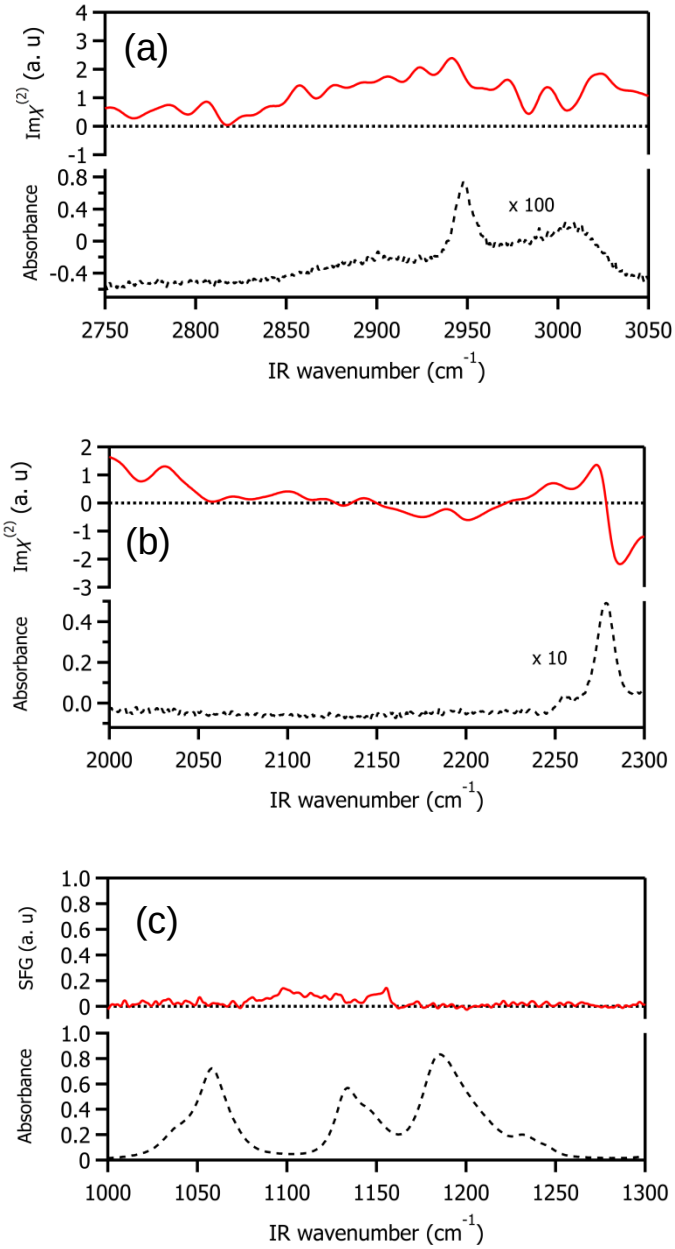

Fig. 5.4. Im$\chi^{(2)}$ spectra and IR spectra of acetonitrile/platinum with 4.2 M LiTFSA electrolyte before applying negative potentials in (a) the CH stretch region and (b) the CN stretch region. (c) VSFG spectrum and IR spectrum in the SO_2 and CF_3 stretch region. The Im$\chi^{(2)}$ spectra and VSG spectrum are shown by red curves, and IR spectra are shown by black broken curves.

5.3.2 Interface structure of 4.2 M LiTFSA electrolyte system with applying negative potentials

Fig. 5.5 shows the $\mathrm{Im}\chi^{(2)}$ spectra and VSG spectrum of the acetonitrile/platinum interface with 4.2 M LiTFSA electrolyte at the potential ranged between -2.8 V and 0.4 V with a 0.4 V potential increment.

Figs. 5.5a and 5.5b show the $\mathrm{Im}\chi^{(2)}$ spectra of the acetonitrile/platinum interface in the CH and CN stretch regions. In both of these frequency regions, $\mathrm{Im}\chi^{(2)}$ spectra do not show any significant change independent of the applied potentials except for the shift of the non-resonant background, indicating that the solvating acetonitrile structure does not change with the electrode potential. Most importantly, unlike the dilute system, any feature associated with η^2 species or CN^- is not observed in the 4.2 M LiTFSA solution. This result clearly shows that the acetonitrile does not decompose in super-concentrated electrolyte, being consistent with the previous report [112]. Below, I discuss the reason why acetonitrile is stable even at the very negative potential in 4.2 M LiTFSA electrolyte solution.

Fig. 5.5c shows VSFG spectra of the acetonitrile/platinum interface with 4.2 M LiTFSA electrolyte in the SO_2 and CF_3 stretch region at each electrode potential. The strong band is observed at 1160 cm^{-1} in the whole potential region. Compared with the corresponding IR spectrum shown in Fig. 5.4c, it is clear that the observed peak frequency is different from that of the bulk IR absorption. This suggests that a new species is produced at the electrode, which is considered to be the decomposition product formed on the electrode.

The previous reports have suggested that the $TFSA^-$ anion decomposes prior to acetonitrile and the TFSA-decomposition product forms an insoluble layer [112]. This decomposition is induced by the down-shift of the LOMO energy level of $TFSA^-$ anion as mentioned in section 5.1 [113]. In the previous report, the ex-situ X-ray photoelectron spectroscopy clearly showed that the abundance of oxygen, fluorine, sulfur and nitrogen elements increased after electrochemical charge and discharge processes [112]. Therefore, it was considered that the insoluble TFSA-decomposition product was piled up on the electrode surface and forms a decomposition-product layer. The TFSA-decomposition layer inhibits the acetonitrile and TFSA from direct attaching to the electrode and further reductive decomposition.

To confirm our assignment of the new band, ex-situ VSFG measurement, i.e., a measurement of air/platinum interface is performed after the electrochemical measurements. Fig. 5.6 shows the VSFG spectra of the air/platinum before/after the in-situ measurements. The VSFG spectra of the acetonitrile/platinum interfaces measured in-situ at 0.4 V is also shown by the red curve. The black curve in Fig. 5.6 shows the VSFG spectra of the air/platinum interface before the electrochemical

measurement. It is clear that no band is observed before the electrochemical measurements. After the electrochemical measurement, the sample substrate was washed by acetonitrile and acetone, then dried in an oven for one day. And, VSFG spectrum of the air/platinum interface was measured as shown by the blue curve. A strong peak is observed around 1150 cm^{-1} in the VSFG spectrum of the air/platinum interface. This result strongly supports that some species that is insoluble in acetonitrile is formed on the electrode. The peak frequency in the air/platinum spectrum is slightly different from that in the in-situ spectrum but this can be attributed to the difference in the measurement environment between in air and in acetonitrile. Thus, it is reasonable to assign the new band to the TFSA-decomposition product layer. To my best knowledge, this is the first time to observe the decomposition layer in-situ.

Now, the interface structure of acetonitrile/platinum interfaces with 4.2 M LiTFSA electrolyte can be discussed. The schematic drawing of the proposed interface structure is shown in Fig. 5.7. The observation of the new band at 1160 cm^{-1} combined with the absence of the CN^- band and η^2 species band strongly suggests that the electrode interface is covered by the TFSA-decomposition layer and that the decomposition of acetonitrile is inhibited. It is considered that TFSA-decomposition layer on the platinum electrode protects acetonitrile from reductive decomposition. No significant change was observed for the solvation structure of acetonitrile in the concentrated solution.

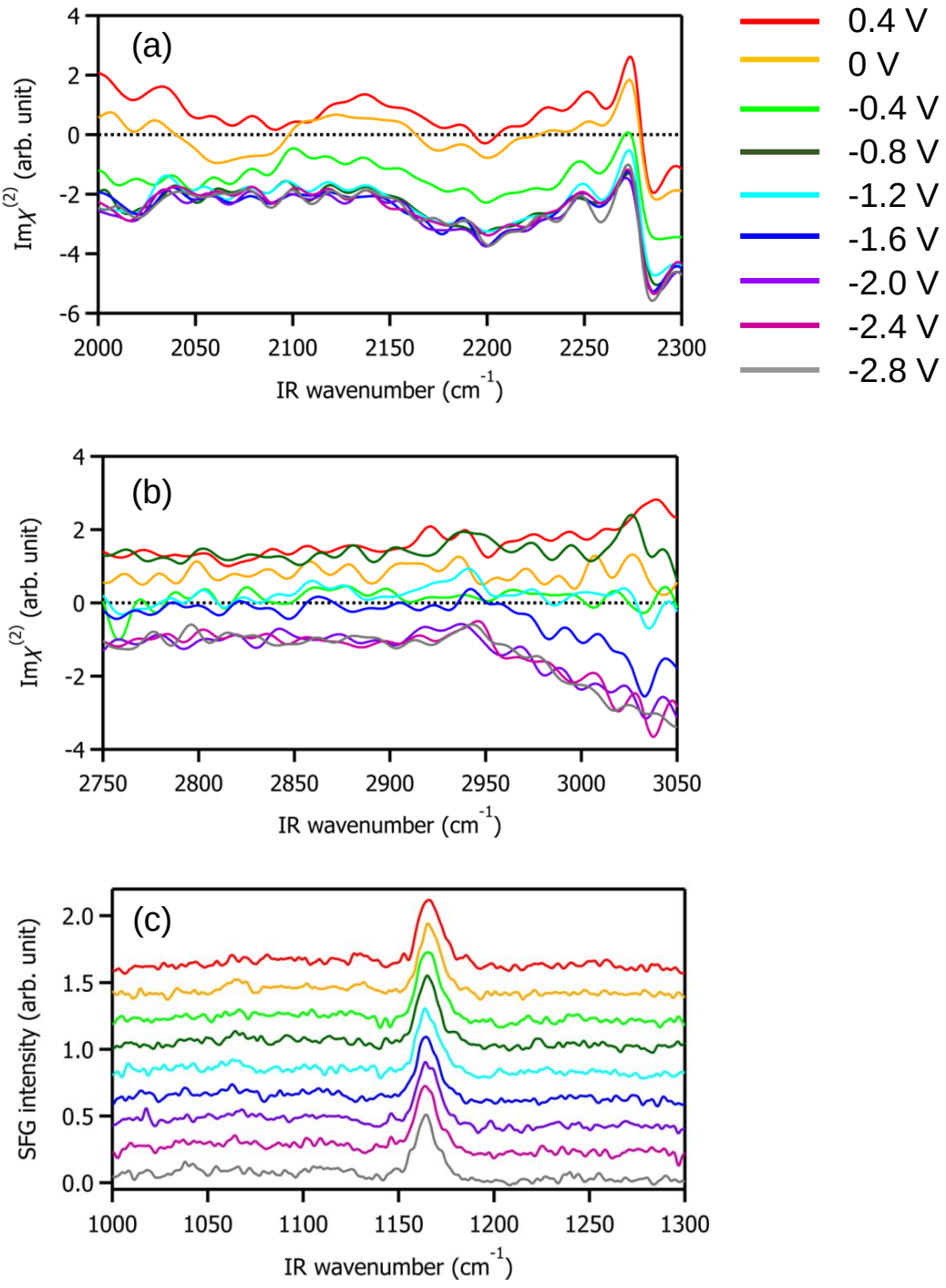

Fig. 5.5. Im$\chi^{(2)}$ spectra of acetonitrile/platinum with 4.2 M LiTFSA electrolyte at each potential in (a) the CH stretch region and (b) the CN stretch region. (c) VSFG spectra of acetonitrile/platinum with 4.2 M LiTFSA electrolyte in the SO_2 and CF_3 stretch region. 0.2 offsets are added in (c) for comparison.

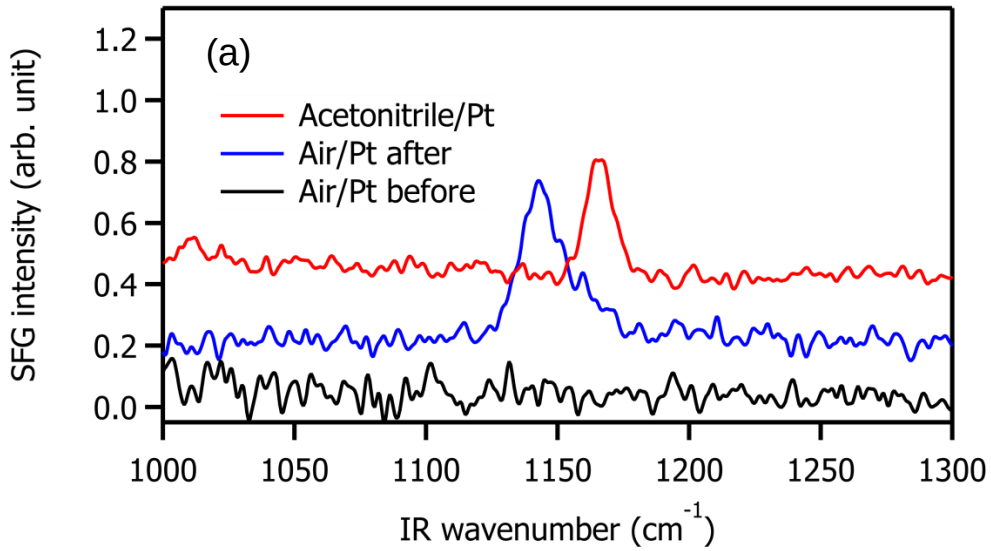

Fig. 5.6. VSFG spectra of acetonitrile/platinum (red), air/platinum after the electrochemical measurement (blue) and air/platinum before the electrochemical measurement (black). 0.2 offsets are added for the comparison.

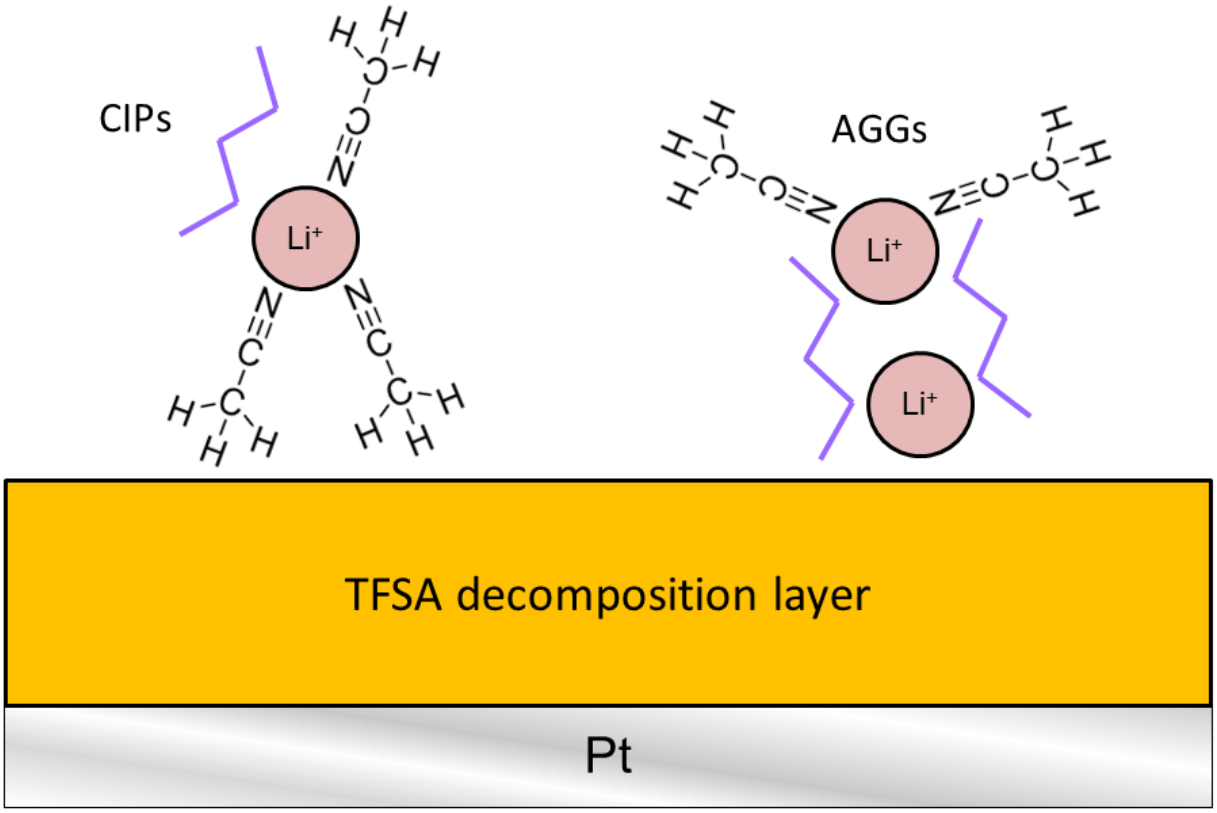

Fig. 5.7. Interface structure of acetonitrile/platinum interfaces with 4.2 M LiTFSA electrolyte.

5.4. Conclusion of chapter 5

HD-VSFG spectroscopy was applied to acetonitrile/platinum interfaces with 0.1 M and 4.2 M LiTFSA electrolyte. HD-VSFG measurements in the dilute 0.1 M LiTFSA solution revealed that acetonitrile decomposes and CN^- is produced. The CN^- band shows frequency shift depending on the electrode potential, suggesting the chemisorption of CN^-. Moreover, the presence of η^2 species is indicated by the negative band in the CH region. On the other hand, in the concentrated 4.2 M LiTFSA solution, no band associated with CN^- or η^2 species is observed, indicating that acetonitrile does not decompose in the 4.2 M LiTFSA solution. The new band in the SO_2 and CF_3 stretch region is observed in the VSFG spectra. The resonance frequency is different from the bulk IR absorption, suggesting the formation of new product on the electrode surface. The formation of TFSA-decomposition layer is observed in-situ for the first time in the present study. The air/platinum measurement after the electrochemical HD-VSFG measurements clearly shows that the band is still observed after washing the sample substrate. This result supports the insoluble layer is formed on the electrode surface.

6. Summary and Future perspectives

6.1. Summary of the thesis

In this thesis study, electrochemical HD-VSFG spectroscopy has been realized by developing the in-situ reference method and this advanced technique was applied to prototypical electrolyte/electrode interfaces and revealed potential-dependent structure of those interfaces.

Previous VSFG studies on electrolyte/electrode interfaces have been done by homodyne detection. Thus the orientation of interfacial molecules was discussed only by theoretical calculation and/or intuition based on simple electrostatic interaction [49]. This is because the phase information is lost in the homodyne-detected VSFG spectra. Although HD-VSFG spectroscopy which provides the phase information has been utilized for the study of simple interfaces such as air/water, silica/water, etc., it was not applied to electrolyte/electrode interfaces due to the lack of the phase reference available in the electrochemical condition. As described in chapter 3, the in-situ reference method, in which a metal film electrode is deposited on the half of the surface of quartz substrate, is essential to realize the electrochemical HD-VSFG measurements. The validation of the in-situ reference method was examined by measuring the ODT SAM on the platinum electrode, which has CH_3-up orientation in the terminal methyl group, in air and water. The measurements clearly showed that the spectral features do not change noticeably both in air and water. Therefore, it is validated that the in-situ reference method can calibrate the phase and amplitude of the SF signal even at the liquid/solid interfaces.

Employing the developed in-situ reference method, HD-VSFG spectroscopy was applied to an acetonitrile/platinum with 0.1 M $LiCF_3SO_3$, a prototypical electrochemical interface. This is the first time to realize the electrochemical HD-VSFG measurement for real electrochemical interfaces with phase and amplitude calibration. In the obtained $\mathrm{Im}\chi^{(2)}$ spectra, the positive bands are observed both in the CH stretch region and the CN stretch region at the positive potential. With going to more negative potential, the peak amplitude decreases, suggesting the orientation of acetonitrile changes with the electrode potential. The positive bands indicate that acetonitrile is in CH_3-down and CN-up orientation, which is opposite to the previous interpretation by a conventional VSFG study [49]. The reason of CH_3-down and CN-up orientation of acetonitrile is considered due to anion adsorption because of the following reasons. Homodyne VSFG spectra in 1000 – 1200 cm^{-1} region, where quartz reference cannot be used as a reference due to its own vibrational resonance, clearly exhibit the SO_3^- band at the positive potential. Moreover, the trend of potential dependence of the peak amplitude is very similar to each other for the CH_3, CN and SO_3^- bands. These results suggest that

anion adsorption induces the CH_3-down and CN-up orientation of acetonitrile. Such a molecular-level picture at the electrolyte/electrode interface was obtained for the first time in the present study by the use of HD-VSFG spectroscopy with the in-situ reference method.

HD-VSFG spectroscopy was also applied to a super-concentrated electrolyte/platinum interface with LiTFSA salt and an acetonitrile solvent. In 0.1 M LiTFSA condition, The $\mathrm{Im}\chi^{(2)}$ spectra show that free acetonitrile, η^2 species and CN^- exist in the vicinity of the platinum electrode. As η^2 species and CN^- are considered to be reaction intermediates in acetonitrile decomposition, the observations of these species clearly indicate that the acetonitrile molecule decomposes in 0.1 M LiTFSA condition. On the other hand, in 4.2 M LiTFSA condition, no peak associated with η^2 species or CN^- is observed in all potential region studied. This clearly indicates that the acetonitrile does not decompose in 4.2 M LiTFSA condition. Instead, a new band is observed in the VSFG spectra in the anion stretch frequency region, indicating the formation of a TFSA-decomposition layer on the electrode surface. The ex-situ air/platinum measurement after electrochemical HD-VSFG measurements clearly shows that the band is still observed after washing the sample substrate. This result implies that an insoluble layer is formed on the electrode surface. These result support the hypothesis that the TFSA-decomposition layer protects acetonitrile from reductive decomposition at the negative potential. A clear picture of formation of TFSA-decomposition layer is obtained with in-situ observation for the first time in the present study.

6.2. Future perspectives

Electrochemical HD-VSFG spectroscopy enables in-situ observation of structure of electrolyte/electrode interfaces as described in this thesis. Most of the mechanism of electrochemical reactions has still been veiled, and thus electrochemical HD-VSFG spectroscopy is expected to play very important roles for revealing such electrochemical reactions. For example, even the detail of lithium intercalation reaction in the current LIB has not been fully understood. Application of electrochemical HD-VSFG spectroscopy to actual LIB system can provide us with new knowledge about the working mechanism of the LIB. Of course, there are other electrolyte/electrode interfaces for which electrochemical HD-VSFG spectroscopy will be useful such as solid electrolyte, photocatalytic electrode, and biological electrode interfaces.

In the present thesis study, the behavior of ions could be discussed only by using the conventional VSFG spectroscopy. Therefore, the orientation of ions cannot be determined. However, orientation of ions is very interesting and important for clarifying more detailed interface structure of electrolyte/electrode interfaces. In order to realize the electrochemical HD-VSFG measurement in the

low frequency region (~ 1000 cm^{-1}), a new reference material other than quartz need to be found. Once we find a suitable new reference material, the electrochemical HD-VSFG measurement in the low frequency region will be soon realized.

A prototypical electrochemical reaction was also studied in this thesis. However, in the present study, only reactivity of acetonitrile was discussed. For the further understanding of the mechanism of electrochemical reactions, dynamics study is essential. To achieve this goal, the pump-probe measurement is one of the most promising methods. Free electrons of the metal electrode can be excited by UV-pump, and thus pump-probe electrochemical HD-VSFG spectroscopy will reveal the dynamics of reductive electrochemical reactions. Such dynamical information will be utilized for understanding the important chemical reactions such as reductive reactions on the photocatalytic electrodes.

The history of electrochemistry is long, and batteries are now indispensable for modern society. However, the structure and molecular mechanisms of electrochemical reactions at electrolyte/electrode interfaces have not been well elucidated although a lot of efforts have been made to study electrolyte/electrode interfaces. I hope the present study has contributed to open a new way to elucidate the molecular details of the electrolyte/electrode interfaces.

Reference

[1]. X. Hu, J. Tan and S. Ye, J. Phys. Chem. C **121**, 15181 (2017).

[2]. K. Tanabea and W. F. HoÈlderich, Appl. Catal. A **181**, 399 (1999).

[3]. R. Fong, U. V. Sacken and J. R. Dahn, J. Electrochem. Soc. **137**, 2009 (1990).

[4]. M. Hirayama, Surface Science (表面科学) **38** (12), 626 (2017).

[5]. B. M. Marsh, M. E. Vaida, S. K. Cushing, B. R. Lamoureux and S. R. Leone, J. Phys. Chem. C **121**, 21904 (2017).

[6]. S. Miyashita, M. Wakisaka, A. Iiyama and H. Uchida, Langmuir **33** (8877-8882) (2017).

[7]. F. Lüpke, J. Doležal, V. Cherepanov, I. Ošt'ádalc, F. S. Tautz and B. Voigtländer, Surf. Sci. **681**, 130 (2019).

[8]. K. Kimura, K. Miwa, H. Imada, M. Imai-Imada, S. Kawahara, J. Takeya, M. Kawai, M. Galperin and Y. Kim, Nature **570**, 210 (2019).

[9]. E. V. Dubrovin, N. A. Barinov, T. E. Schäffer and D. V. Klinov, Langmuir **35**, 9732 (2019).

[10]. Y. Ando, Jpn. J. Appl. Phys. **43**, 4506 (2004).

[11]. X. Ma, T. Kratky and S. Günther, Nanoscale Adv. (2019).

[12]. B. B. Jena and K. S. R. Menon, AIP Conference Proceedings **2115**, 030308 (2019).

[13]. T. Kondo, T. Masuda, N. Aoki and K. Uosaki, J. Phys. Chem. C **120**, 16118 (2016).

[14]. F. Santos, J. Abad, M. Vila, G. R.Castro, A. Urbina and A. J. F. Romeroa, Electrochim. Acta **281**, 133 (2018).

[15]. J. C. Pramudita, R. Aughterson, W. M. Dose, S. W. Donne, H. E. A. Brand and N. Sharma, J. Mater. Res. **30**, 381 (2015).

[16]. M. Araki, Y. Matsushita and K. Tsukiyama, Astronomical Journal **150**, 113 (2015).

[17]. M. Miyazaki, A. Naito, T. Ikeda, J. Klyne, K. Sakota, H. Sekiya, O. Dopfer and M. Fujii, Phys. Chem. Chem. Phys. **20** (2018).

[18]. H.Yui, K.Kanoh, H.Fujiwara and T.Sawada, J. Phys. Chem. A **106**, 12041 (2002).

[19]. S. Takeuchi, S. Ruhman, T. Tsuneda, M. Chiba, T. Taketsugu and T. Tahara, Science **322**, 1073 (2008).

[20]. N. M. Markovic, H. A. Gasteiger and P. N. Ross, J.Phys.Chem. **100**, 6715 (1996).

[21]. C. William, O. J. Manuel and R. Antonio, J. Electroanal. Chem. **764**, 79 (2016).

[22]. Y. X. Chen, A. Miki, S. Ye, H. Sakai and M. Osawa, J. Am. Chem. Soc. **125**, 3680 (2003).

[23]. E. Boscheto, B. C. Batsista, R. B. Lima and H. Varela, J. Electroanal. Chem. **642**, 17 (2010).

[24]. S. J. Huo, X. K. Xue, Y. G. Yan, Q. X. Li, M. Ma, W. B. Cai, Q. J. Xu and M. Osawa, J. Phys. Chem. B **110**, 4162 (2006).

[25]. K. Nakata, Y. Kayama, K. Shimazu, A. Yamakata, S. Ye and M. Osawa, Langmuir **24**, 4358 (2008).

[26]. K. N. Heck, B. G. Janesko, G. E. Scuseria, N. J. Halas and M. S. Wong, J. Am. Chem. Soc. **130**, 16592 (2008).

[27]. X. Li, D. Heryadi and A. A. Gewirth, Langmuir **21**, 9251 (2005).

[28]. R. Gomez, J. S. Gullon, J. M. Perez and A. Aldaz, ChemPhysChem **6**, 2017 (2005).
[29]. R. A. Gu, P. G. Cao, Y. H. Sun and Z. Q. Tian, J. Electroanal. Chem. **528**, 121 (2002).
[30]. X. D. Zhu, H. Suhr and Y. R. Shen, Phys. Rev. B **35**, 3047 (1987).
[31]. J. H. HUNT, P. GUYOT-SIONNEST and Y. R. SHEN, Chem. Phys. Lett. **133**, 189 (1987).
[32]. Y. R. Shen, *Fundamentals of Sum-Frequency Spectroscopy*. (Cambridge University Press, 2016).
[33]. X. D. Zhu, H. Suhr and Y. R. Shen, Phys. Rev. B, 3047 (1987).
[34]. S. Liu, A. a. Liu, B. Wen, R. Zhang, C. Zhou, L. M. Liu and Z. Ren, J . Phys. Chem. Lett. **6**, 3327 (2015).
[35]. A. A. Liu, S. Liu, R. Zhang and Z. Ren, J. Phys. Chem. C **119**, 23486 (2015).
[36]. J. Schaefer, G. Gonella, M. Bonn and E. H. G. Backus, Phys. Chem. Chem. Phys. **19**, 16875 (2017).
[37]. G. Neri, P. M. Donaldson and A. J. Cowan, J. Am. Chem. Soc. **139**, 13791 (2017).
[38]. R. Superfine, J. Y. Huang and Y. R. Shen, Opt. Lett. **15**, 1276 (1990).
[39]. N. Ji, V. Ostroverkhov, C. Y. Chen and Y. R. Shen, J. Am. Chem. Soc. **129**, 10056 (2007).
[40]. S. Nihonyanagi, S. Yamaguchi and T. Tahara, J. Chem. Phys. **130**, 204704 (2009).
[41]. M. Okuno and T. Ishibashi, J. Phys. Chem. C **119**, 9947 (2015).
[42]. P. C. Singh, S. Nihonyanagi, S. Yamaguchi and T. Tahara, J. Chem. Phys. **137**, 094706 (2012).
[43]. S. Nihonyanagi, S. Yamaguchi and T. Tahara, Chem. Rev. **117**, 10665 (2017).
[44]. K. Inoue, P. C. Singh, S. Nihonyanagi, S. Yamaguchi and T. Tahara, J. Phys. Chem. Lett. **8**, 5160 (2017).
[45]. S. Nihonyanagi, P. C. Singh, S. Yamaguchi and T. Tahara, Bull. Chem. Soc. Jpn. **85**, 758 (2012).
[46]. A. Myalitsin, S. Urashima, S. Nihonyanagi, S. Yamaguchi and T. Tahara, J. Phys. Chem. C **120**, 9357 (2016).
[47]. S. Urashima, A. Myalitsin, S. Nihonyanagi and T. Tahara, J. Phys. Chem. Lett. **9**, 4109 (2018).
[48]. F. Dederichs, K. A. Friedrich and W. Daum, J. Phys. Chem. B **104**, 6626 (2000).
[49]. S. Baldelli, G. Mailhot, P. Ross, Y. R. Shen and G. A. Somorjai, J. Phys. Chem. B **105**, 654 (2001).
[50]. S. Baldelli, G. Mailhot, P. N. Ross and G. A. Somorjai, J. Am. Chem. Soc. **123**, 7697 (2001).
[51]. S. Nihonyanagi, S. Ye, K. Uosaki, L. Dreesen, C. Humbert, P. Thiry and A. Peremans, Surf. Sci. **573**, 11 (2004).
[52]. Z. D. Schultz, S. K. Shaw and A. A. Gewirth, J. Am. Chem. Soc. **127** (45), 15916 (2005).
[53]. H. Noguchi, T. Okada and K. Uosaki, Faraday Discuss. **140**, 125 (2008).
[54]. F. Vidal, A. Tadjeddine, C. Humbert, L. Dreesen, A. Peremans, P. A. Thiry and B. Busson, J. Electroanal. Chem. **672**, 1 (2012).

[55]. B. G. Nicolau, N. García-Rey, B. Dryzhakov and D. D. Dlott, J. Phys. Chem. C **119** (19), 10227 (2015).
[56]. T. Iwahashi, Y. Miwa, W. Zhou, Y. Sakai, M. Tamagata, M. Ishikawa, D. Kim and Y. Ouchi, Electrochem. Commun. **72**, 54 (2016).
[57]. Y. Horowitz, H. Han, P. N. Ross and G. A. Somorjai, J. Am. Chem. Soc. **138** (3), 726 (2016).
[58]. S. A. Sorenson, J. G. Patrow and J. M. Dawlaty, J. Am. Chem. Soc. **139** (6), 2369 (2017).
[59]. W. Xiong, J. E. Laaser, R. D. Mehlenbacher and M. T. Zanni, PNAS **108**, 20902 (2011).
[60]. S. Takeuchi, *Text book of 58th summer school of society for young molecular scientists (第58回分子科学夏の学校　テキスト)*. (2018).
[61]. X. Zhuang, P. B. Miranda, D. Kim and Y. R. Shen, Phys. Rev. B **59**, 12632 (1999).
[62]. R. Lu, W. Gan, B. H. Wu, H. Chen and H. F. Wang, J. Phys. Chem. B **108**, 7297 (2004).
[63]. X. Wei, S. C. Hong, X. W. Zhuang, T. Goto and Y. R. Shen, Phys. Rev. E **62**, 5160 (2000).
[64]. M. B. Feller, W. Chen and Y. R. Shen, Phys. Rev. A, 6778 (1991).
[65]. H. WANG, W. GAN, R. LU, Y. RAO and B.-H. WU, International Reviews in Physical Chemistry **24**, 191 (2005).
[66]. I. V. Stiopkin, C. Weeraman, P. A. Pieniazek, F. Y. Shalhout, J. L. Skinner and A. V. Benderskii, Nature **474**, 192 (2011).
[67]. L. Götte, K. M. Parry, W. Hua, D. Verreault, H. C. Allen and D. J. Tobias, J. Phys. Chem. A **121** (34), 6450 (2017).
[68]. Y. Nojima, Y. Suzuki, M. Takahashi and S. Yamaguchi, J. Phys. Chem. Lett. **8**, 5031 (2017).
[69]. S. Nihonyanagi, A. Sayama, Y. Ohshima and T. Tahara, Chem. Lett. **48**, 1387 (2019).
[70]. V. V. Pavlishchuk and A. W. Addison, Inorg. Chim. Acta **298**, 97 (2000).
[71]. C. P. Rinslanda, S. W. Sharpeb and R. L. Samsb, J. Quant. Spectrosc. Radiat. Transf. **96**, 271 (2005).
[72]. S. A. Sheppard, S. A. Campbell, J.R.Smith, G.W.Lloyd, T.R.Ralph and F.C.Walsh, Analyst **123**, 1923 (1998).
[73]. M. Korenobu, The University of Tokyo, 2013.
[74]. L. D. Nguyen, K. Nakatani and B. Journet, Photonics Technology Letters **22**, 857 (2010).
[75]. M. A. Czarnecki and J. P. Hawranek, Bulletin of the polish academy of sciences : chemistry **34**, 509 (1986).
[76]. D. W. Lynch and W. R. Hunter, in *Handbook of Optical Constants of Solids*, edited by E. D. Palik (Academic Press 1985), Vol. I.
[77]. G. R. Bell, Z. X. Li and C. D. Bain, J. Phys. Chem. B **102** (47), 9461 (1998).
[78]. T. Radhakrishnan, Proc. Indian Acad. Sci. (Math. Sci.) **25** (3), 260 (1947).
[79]. M. R. Anderson and M. Gatin, Langmuir **10** (6), 1638 (1994).
[80]. Z. Li, S. Chang and R. S. Williams, Langmuir **19** (17), 6744 (2003).
[81]. M. A. Hines, J. A. Todd and P. Guyot-Sionnest, Langmuir **11** (2), 493 (1995).
[82]. H. Noguchi, M. Ito and K. Uosaki, Chem. Lett. **34** (7), 950 (2005).

[83]. P. Guyot-Sionnest, A. Tadjeddine and A. Liebsch, Phys. Rev. Lett. **64** (14), 1678 (1990).
[84]. A. Tadjeddine, A. Le Rille, O. Pluchery, F. Vidal, W. Q. Zheng and A. Peremans, Phys. Stat. Sol. (a) **175**, 89 (1999).
[85]. C. D. Bain, J. Chem. Soc. Faraday Trans. **91** (9), 1281 (1995).
[86]. M. Himmelhaus, F. Eisert, M. Buck and M. Grunze, J. Phys. Chem. B **104** (3), 576 (2000).
[87]. R. Lu, W. Gan, B.-h. Wu, Z. Zhang, Y. Guo and H. Wang, J. Phys. Chem. B **109** (29), 14118 (2005).
[88]. M. Oh-e, A. I. Lvovsky, X. Wei and Y. R. Shen, J. Chem. Phys. **113** (19), 8827 (2000).
[89]. Y. Yamada, J. Wang, S. Ko, E. Watanabe and A. Yamada, Nature Energy **4**, 269 (2019).
[90]. Y. Zhang, M. Konya, A. Kutsumura, S. Lim, T. Mandai, H. Munakata and L. Kanamura, small **15**, 1902236 (2019).
[91]. K. R. Adair, C. Zhao, M. N. Banis, Y. Zhao, R. Li, M. Cai and X. Sun, Angew. Chem. Int. Ed. **58**, 1 (2019).
[92]. A. J. Bard and L. R. Faulkner, *Electrochemical Methods: Fundamentals and Applications*, 2 ed. (Wiley, New York, 2000).
[93]. *Rika Nenpyo (Chronological Scientific Tables 2014)*. (Maruzen Publishing Co., Ltd., 2013).
[94]. P. Venkateswarlu, J. Chem. Phys. **19**, 293 (1951).
[95]. R. Raval and M. A. Chesters, Surf. Sci. **219**, L505 (1989).
[96]. K. Saito, Q. Peng, L. Qiao, L. Wang, T. Joutsuka, T. Ishiyama, S. Ye and A. Morita, Phys. Chem. Chem. Phys. **19**, 8941 (2017).
[97]. S. Yamaguchi, K. Shiratori, A. Morita and T. Tahara, J. Chem. Phys. **134**, 184705 (2011).
[98]. K. Matsuzaki, S. Nihonyanagi, S. Yamaguchi, T. Nagata and T. Tahara, J. Chem. Phys. **151**, 064701 (2019).
[99]. H. J. Herrera-Suarez, A. Rubio-Ponce and D. Olguin, Rev. Mex. Fis. **58**, 46 (2012).
[100]. K. Saito, Q. Peng, L. Qiao, L. Wang, T. Joutsuka, T. Ishiyama, S. Ye and A. Morita, Phys. Chem. Chem. Phys. **19**, 8941 (2017).
[101]. A. T. Hubbard, E. Y. Cao and D. A. Stern, Electrochim. Acta **39**, 1007 (1994).
[102]. B. Bozzini, B. Busson, A. Gayral, C. Humbert, C. Mele, C. Six and A. Tadjeddine, Molecules **17** (7), 7722 (2012).
[103]. F. Dederichs, A. Petukhova and W. Daum, J. Phys. Chem. B **105** (22), 5210 (2001).
[104]. E. C. Ou, P. A. Young and P. R. Norton, Surf. Sci. **277**, 123 (1992).
[105]. D. H. Johnston and D. F. Shriver, Inorg. Chem. **32**, 1045 (1993).
[106]. J. M. Alia, Y. D. Mera, H. G. M. Edwards, F. J. Carcia and E. E. Lawson, J. Mol. Struct. **408/409**, 439 (1997).
[107]. P. Geetha, M. Nair, C. Y. Panicker, H.T.Varghese, S. M. Y, K. Raju and P. S. A. Devi, Orient. J. Chem. **26**, 167 (2010).
[108]. P. Venlateswarlu, J. Chem. Phys. **19**, 293 (1951).
[109]. K. Inoue, T. Ishiyama, S. Nihonyanagi, S. Yamaguchi, A. Morita and T. Tahara, J. Phys.

Chem. Lett. **7**, 1811 (2016).
[110]. R. Kusaka, T. Ishiyama, S. Nihonyanagi, A. Morita and T. Tahara, Phys. Chem. Chem. Phys. **20**, 3002 (2018).
[111]. K. Xu, Chem. Rev. **114**, 11503 (2014).
[112]. Y. Yamada, K. Furukawa, K. Sodeyama, K. Kikuchi, M. Yaegashi, Y. Tateyama and A. Yamada, J. Am. Chem. Soc. **136**, 5039 (2014).
[113]. K. Sodeyama, Y. Yamada, K. Aikawa, A. Yamada and Y. Tateyama, J. Phys. Chem. C **118**, 14091 (2014).
[114]. Y. Yamada, J. Wang, S. Ko, E. Watanabe and A. Yamada, Nature energy **4**, 269 (2019).
[115]. Y. Yamada, K. Usui, K. Sodeyama, S. Ko, Y. Tateyama and A. Yamada, Nature Energy **1**, 1 (2016).
[116]. J. P. BILLON, J. Electroanal. Chem. **1**, 486 (1959/1960).
[117]. M. W. Rupich, L. Pitts and K. M. Abraham, J. Electrochem. Soc. **129**, 1857 (1982).
[118]. B. Braunschwig, P. Mukherjee, D. D. Dlott and A. Wieckowski, J. Am. Chem. Soc. **132**, 14036 (2010).
[119]. B. Braunschweig and A. Wieckowski, J. Electroanal. Chem. **716**, 136 (2014).
[120]. B. Braunschweig, P. Mukherjee, J. L. Haan and D. D. Dlott, J. Electroanal. Chem. **800**, 144 (2017).
[121]. B. A. SEXTON and N. R. AVERY, Surf. Sci. **129**, 21 (1983).
[122]. S. Morin and B. E. Conway, J. Electroanal. Chem. **376**, 135 (1994).
[123]. S. Morin, B. E. Conway, G. J. Edens and M. J. Weaver, J. Electroanal. Chem. **421**, 213 (1997).
[124]. D. M. Seo, O. Gorodin, S. Han, P. D. Boyle and W. A. Henderson, J. Electrochem. Soc. **159**, A1489 (2012).

謝辞

月日が経つのは早いもので、博士課程の 3 年間が過ぎ去ろうとしています。道中は辛いこと、上手くいかないことが多々ありましたが、振り返ってみるとあっという間に過ぎ去った 3 年間でした。修士課程のときに進路に悩んで、博士課程に進学し、かつ分野を大きく変えたことは今思い返してみると思い切ったことをしたなと思うばかりです。修士課程までは気相での研究に従事していたこともあり、理化学研究所において界面、しかも、より複雑な凝縮相同士の界面に関するテーマに取り組むことになった際には期待以上の不安がありました。実験技術の習得はもちろんのこと、今まで深く関わってこなかった界面化学や電気化学の勉強、慣れない英語でのコミュニケーションなど、乗り越えなければならない課題も多数ありました。今となってはそれらも良い思い出です。

理化学研究所において研究を指導してくださった田原　太平　主任研究員には大変感謝しております。私が博士課程における進学先を検討している際に、田原主任研究員は快く研究室見学を了承してくれ、見ず知らずの学生であった私にも研究がしたいならぜひ来てくれと言ってくださいました。この言葉がなければ理化学研究所で研究をしようと決意することはなかったかもしれません。時には熱い指導もありましたが、この 3 年間で大きく成長できたのは田原主任研究員のおかげです。ありがとうございます。

東京工業大学での指導教官を引き受けてくださった大島　康裕　教授には本当に頭が上がりません。私が理化学研究所で研究を行うにあたって、大学での指導教官をどうするかという問題について相談した際に、自身の研究室で研究を行うわけではないにも関わらず、指導教官を引き受けても良いと言ってくださいました。大島先生の懐の深さがなければ理化学研究所で研究を行うことは叶いませんでした。ありがとうございます。

実際の研究活動を指導してくれた二本柳　聡史　専任研究員は研究に関する議論から論文の添削に至るまで様々な場面でお世話になりました。正直、馬が合わないと思うことが多々ありましたが、なんとかここまでやってこれました。ありがとうございます。

石井　邦彦　専任研究員はミーティングでの議論からお昼時の雑談に至るまで、様々な場面でお世話になりました。石井さんの指摘は自分が考え至っていなかったことであることがほとんどであり、自身の研究について考える際の良いきっかけとなりました。ありがとうございます。

倉持　光　研究員は私が理化学研究所で研究するためにはどうすればいいかと悩んでいるときに、快く相談に乗ってくださいました。倉持さんに相談に乗っていただいていなかったら、東工大所属のまま理化学研究所で研究を行うことは叶わなかったかもしれません。ありがとうございます。

坂口　美幸　氏　は実験室の管理など、実験を進めていく上で必要な事項を丁寧に説明してくださいました。ありがとうございます。

Dr. Bidyut Sarkar gave me a lot of great useful advises for my presentation. Also, he kindly cooked great Indian dishes for us on the laboratory trip. Thank you.

Dr. Ahmed Mohammed gave me significant questions about my research and encouraged me as a member of interface research team. Thank you.

Dr. Pardeep Kumar gave me many critical comments and suggestions for studying the electrolyte/electrode interfaces. Thank you.

Dr. Woongmo Sung joined RIKEN Tahara group as same timing as me. He gave me a lot of important questions and comments about studying the electrolyte/electrode interfaces. Moreover, he helped me to optimize the alignment of optical setup and measure air/liquid spectra. I really appreciate him. Thank you.

松崎　維信　氏は界面研究に関する基礎的な部分から、昼食後の雑談に至るまで様々な場面でお世話になりました。研究活動を健康的に進めていく上で、松崎氏との会話は精神面において非常に重要な役割を果たしていたと思います。ありがとうございます。

高梨　司　氏はかつて気相で研究を行っていた身同士ということもあり、研究を進めていく上での議論から博士課程における生活に至るまで、幅広く相談に乗っていただきました。高梨さんの助けがなければ博士課程を終えることはできなかったかもしれません。ありがとうございます。

Dr. Li Liu supported me for relieving stress. He sometimes took me for dinner and drinking. Thank you.

Dr. Feng Wei gave me a lot of suggestions for preparation of thin film sample substrates. Thank you.

Dr. Wooseok Heo gave me Korean traditional tonics. They were very useful to make my physical condition better. Thank you.

Mr. Chun-Fu Chang is a fellow who fought together in completing Ph. D program. He gave me great comments, suggestions and questions for writing a paper. I really appreciate him. Thank you.

秘書の加藤　智子　氏には研究室の他のメンバーには話しにくい内容などの相談に乗っていただき、大変感謝しております。加藤さんがいなかったら早々に博士課程での重圧に負

けてつぶれていたかもしれません。ありがとうございます。

竹内　佐年　教授には夏の学校での講義など、勉学の面で大変お世話になりました。竹内さんの講義を受けたことで、非線形分光学に関する理解が進んだと思います。ありがとうございます。

井上　賢一　氏には界面化学に関する知識を教授していただきました。グループミーティングなどでの鋭い指摘は、界面に関する理解を深めるうえで非常に有益でした。ありがとうございます。

田原　進也　氏には主にプライベートの面で大変お世話になりました。ご飯に連れて行ってもらったり、相談に乗っていただいたりと、先輩として非常に尽くしてくれたと思います。ありがとうございます。

浦島　周平　氏にはまだ研究室に来て間もないときに実験などを手伝ってくださり、非常に助かりました。学会での彼の質疑は研究を進めていく上で非常に有益でした。ありがとうございます。

Dr. Sanat Ghosh was a colleague who worked together in the interface research team. He previously studied molecules in gas phase, same as me. Therefore, discussion with him was very interesting time for me. I miss him. Thank you.

長谷川　一途　氏は研究室の数少ない学生同士ということもあり、くだらない雑談によくつきあっていただきました。おそらく彼との雑談が研究室で生活していくうえで心の平穏を保つのに一番大きく貢献していたと思います。ありがとうございます。

以前秘書だった　道幸　智恵　氏には就職活動に関することで様々なアドバイスをいただきました。ありがとうございます。

理研技術基盤支援チームの洲之内　啓　氏には電気化学セルの開発において大変お世話になりました。こちらの無茶な要求にも応えていただき、感謝しております。洲之内さんがいなければ電気化学セルが作れず、研究も早々に頓挫していたかもしれません。ありがとうございます。

理研創発物性科学研究支援チームの四方山　和彦　氏には基盤製作において大変お世話になりました。薄膜形成に関して素人であった私に、装置の使い方を丁寧に教えてくださいました。また、薄膜形成に関する相談をした際にも親切に対応してくれました。基盤を安定して作れるようになったのも四方山さんの協力があってこそです。ありがとうございます。

修士時代の指導教官であった北島　昌史　准教授には博士課程で研究室を変えることを了承していただき、大変感謝しております。研究室を変えたいと相談した際は、決して良い気分ではなかったと思いますが、それでも私のためを思ってその後の相談にも乗っていただけたこと、ありがたく思っています。北島先生が送り出してくれたからこそ、理化学研究所で研究を行うことができました。ありがとうございます。

東工大での同期である鳥塚 祐太郎 氏は修士時代からの長い付き合いとなりました。博士課程を共に戦う仲間として、一緒に飲みに行ったり、就職活動でお互いに慰めあったりと私にとっては大きな支えとなっていました。それと同時に分野の幅を広げる選択をした私に対して、一つの分野を極めようとする選択をした彼の強さをどこか羨ましく思っていた部分もあります。彼がいたからこそ、将来的に自分がどう成長していきたいのか、どうするべきか真摯に考えることができたように思えます。ありがとうございます。

大島・山﨑研究室の後輩たちは東工大に顔を出したときに温かく迎えてくれました。理化学研究所は学生が少ないこともあり、時折大学の雰囲気が恋しくなるときもありました。そのような中で後輩たちとの雑談はホッと息をつける数少ない時間であったように思えます。ありがとうございます。

分子科学若手の会で出会った仲間たちは研究生活を行っていく上で大きな励みとなりました。夏の学校などのイベントを通して交流を深めると同時に、議論を重ねることで他分野に関する理解が深まりました。ありがとうございます。

東北大学の高橋　正彦　教授には研究活動を応援していただいたことに大変感謝しております。原子衝突若手の会でお話させていただいたことをきっかけに、セミナーに呼んでいただいたり、学会発表を聴講しにきてくださったりと、他分野の学生でありがなら非常に親身に尽くしていただけました。高橋先生の励ましがあってこそ、辛い研究生活も頑張ろうと思えました。ありがとうございます。

東京理科大学の由井　宏治　教授には勉学を含めた研究面において深く感謝しております。思えば決して優秀ではない私が博士課程までやってこれたのも、由井先生の丁寧かつ熱心な物理化学の講義があったからこそです。特に、博士課程で界面に関する研究をやってみようと思えたのも、学部時代に由井先生の講義を受けて、実際に由井先生の研究室を見学させていただいたという経験があってこそです。ありがとうございます。

私の最初の指導教官である東京理科大学の築山 光一 教授には大変深く感謝しております。博士課程への進学、また、博士課程に進学してからの辛い研究生活について相談した際も温かい励ましの言葉を頂きました。学部から博士課程まで、学生としては多くの研究室を経験しましたが、築山研究室での研究は私の原点ともいえるものです。自分の将来像を考え

たときに、目指したい先として築山先生の存在は非常に大きなものとなっています。本当に感謝しております。ありがとうございます。

本博士論文における研究内容は理化学研究所　大学院生リサーチアソシエイト制度の下行われたものです。研究環境・資金面でサポートをしてくださった理化学研究所には深く感謝しています。

最後に、博士課程への進学を応援してくれ、私生活面で大きく支えてくれた家族に感謝し、謝辞とさせていただきます。